Downloaded from orbit.dtu.dk on: May 06, 2023

DTU Library

Electrostatic Turbulence in Strongly Magnetized Plasmas

Nielsen, Anders Henry

Publication date:
1993

Document Version
Publisher's PDF, also known as Version of record

Link back to DTU Orbit

Citation (APA):
Nielsen, A. H. (1993). *Electrostatic Turbulence in Strongly Magnetized Plasmas*. Risø National Laboratory.

General rights
Copyright and moral rights for the publications made accessible in the public portal are retained by the authors and/or other copyright owners and it is a condition of accessing publications that users recognise and abide by the legal requirements associated with these rights.

- Users may download and print one copy of any publication from the public portal for the purpose of private study or research.
- You may not further distribute the material or use it for any profit-making activity or commercial gain
- You may freely distribute the URL identifying the publication in the public portal

If you believe that this document breaches copyright please contact us providing details, and we will remove access to the work immediately and investigate your claim.

DK9300017

RISØ

Risø-R-659(EN)

Electrostatic Turbulence in Strongly Magnetized Plasmas

Anders H. Nielsen

Risø National Laboratory, Roskilde, Denmark
January 1993

Electrostatic Turbulence in Strongly Magnetized Plasmas

Risø-R-659(EN)

Anders H. Nielsen

Risø National Laboratory, Roskilde, Denmark
January 1993

Abstract Turbulence in plasmas has been investigated experimentally and numerically.

- On the experimental side the turbulent nature of the Kelvin-Helmholtz instability has been studied in a single-ended Q-machine. The development of coherent structures in the background of the turbulent flow has been demonstrated and the capability of structures of transporting plasma across the magnetic field-lines is explained in detail.

The numerical investigations are divided into two parts:

- Numerical simulations of the dynamics from the Q-machine experiments using spectral methods to solve the two-dimensional Navier-Stokes equations in a cylindrical geometry.
- A numerical study of the Eulerian-Lagrangian transformation in a two-dimensional flow. Here the flow is made up by a large number of structures, where each individual structure is convected by the superposed flow field of all the others.

This report is practically identical to the thesis submitted to the Technical University of Denmark for obtaining the Ph.D. degree. It was submitted on the 6 of September 1991 and the lecture held on the 9 December 1991.

ISBN 87-550-1865-3
ISSN 0106-2840

Grafisk Service · Risø · 1993

Contents

1 Introduction *7*

2 Experimental Investigations of Low-Frequency Fluctuations *9*

2.1 Experimental Setup *9*

2.2 Basic Plasma Characteristics *11*

2.3 Stability Analysis *13*

2.4 Conditional Analysis *18*

2.5 Conditionally Averaged Potentials *21*

2.6 Flux Measurement *30*

2.7 Conclusions and Discussions *34*

3 Navier-Stokes Equations *38*

3.1 Introduction *38*

3.2 Numerical Scheme *39*

3.3 The Poisson Solver *43*

3.4 The Convolution Sum *45*

3.5 The Time Evolution *47*

3.6 Energy and Enstrophy Evolution *49*

3.7 Numerical Results *51*

3.8 Conclusions and Discussions *59*

4 Studies of the Eulerian-Lagrangian Transformation in Two-Dimensional Flows *61*

4.1 Introduction *61*

4.2 Analytical Results *63*

4.3 Numerical Results *68*

4.4 Conclusions and Discussions *77*

References *80*

There is more here
than meets the eye.
Watson !
Sherlock Holmes.

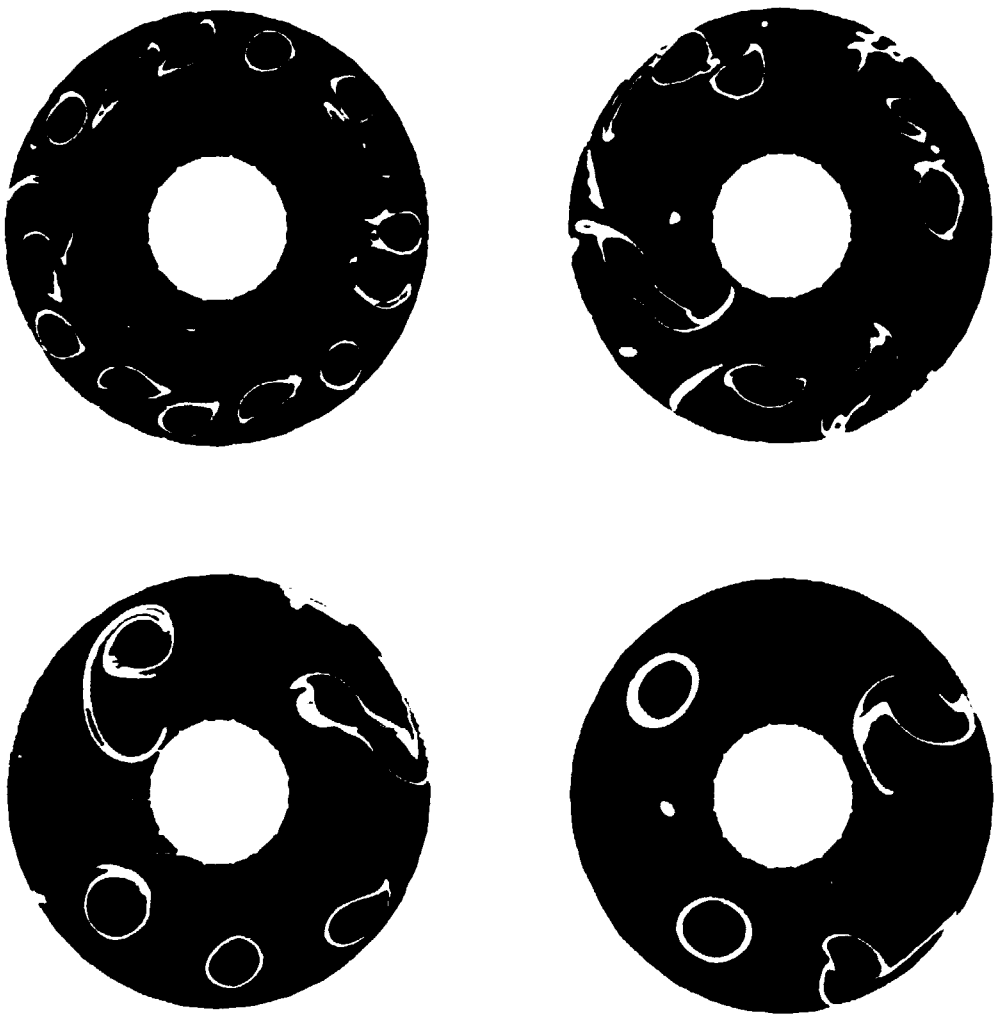

Acknowledgements

This report describes the work in which I have participated during the last three years in the Group for Fondamental Plasma Physics at Risø National Laboratory. None of this would have been possible without the members of this group. They are on the experimental work: my supervisor Prof. H. L. Pécseli, J. Juul Rasmussen and T. Huld and on the numerical simulations: J-P. Lynov and Prof. E. A. Coutsias, the latter from the University of New Mexico, USA, whom I had the pleasure of visiting during half a year in the USA. I would also like to thank M. Nielsen and B. Reher for their technical assistance in the experimental work.

Dansk resumé

Forskellige aspekter af turbulens i plasmaer er blevet udforsket, både eksperimentelt og ved numeriske simulationer. De turbulente fluktuationer har været af *flute*-typen, også kaldet konvektive celler, der kan iagttages i kanten af plasmasøjlen i en Q-maskine. Fluktuationerne bliver genereret af Kelvin-Helmholtz instabiliteten, da det yderste lag af plasmasøjlen roterer med en stærkt varierende vinkelhastighed. Q-maskineforsøgene kan deles op i to hovedgrupper.

- Dels er eksistensen af kohærente strukturer påvist. Disse strukturer er en følge af en spontan kondensering af små-skala fluktuationer. Der er her tale om målte strukturer i det elektrostatiske potentiale samt i plasmatætheden.
- Dels en undersøgelse af den turbulente transport på tværs af magnetfeltlinierne. Denne transport er i dette tilfælde flere størrelsesordener større end den klassiske diffusion, dvs. diffusion der skyldes kollisionsprocesser.

Målingerne er foretaget ved, at tidsserier af de fluktuerende størrelser i sand tid er opsamlet ved hjælp af et digitaloscilloskop og bagefter behandlet ved hjælp af en betinget statistisk metode på en standard PC. Denne statistiske metode har gjort det muligt at iagttage plasmaet, når fluktuationerne i det elektriske felt er store, dvs. når kohærente strukturer er til stede på kanten af plasmasøjlen.

På det numeriske område er der opbygget to computerkoder, der i todimensioner simulerer dynamikken af turbulente væskestrømninger, herunder også den turbulens der kan iagttages i et plasma. Til simulering af dynamikken i Q-maskine eksperimenterne er der udviklet en kode, der løser Navier-Stokes ligningerne i en annulusgeometri. Løsningen findes ved brug af spektrale metoder, hvor der i den radiære retning udvikles i Chebyshev polynomier, mens en Fourier udvikling benyttes i den azimuthale retning. Da løsningerne findes i en række gitterpunker, følger vi dermed strømningen i det Eulerske koordinatsystem. Karakteristiske simuleringer, der udviser den samme form for kondensering af de høj-frekvente fluktuationer, som kan iagttages i Q-maskineforsøgene, vil blive vist.

Den anden computerkode simulerer en turbulent strømning, opbygget af et stort antal hvirvler, hvor hver individuel hvirvel bliver konvekteret af en superpositionering af hastighedsfeltet skabt af samtlige hvirvler i systemet. Koden følger hvirvlernes traktorier, og simuleringerne forgår dermed i det Lagrangske koordinatsystem. En statistisk undersøgelse af det resulterende hastighedsfelt vil blive foretaget og sammenlignet med analytisk udregnede størrelser for både den Eulerske og Lagrangske korrelationsfunktion.

1 Introduction

Turbulence is an interesting subject which has received a vast amount of attention in resent years, especially with the development of fast computer programs to simulate the dynamics of turbulence. Turbulence plays an important role in the time evolution of many systems ranging from the dynamics of largescale systems like the atmospheres of planets such as Jupiter and Saturn, the solar atmosphere and the creation of galaxies to the dynamics of small-scale systems like the turbulence created in the boundary layers on airplanes and cars. One should of course not forget the magnetic fusion research, where turbulence at the edge of the plasma column is believed to play an important role for the transport of the plasma. Due to the many different applications it is difficult to obtain a precise definition of the physical meaning of "turbulence". A very vague definition is that a turbulent flow is disordered in space and time, but this is not a precise mathematical definition. It is problematic to obtain a mathematically acceptable definition as nearly any other scientist will (automatically) disagree with you; the area is too vast for such precise definitions. There is a huge difference between one-, two- and three-dimensional turbulence, between turbulence where a statistical analysis is acceptable and where coherent structures dominate the flow and, especially, where is the transition from a laminar flow to a turbulent flow? Instead of contributing to the variety of definitions already floating around in the system, I will (re)use the best definition I have come across during my three years of PhD study, see Lesieur (1987):

- Firstly, a turbulent flow must be unpredictable, in the sense that a small uncertainty as to its knowledge at a given initial time will amplify so as to render impossible a precise deterministic prediction of its evolution.
- Secondly, it should be able to mix transported quantities much more rapidly than if only molecular diffusion processes were involved.

The subject of the present thesis is turbulence in the form of low-frequency, *flute*-type electrostatic plasma fluctuations propagating across a strong homogeneous magnetic field. The turbulence can thus be restricted to two spatial dimensions in a plane perpendicular to the magnetic field lines. The thesis consists of three (individual) chapters.

In chapter two the potential fluctuations are investigated experimentally in a Q-machine, where a single ionized cesium plasma is confined by the strong magnetic field. Due to a potential difference between the plasma and the confining steel vessel a strong shear flow is created at the edge of the plasma. In the background of this turbulent shear flow the detection of relatively long-lived vortexlike potential and density structures is demonstrated by a conditional sampling technique, see Huld *et al.* (1991, 1990). Depending on the plasma parameters, the dominant structures can appear as monopole or multipole vortices, in particular dipoles. The contribution from these vortices to the total turbulent plasma diffusion is investigated.

In chapter three the two-dimensional Navier-Stokes equations in an annulus geometry are simulated using a spectral method. In the limit of long wavelength these equations are also valid for the fluctuations at the edge of the plasma column described in chapter two. The Navier-Stokes equations are expanded into Chebyshev and Fourier modes, and the different algorithms for solving the differential

equations are described in detail. Preliminary results are shown where the inverse cascade is noticeable, i.e. the cascade of energy from small wavelength to short wavelength.

In chapter four a two-dimensional, incompressible flow is investigated numerically and analytically. The flow is here made up by a large number of structures, where each individual structure is convected by the superposed flow field of all the others, i.e. the model is described in a Lagrangian coordinate frame, where the model in chapter four is simulated in the Eulerian coordinate frame. The statistical properties of the resulting space-time varying random flow are studied. Analytical expressions for both Eulerian and Lagrangian correlation functions are obtained in the limit where the density of structures is large. The analytical results are compared with numerical simulations. The study serves as a special test on proposed relations between Eulerian and Lagrangian averages which can be generally valid, i.e. also for three-dimensional, turbulent flows.

2 Experimental Investigations of Low-Frequency Fluctuations

2.1 Experimental Setup

The experiments, which will be described in this chapter, were performed in the Q-machine at Risø National Laboratory. The experimental setup is shown schematically in Figs. 1 and 2. For a more detailed description of a Q-machine see, for example, Motley (1975). The machine was operated in a single ended mode, where a steady-state singly ionized cesium plasma was produced by surface ionization on a hot tantalum plate with a diameter of 3 cm. This plate was heated from the rear by electron bombardment (energy $1.5-2$ keV) to a temperature of approximately 2200°C. The plasma was confined in the radial direction by a strong magnetic field, B_o, which was produced by 12 large coils surrounding the machine (these coils are not shown in the figure). The magnetic field was variable in the range $0.1-0.6$ T having a ripple of ±4% along the axis of the device with a periodicity corresponding to the coil positions. A terminating "cold" metal plate with variable bias, V_E, was placed at the end of the device . In the experiments this plate was biased negatively with respect to the stainless steel vessel in order to reflect electrons and was heated to approximately 300°C in order to avoid coating with neutral cesium. The total length, viz. the distance between the hot and the cold plate, was variable up to 120 cm. A limiting metal aperture with a 25 mm opening and a variable bias, V_A, was inserted perpendicular to the plasma column at a distance of 25 cm from the hot plate. This aperture was used to scrape off the outer layer of the plasma and control the potential profile. The experiment was confined in a stainless steel vessel with an inner diameter of 15 cm and brought down to a very low pressure, approximately 10^{-6} mmHg, to minimize collisions between the ionized and neutral particles. The magnetic coils were placed around the vessel.

The plasma column could conveniently be considered as being composed of two parts. Firstly, we have a central plasma core terminated by the hot plate. Here the plasma potential, and to a certain degree also the density, was essentially constant (see Figs. 3 and 4) since the hot plate was electrically conductive, and any potential difference would therefore be short-curcuited. Secondly, surrounding this plasma column, we have a residual plasma (Motley (1975)) or scrape-off layer, where the density decreases with the radius while the plasma potential increases towards ground, i.e. the potential of the stainless steel vessel. The residual plasma was terminated by resistive sheaths at both ends (in contrast to the central plasma) since the metal plates (aperture and end plate) were too cold to emit electrons. By varying the aperture potential V_A it was possible to control the residual potential profile. Examples of this are shown in Fig. 3 for three different values of V_A. Also the radial plasma density profile was affected by the aperture bias, see Fig. 4. The radial density gradient was decreasing for decreasing V_A.

To measure the DC-values and fluctuating parts of the floating potential and the plasma density, Langmuir probes were used (Motley (1975), ch. 3). They were spherical platinum probes with a diameter of 1 mm, placed on thin platinum wires, isolated from the plasma by a glass tube (see Chen (1968) and Fig. 2(b)). The probes were coupled through a high-input impedance amplifier (100MΩ) with a

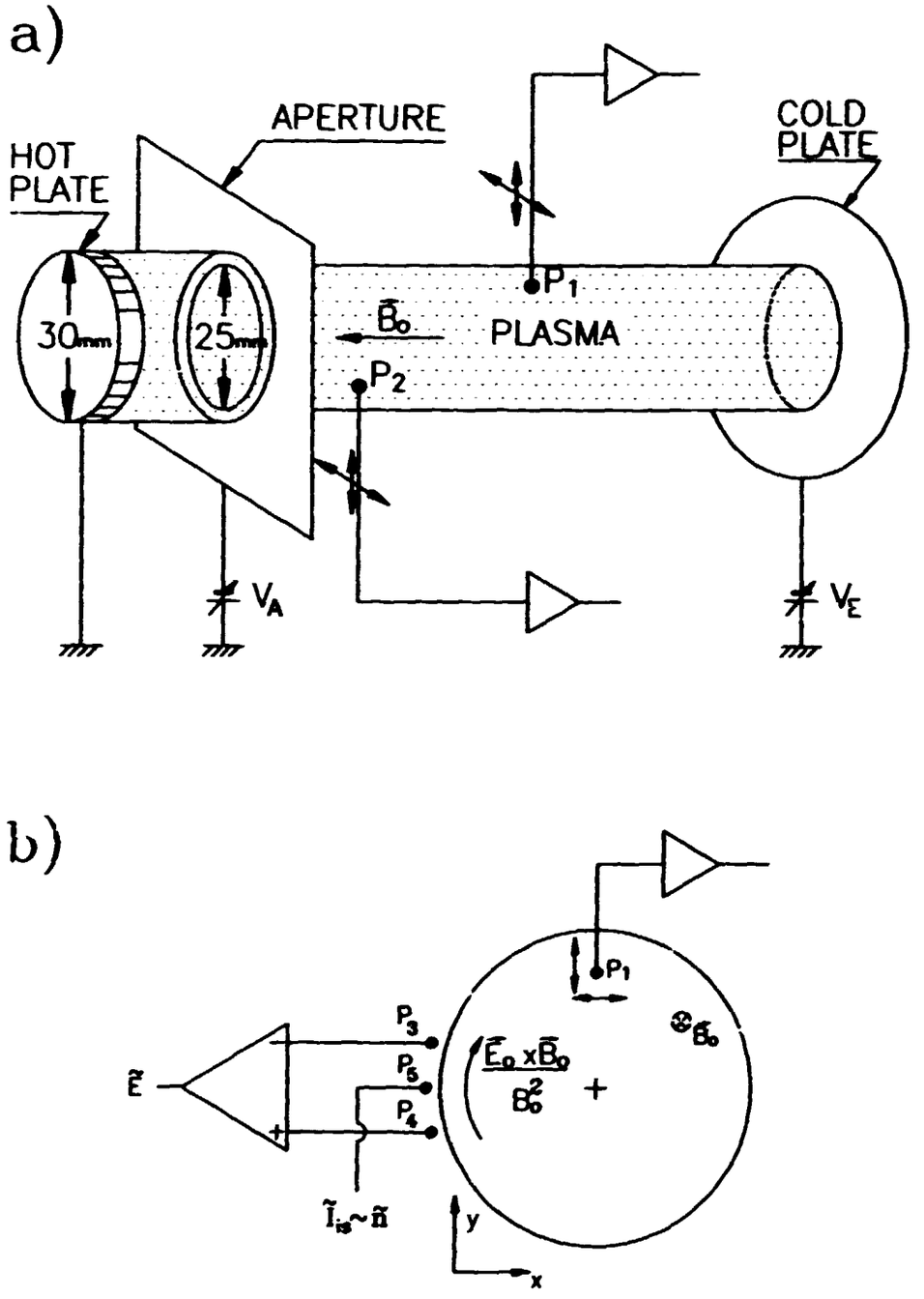

Figure 1. Experimental setup. (a) Plasma column with aperture and terminating end plate shown schematically. (b) Configuration of detecting probes.

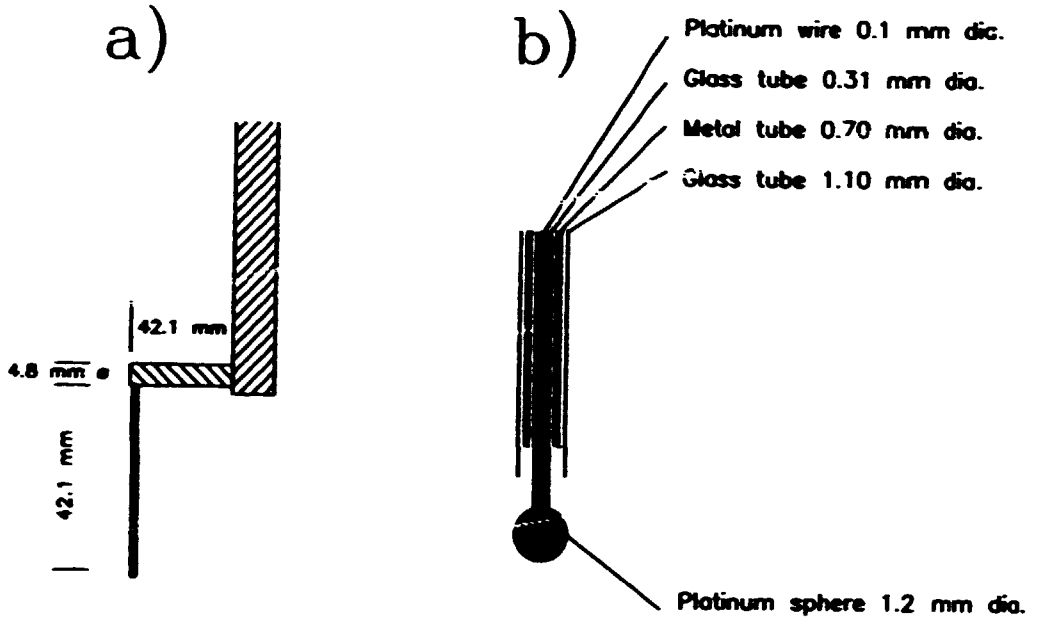

Figure 2. a) Dimensions of the movable probe, P_1 from Fig. 1. b) Close-up of a probe tip.

300 kHz bandwidth placed in the immediate vicinity of the probes. They could thus measure fluctuations in the floating potential. However, at these low-frequency fluctuations the electrons maintain a local Boltzmann distribution around the probe tip, and the difference between the measured floating potential and the plasma potential was in the order of $4T_e \approx 0.8$ V. The electron temperature T_e was to a good approximation found to be constant in the plasma region of interest here. The plasma density was measured by the ion saturation current to the Langmuir probes. As shown in Fig. 1b up to four probes can be used at one time. Three of the probes were fixed, placed at the edge of the plasma column. Two of them were placed with a relative distance of 7 mm and were used to measure the fluctuating part of the electric field. This signal was used as a reference for the conditional analysis, see later sections. The last of the fixed probes, P_3 in Fig. 1(b), was placed between the two others and was used to measure the plasma density. We could thus measure the electric field and the density simultaneously at a "point" at the edge of the plasma column. The fourth probe, P_1 in Fig. 1(b), was movable and could be used to measure the DC-values, or fluctuating parts, of the floating potential or the density. This probe was constructed so that it could penetrate the plasma column with only a small influence of the plasma, see Fig.2.

2.2 Basic Plasma Characteristics

Since both the ions and electrons were produced on the hot plates, their temperatures were approximately the same as the plate temperature, i.e. $T_i \sim T_e \sim 2200°C \sim 0.2eV$, T_i and T_e being the ion and electron temperatures, respectively. These temperatures can be considered to be constant over the entire plasma column since the plasma was not in contact with the wall. Ion Larmor radii were typically 2 mm for our conditions, while the electron Larmor radii could be ignored because of the large difference between the mass of the cesium ions and the

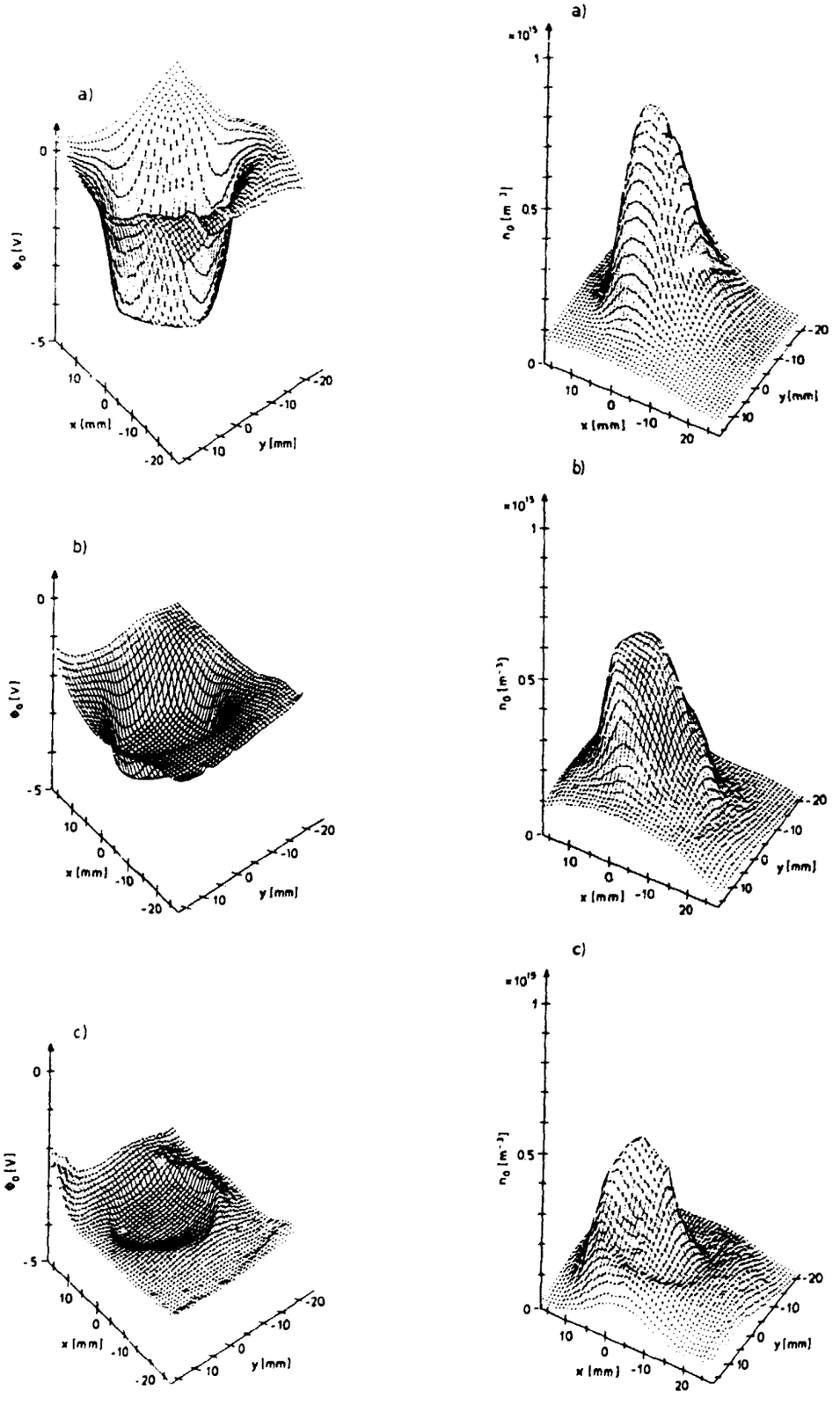

Figure 3. (Left) Variation of the floating potential $\phi_o(r)$ for three values of the aperture bias. (a) $V_A = 0$V, (b) $V_A = -2.25$V and (c) $V_A = -3.2$V, for $B_o = 0.35$T.

Figure 4. (Right) Plasma density $n_o(r)$ variations corresponding to the results in Fig.3.

electrons. Plasma densities were in the range of $10^8 - 10^{10}\mathrm{cm}^{-3}$ in the centre of the plasma column. With these parameters the device was operated in electron-rich conditions, and the plasma column assumed a potential of approximately -3 V with respect to the grounded hot plate (see Fig. 3). To clarify what kind of plasma we are dealing with, some of the basic plasma characteristics will be given here. Using a magnetic field of 0.35 T, a density of $n = 10^9 cm^{-3}$ and the electric field in the residual plasma obtained from Fig. 7, choosing an aperture bias of 0.0 V, will result in the following typical values in the residual plasma region (Chen (1974)): Ion cyclotron frequency:

$$f_{ci} = \frac{eB}{2\pi m_i} \simeq 40\,\mathrm{kHz}. \tag{1}$$

Electron cyclotron frequency:

$$f_{ce} = \frac{eB}{2\pi m_e} \simeq 9.5\,\mathrm{GHz}. \tag{2}$$

Larmor radius for the ions:

$$r_{ci} = \frac{v_\perp}{\omega_{ci}} \simeq 2.2\,\mathrm{mm}. \tag{3}$$

Larmor radius for the electrons:

$$r_{ce} = \frac{v_\perp}{\omega_{ce}} \simeq 6\,\mu\mathrm{m}. \tag{4}$$

An average $\mathbf{E} \times \mathbf{B}$ drift velocity:

$$\mathbf{v}_E = \frac{\mathbf{E}_o \times \mathbf{B}_o}{B_o^2} \simeq -750\,\mathrm{m/s}\,\hat{\theta}. \tag{5}$$

The Larmor radius of the electron was so small that it can be neglected in all cases. The Larmor radius for the ions, even though it was small, was comparable with the size of the residual plasma (see Fig. 7). Recall that the plasma was a cesium plasma so $m_i = 133 m_p$, where m_p is the mass of a proton.

2.3 Stability Analysis

On the edge of the plasma column, i.e. in the residual plasma region, strong oscillations in the azimuthal electric field $\tilde{E}$ occur (see Fig. 5). This field was measured using the two fixed probes, P_3 and P_4, in Fig. 1(b). These probes were located $14 - 16$ mm from the centre of the plasma column and were carefully aligned to the same DC floating potential to ensure that they only measured the azimuthal component of the electric field. The electric field was calculated by taking the difference in the floating potential obtained from the two probes, i.e. $\tilde{E} \approx -(\phi_{P_4} - \phi_{P_3})/\Delta$, where $\Delta = 7$ mm was the distance between the probes and the sign of $\tilde{E}$ has been chosen according to Fig. 1(b). Fig. 5 shows the spectral distribution for $\tilde{E}$ as a function of the frequency for different aperture bias V_A. For $V_A = 0$ V the spectrum is characterized by a narrow peak at a frequency of approximately 4.5 kHz and its second harmonic at 9 kHz. There is also a large peak at a low frequency. This is believed to come from thermal noise from the plasma and noise coming from the outside through the hot plate. There is only very little energy in the spectrum for frequencies above 25 kHz, irrespective of the aperture bias within the range described here. The peak in the spectra is largest where the radial electric field, $E_o(r)$, is maximum, and by changing E_o, e.g. by decreasing the aperture bias, the peak becomes smaller and its frequency decreases. At a bias close to the floating potential we are left with only a broad spectrum.

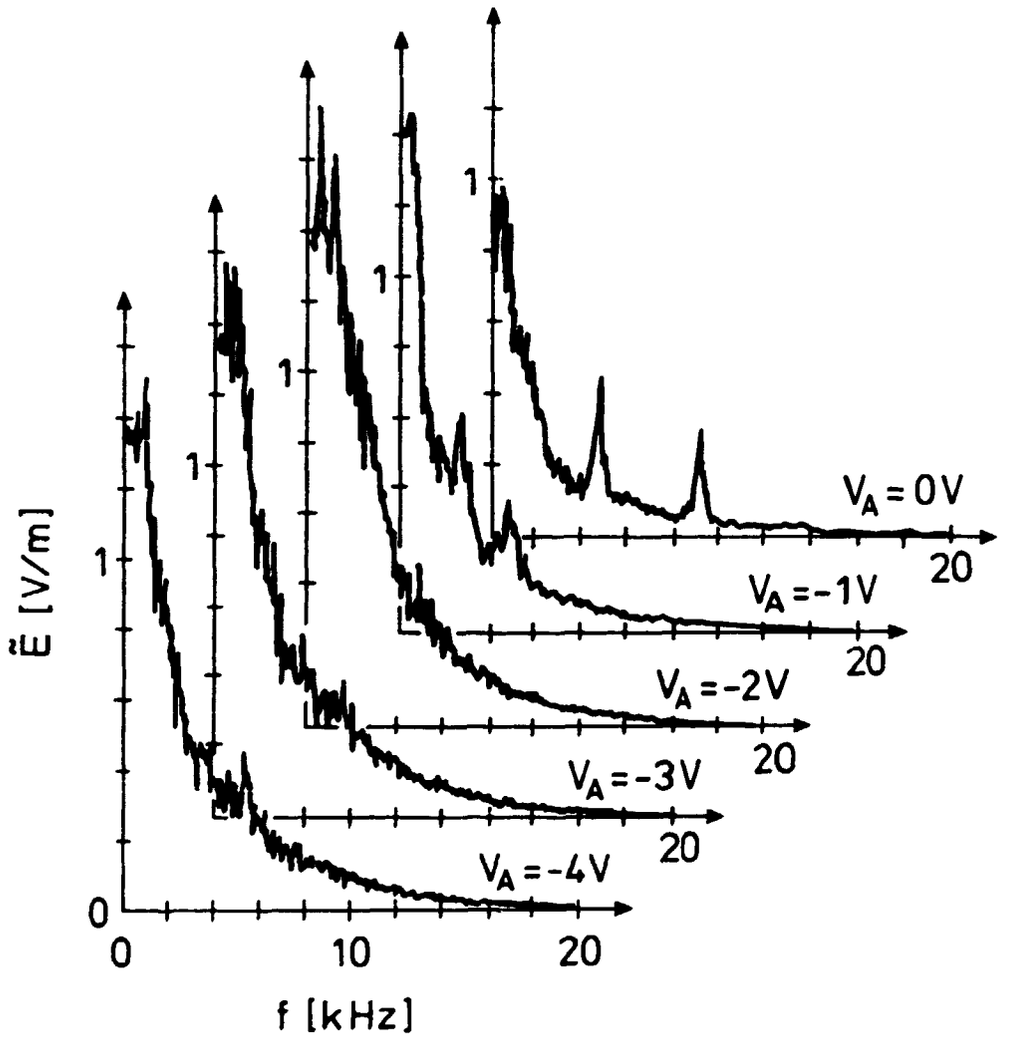

Figure 5. Spectral distributions for the azimuthal $\tilde{E}$-field component obtained for varying aperture bias V_A with $n_o(r = 0) = 5 \times 10^{14} m^{-3}$ and $B_o = 0.35$ T. The bandwidth of the analyzer was 300 Hz.

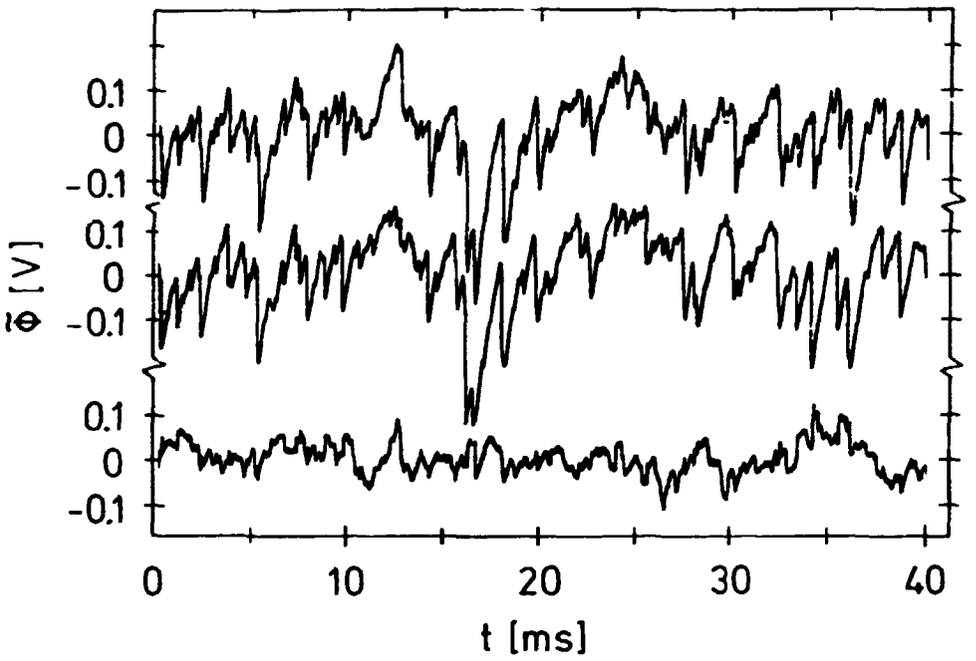

Figure 6. Sample of a typical result of the potential fluctuations obtained by two probes with a 30 cm axial distance and the same radial and azimuthal position. The two upper traces are the two probe signals, while the lower trace shows their difference. Here, $n_o(r = 0) = 8 \times 10^{14}$ m^{-3} and $\mathbf{B}_o = 0.35$ T.

In previous measurements it has been demonstrated that the fluctuations in the residual plasma are characterized by $e\tilde{\phi}/T_e \gg \tilde{n}/n_o(\mathbf{r})$ differing from the usual driftwave scaling where $e\tilde{\phi}/T_e \approx \tilde{n}/n_o(\mathbf{r})$ (Huld *et al.* (1988)). These observations were taken as indicators for the *flute*-type nature of the fluctuations, i.e. the $\mathbf{B}_o$-parallel wavelength is so large that the electrons are incapable of maintaining a Boltzmann equilibrium by flowing along magnetic field lines. By measuring the potential fluctuations by two probes (P_1 and P_2 in Fig. 1(a)) separated axially but at the same radial and azimuthal positions we obtain the result given in Fig. 6. The difference between the two probe signals (lower trace in Fig. 6) is clearly small and indicates that on these slow time scales the magnetic field lines are equipotential to a good approximation. An estimation of a $\mathbf{B}_o$-parallel wavelength component indicates that it is larger than 3 m, i.e. larger than the length of the plasma column. The difference in signal between the two probes originates from a small misalignment of the positions of the probes, the positions being only accurate within the diameter of the probe, i.e. 1 mm, and from small-scale electrostatic fluctuations with a small $\mathbf{B}_o$-parallel phase velocity component, i.e. low-level drift waves. These results were independent of aperture bias within the range used in this context.

To understand the nature of these oscillations, let us look at the radial profile of the electric field. The electric field can be calculated from Fig. 3 and will give rise to an azimuthal $\mathbf{E}_o(r) \times \mathbf{B}_o/B_o^2$ bulk velocity of the plasma. The angular velocity, $\omega_E \equiv E_o/(rB_o)$ is given in Fig. 7 as a function of the radius for an aperture bias of $V_A = 0$ V. It can be seen from the figure that the plasma does not rotate at constant angular velocity, the residual plasma (regions 2 (and 3) in the figure)

has large gradients in the velocity profile and the flow will therefore be strongly sheared in this region. As known from fluid dynamics the shear will give rise to a Kelvin-Helmholtz instability which generates strongly $\mathbf{B}_o$ aligned fluctuations, with frequencies well below the ion cyclotron frequency (Huld *et al.* (1991, 1988), Jassby *et al.* (1972), Kent *et al.* (1969)). A linear analysis of the experimentally obtained velocity and density profiles can be performed using the radial wave equation derived by Rosenbluth and Simon (1965) and Kent *et al.* (1969) by assuming that the low-frequency perturbations have the form $\exp[i(m\theta - \omega t)]$ propagating around the plasma column with density profile $n_o(r)$:

$$(T\psi')' + \{[(1-m^2)/r^2]T + r^2\omega^2 n_o'(r)\}\psi = 0 \ , \tag{6}$$

where

$$T \equiv n_o r^3 \bar{\omega}(\bar{\omega} - m\omega_{di}) \quad , \quad \bar{\omega} \equiv \omega - m\omega_E,$$
$$\omega_{di} \equiv -\frac{T_i}{eB_o r}\frac{n_o'(r)}{n_o(r)} \quad , \quad \psi \equiv \frac{\tilde{E}}{\bar{\omega}} \ .$$

The prime denotes $\partial/\partial r$ and $\tilde{E}$ is the azimuthal component of the fluctuating electric field. If we assume that the density profile is constant, i.e. $n_o'(r) = 0$, we obtain the usual equation for the Kelvin-Helmholtz instability in an ordinary fluid (Chandrasekhar (1961)).

Analytic solutions of equation (6) can be found only for special forms of the functions $n_o(r)$ and $E_o(r)$. Instead we have followed the work of Kent *et al.* (1969) by approximating the profiles of $n_o(r)$ and $E_o(r)$ to be piecewise constant in each of the three regions shown in Fig. 7, with discontinuous jumps at the interfaces.

With this simplification ω_{di} vanishes and $\bar{\omega}$ is constant in each of the three regions. Within each region eq. (6) will then be reduced to:

$$\psi'' + \frac{3}{r}\psi' + \frac{1-m^2}{r^2}\psi = 0. \tag{7}$$

This equation has the solution $\psi = Ar^{-1+m} + Br^{-1-m}$. By requiring that ψ is finite at $r = 0$, vanish for $r \to \infty$ and that $m \geq 1$ the solutions take the forms:

$$\begin{aligned} \psi_1 &= Ar^{-1+m} && \text{(region 1)}, \\ \psi_2 &= Br^{-1+m} + Cr^{-1-m} && \text{(region 2)}, \\ \psi_3 &= Dr^{-1-m} && \text{(region 3)}. \end{aligned} \tag{8}$$

To connect the solutions at the interfaces we use continuity of ψ across the interfaces and derive the jump condition by integrating eq. (6) from $r_s - \epsilon$ to $r_s + \epsilon$ and taking the limit $\epsilon \to 0$. The four constants in eq. (8) can thus be expressed by the parameters given in the problem. It is assumed (i) that $\omega_2 \gg \omega, \omega_1, \omega_3, \omega_{di}$, which is justified by examining the values given in Fig. 7 and eq. (1), and (ii) that the second region is very narrow[1], i.e. $\delta \equiv (r_2 - r_1)/r_1 \ll 1$. Then a quadratic dispersion relation is obtained (Kent *et al.* (1969)):

[1] using the values in Fig. 7 it is found that $\delta \simeq 0.3$ so this approximation is marginally fulfilled.

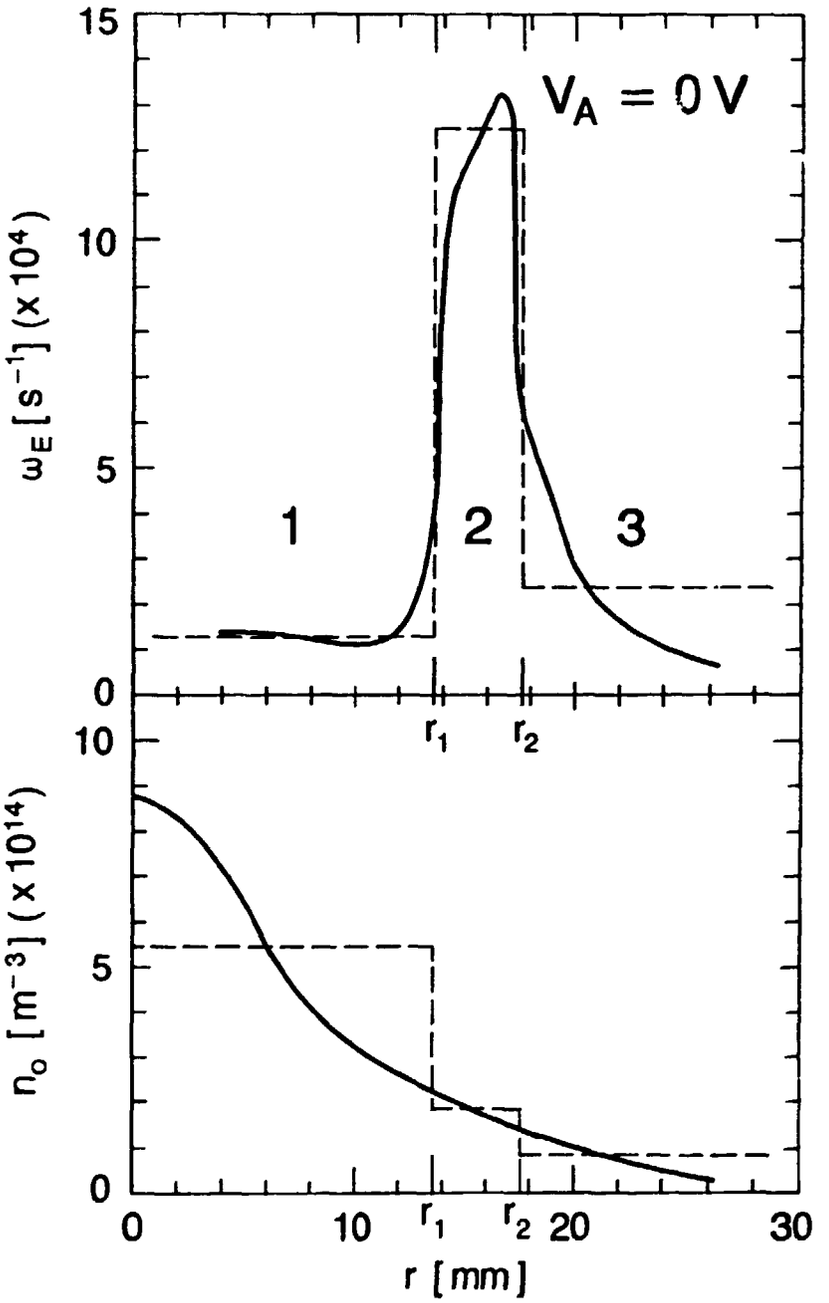

Figure 7. Radial profile of ω_E and n_o (full curves) with the three-region approximation (dashed curves) used for obtaining the dispersion relation (9). The radius r_1 corresponds approximately to the radius of the aperture. The values used are $\omega_1 = 1.3 \times 10^4\ sec^{-1}$, $\omega_2 = 12.5 \times 10^4\ sec^{-1}$, $\omega_3 = 2.4 \times 10^4\ sec^{-1}$, $\alpha_1 = 0.87$, $\alpha_2 = 0.29$, $\alpha_3 = 0.13$. The weak rotation in the central plasma column ω_1 is due to inhomogeneity of the hot plate temperature.

$$\Big[1+\delta\alpha_2(m^2-1)/m\Big]\omega^2 - 2\Big[(m-a)\alpha_1\omega_1 + (m+1)\alpha_3\omega_3 + \delta(m^2-1)\alpha_2\omega_2\Big]\omega + m\Big[(m-1)\alpha_1\omega_1^2 + (m+1)\alpha_3\omega_3^2 + \delta(m^2-1)\alpha_2\omega_2^2 + \gamma(m^2-1)\omega_2(\alpha_3-\alpha_1)\Big] = 0\,, \tag{9}$$

where $\alpha_i \equiv n_{oi}/(n_{o1}+n_{o3})$ and n_{oi}, ω_i are constant values of n_o and ω_E, respectively, in region i. The effect of finite Larmor radius for the ions expressed by the γ term in eq. (9) acts to stabilize the higher mode numbers. Here, $\gamma \equiv (T_i/2eB_o r_1^2)$ and, for our parameters, $\gamma \simeq 3\times 10^3 \mathrm{sec}^{-1}$. Solving eq. (9) using the values given in Fig. 7 reveals that many modes are unstable. The $m=2$ mode, the most commonly mode observed in our experiments, has the frequency: $\omega/2\pi \simeq 7$ kHz. This value is close to the observed frequency, see Fig. 5, where we find a frequency at about 4.5 kHz [2]. Higher mode numbers are also found to be unstable, but these modes were seldom seen in the experiments. Using the same stability analysis for decreasing aperture potential, V_A, will result in nearly the same picture, but the frequency of the $m=2$ mode will decrease with decreasing V_A.

The stability analysis inevitably has its limitations. The most grave one is that we apply a linear theory to a turbulent flow! Nonlinear exchange of energy between the different modes is not incorporated in the linear model. In chapter 3 the two-dimensional Navier-Stokes equations will be solved in an annulus geometry. There the effect of such a nonlinear exchange of energy results in an inverse cascade, where the energy condenses into the lower modes which is consistent with the experimental results. Another limitation is that the width of the strongly sheared region, region 2 in Fig. 7, is only a few Larmor radii for the ions, so a large portion of the ions is not restricted to one region. Taking finite Larmor radius into account one would expect a stabilization of the higher order modes and a decrease of the frequency of modes because the effective rotation frequency of the ions decreases in region 2. Even with those limitations the theory gives results quite close to the experimentally obtained values for the frequency.

2.4 Conditional Analysis

To detect structures that might be present in the strongly sheared flow of the residual plasma, a statistical analysis becomes necessary. We cannot measure the floating potential simultaneously in all points in a plane perpendicular to the magnetic field since we would then have to insert so many probes into the plasma that the features we want to investigate would be totally destroyed. It has been demonstrated that such flows can exhibit coherent structures (or vortices), see e.g. Huld *et al.* (1988) where a correlation analysis of the shear flow was performed. In the present work we use an analysis based on conditional averaging, see Huld *et al.* (1991, 1990). The basic idea of this method is discussed in detail by Johnsen and Pécseli (1987) and has been used to investigate turbulent boundary layers in neutral flows, see Blackwelder *et al.* (1976), and electrostatic fluctuations in the electrojet above Greenland, see Pécseli *et al.* (1989). In these measurement we simultaneously recorded two time series with a sampling rate of 125 kHz using a LeCroy oscilloscope with an 8-bit resolution. The time series were typically of

[2] Considering that we apply a linear analysis to a turbulent flow this is quite a reasonable result.

200 msec duration and we thus have 25,000 points with a time spacing of 8 μsec. This will give us good time resolution when examining fluctuations at 4 kHz, the dominant frequency in the power spectrum in Fig. 5. One of the time series, series A, came from the azimuthal electric field component located in the middle of the residual plasma, i.e. using probes P_3 and P_4 in Fig. 1(b). The other time series, series B, came from the movable Langmuir probe, P_4, and it could thus be a measurement of either the fluctuating floating potential or the fluctuating density. The two time series were obtained for positions of the movable probe in a grid of 13 x 9 positions with 3 mm spatial resolution in the plane perpendicular to the magnetic field. Using the computer program AIDA, see Huld (1990), the time series were stored in a PC-computer for later analysis. The total time of the measurement was about 15 min during which period the plasma parameters were believed to be constant. We found no change in the statistical values if we made two measurements shortly after each other.

Having obtained the measurements, we applied the conditional averaging for each pair of time series. For time series A we searched the record for events fulfilling the conditions: $E_A(t) \geq E_* \mid \partial_t E_A \geq 0$. For large values of the imposed condition E_* this method will reflect the properties of large structures which might be presented in the flow. We have employed the condition: $\partial_t E_A \geq 0$ so that some of the noise would be ignored and consequently did not start the analysis when the condition was fulfilled and decreasing. At each time, $t = t_*$, the condition was fulfilled, we took out a subseries from signal B in the time interval $\{t_* - \tau\,;\, t_* + \tau\}$. The time τ was usually taken to be the correlation time for the signal. Assuming that each time series was statistically independent and that they arose from the same physical conditions, we added these subseries together and divided them by the number of realizations. We thus had an average signal from the movable probe at the position (x, y) under the condition that we had a large electric field in the residual plasma region. The subseries were chosen so that they did not overlap and, depending on the imposed condition, we got about $50 - 300$ realizations per time series. If we imposed a very large condition on the electric field, the number of events would be so low that the thermal noise would be dominant. To clarify the method Fig. 8 shows 3.2 msec of the (a) fluctuating azimuthal electric field, (b) the corresponding potential variations for a probe position 5 mm above the top of the fixed probes, and (c) the resulting conditional time signal obtained using all 200 msec with $\tau = 200\,\mu$sec. In Fig. 8(a) the imposed condition has been set equal to $1.5\,\sigma$, where σ is the root mean square of the fluctuating azimuthal electric field. Five notable positive peaks are seen in the figure, where three of them are above the imposed condition. For the three peaks we find corresponding potential peaks in Fig. 8(b) which will contribute to the average signal. The last two peaks are below the imposed condition and are thus skipped by the analysis. As the potential variations were obtained for a position above the fixed probes, we find that the "structures" corresponding to the two peaks were damped out as there are only very weak variations in the potential. Applying this average to all positions of the probe, we can thus choose a specific time and by using a numerical interpolation scheme obtain the full spatial variation of the potential (density). Note that it is possible to consider times after as well as prior to the reference time where the condition is fulfilled, and that for the same set of data we can apply the conditional averaging method for different values of the imposed condition. We could also have searched for events: $E_A(t) \leq E_* \mid \partial_t E_A \leq 0$ and would thus

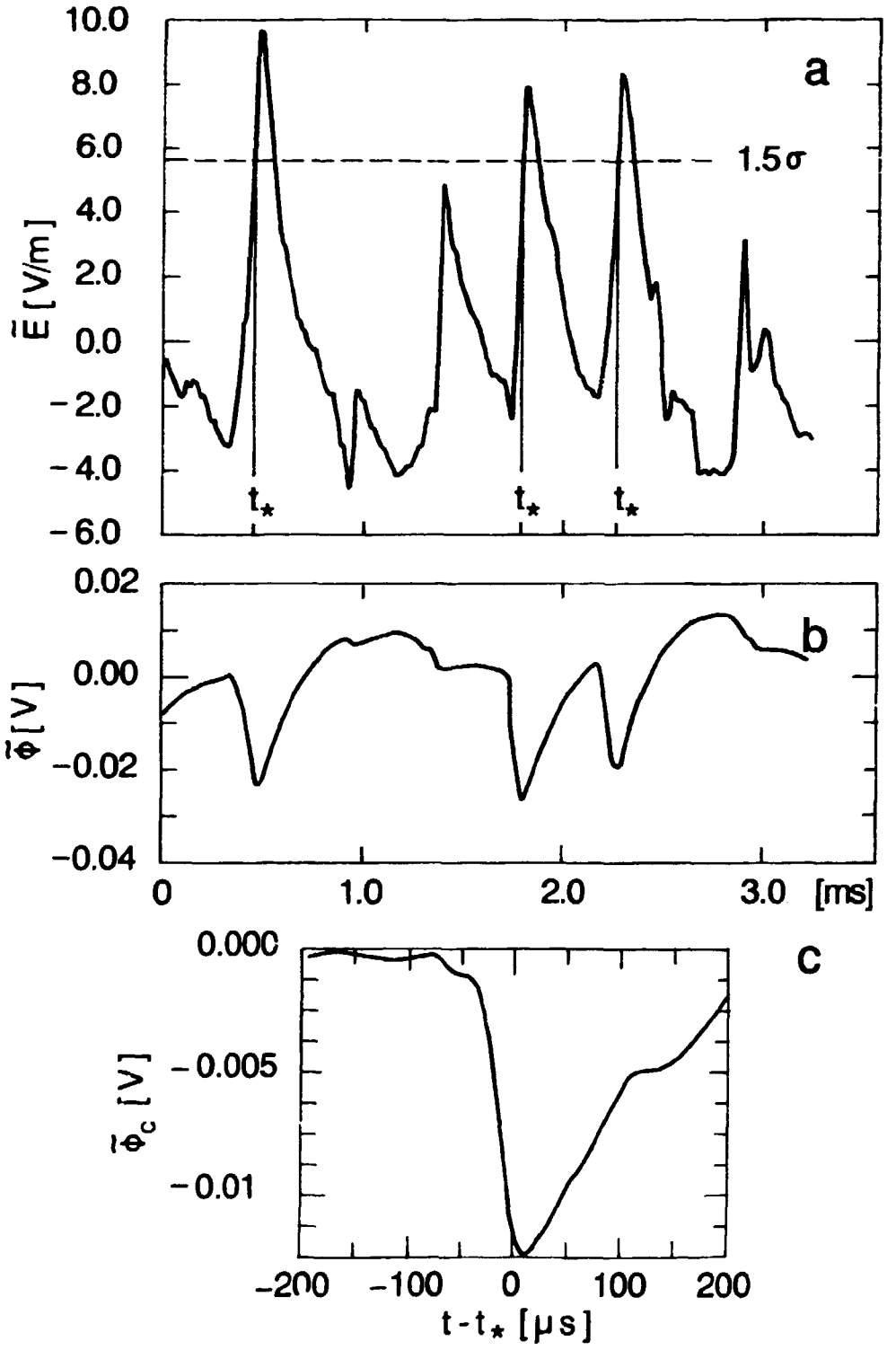

Figure 8. Part of the total time series obtained from the experiments at $x = -17$mm and $y = 10$mm, see Fig. 9. (a) The azimuthal electric field fluctuations of 3.2msec duration. (b) The corresponding potential time variations obtained by the movable probe. (c) The conditional time signal obtained using the total time serie.

examine a negative electric field from time series A.

2.5 Conditionally Averaged Potentials

Applying the conditional analysis to the space-time varying potential detected by the movable probe a time-space potential profile like the one shown in Fig. 9 can be obtained. In such kinds of measurements the fixed probe for measuring the density, i.e. probe 5 in Fig. 1(b), was removed. This analysis was obtained using the condition on the electric field: $E_* = 1.5 < E^2 >^{1/2} = 1.5\,\sigma$ with $\partial_t \tilde{E} > 0$, a density of $n_e(r = 0) = 2 \times 10^{15}\mathrm{m}^{-3}$, $B_o = 0.35\,\mathrm{T}$, and an aperture bias of $V_A = -2.0\,\mathrm{V}$. The frames show the time evolution of the potential profile in the interval [-32 μsec;48 μsec], where the time $t = 0\,\mu$sec was when the imposed condition E_* was fulfilled. The plasma column and the position of the probes for detection of the azimuthal electric field are shown in the panel for $t = 0\mu$sec. We see the formation and the beginning decay of a large monopolelike structure, quickly[3] propagating on the edge of the plasma column. The velocity of propagation can be estimated from Fig. 10(b) to be approximately 300 m/s in the positive direction, i.e. the same direction as the bulk plasma $\mathbf{E}_o(r) \times \mathbf{B}_O/B_o^2$ velocity in the residual plasma region. This DC plasma velocity was found in eq. (5) to be around 750 m/s and is thus comparable with the estimated structure velocity. It is difficult to estimate an exact lifetime of the structures using this analysis; the structure disappears out of the frame in Fig. 9 before it is possible to estimate a decay rate. Fig. 10(a) shows a beginning decay, but this figure was created using the values from the numerical interpolation and is thus subject to uncertainty, and it is not possible to obtain an exact decay rate using this figure. From the conditional analysis it was found that the structures would be damped out before they had performed one cycle around the plasma column. The lifetime is mostly determined by the shear flow. From general fluid dynamics it is known that in some cases small-scale fluctuations in a turbulent flow can condensate into coherent structures. A wellknown realization of this phenomenon is the red spot on Jupiter, where the atmosphere around the equator rotates in opposite direction due to the Coriolis force creating a shear flow in which the red spot is observed. In this case the coherent structure has a very long lifetime; it has not changed much since it was first discovered at the time of the invention of the telescope. In other kinds of turbulence, such as the plasma flow described in the present chapter, the structures have a much shorter lifetime as they are destroyed by the shear flow. In our case there are other mechanisms which determine the lifetime of the structure. The end loss of charged particles is a damping mechanism which is a consequence of the finite length of the plasma column. The friction between the convective $\tilde{\mathbf{E}}_o \times \mathbf{B}_o/B_o^2$-velocity field and the end plate is clearly proportional to the area of the vortices and therefore predominantly acts as a damping on the largest structures, i.e. as an energy drain on large scales. The finite Larmor radii must also be considered when discussing the time evolution. As found in section 2.2, the Larmor radii were about 2 mm, and the particles rotate around the magnetic field lines with a frequency of 40 kHz or, in other words, they will perform one cycle in 25μsec. These values are comparable with the spatial dimensions and the lifetime of the structure. Ions on the edge of the monopole cannot consequently be considered as point charges but will gyrate across the edge to the outside of

[3] quickly means relative to the velocity of structures observed for an lower aperture bias.

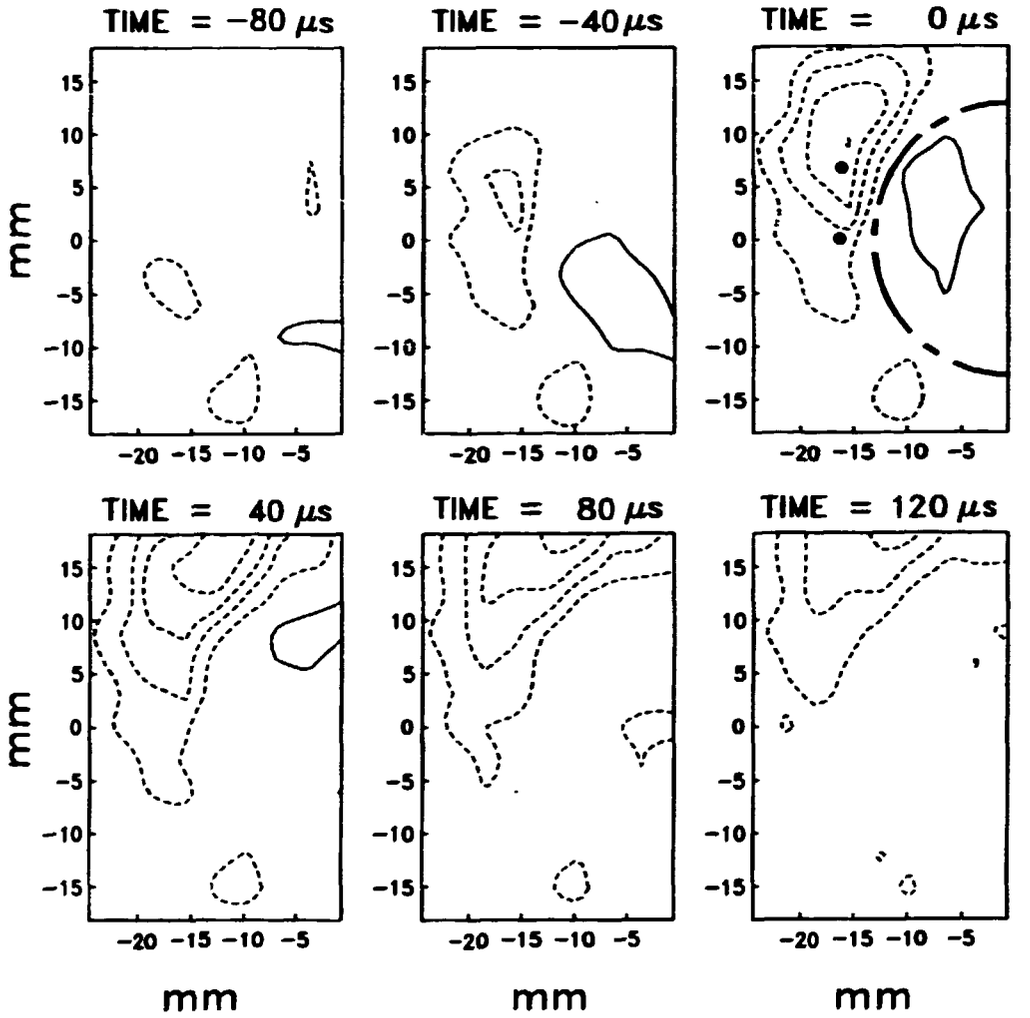

Figure 9. Space-time variation of the conditionally averaged potential obtained for $E_o = 1.5\sigma$ with $\partial_t \dot{E} > 0$. The contour interval is $\Delta\phi = 0.0038$V. Positive potentials are shown as solid lines, negative ones as dashed lines. The zero contour is not shown. The dot-dashed semicircle in the panel for $t = 0$ μsec indicates the projection of the aperture opening. The plasma parameters were: $V_A = -2.0$ V, $n_o(r = 0) = 2 \times 10^{15}$ m^{-3}, and $B_o = 0.35$ T.

the structure. They will thus be exposed to the nonhomogeneous electric field set up by the monopole itself. This feature will clearly set a limit to the steepness of the potential structures. An exact analytical analysis of this feature is difficult to perform. Numerical simulations have shown that finite Larmor radii do play a role for the time evolution and stability of coherent structures, see Knorr *et al.* (1988) where finite Larmor radii to first order have been incorporated in the Euler equation.

It is important to emphasize that the finite lifetime observed by us could also, in principle, simply reflect a "smearing out" due to differences in velocity of propagation of individual structures. We have at present no possibility of evaluating the velocity of individual structures and their decay, but future work in the group will be dedicated to examining this problem.

The potential profile shown in Fig. 9 was obtained using the values of the fluctuating potential in a grid with a 3 mm spatial resolution, a limitation set by our data acquisition system. Details smaller than 3 mm will therefore not be detected. We have performed a more detailed analysis on a restricted region with 1 mm spatial resolution, see Huld *et al.* (1991) and found that even though some small-scale details were lost in these kinds of measurements, the overall dynamics of the flow were the same. This is consistent with the fact that the electric field was obtained with a spatial distance of 7 mm. Structures smaller than this spatial distance will therefore not be detected by our conditional analysis. In principle, small structures may be present in the flow but they are unlikely to have any serious influence on the dynamics of the flow and can be considered as being part of the overall small-scale fluctuations.

By changing the imposed condition to $E_* = -1.5\,\sigma$ together with $\partial_t \tilde{E} < 0$ the result in Fig. 11 is obtained. Notice that the figure was obtained using the same data as the ones used to produce Fig. 9. Again a monopole-type structure is observed but the strength of the structure is now smaller. These results show that a positive electric field, measured by the two fixed probes, has greater probability than a negative one. A close examination of Fig. 9 reveals that the structure is not symmetric, and positive fluctuations of the electric field on the rear side of the structure are numerically stronger than the negative fluctuations on the front. In other words the monopole-type structures have significant skewness, with steepest potential gradients on the rear sides. By the present methods we can only obtain an average structure, and what we see could just be differences in size and amplitude of structures being summed. The hypothesis is, however, strengthened when analyzing the probability distribution for the electric field obtained by the fixed probes, as shown in Fig. 12. The figure was obtained using all 9×13 time series of the electric field from the data which produced Figs. 9 and 11, i.e. using 2.9 million values, and is thus very accurate. Here the distribution is found have significant positive skewness, $S = 0.67$ so that positive electric fields have greater probability than negative ones and that might be connected to the turbulent structures shown in Figs. 9 and 11. Fig. 12 also reveals a kurtosis of $K = 3.6$, noticeably exceeding the value 3 which characterizes a Gaussian distribution.

The creation of the structures is strongly influenced by the plasma parame-

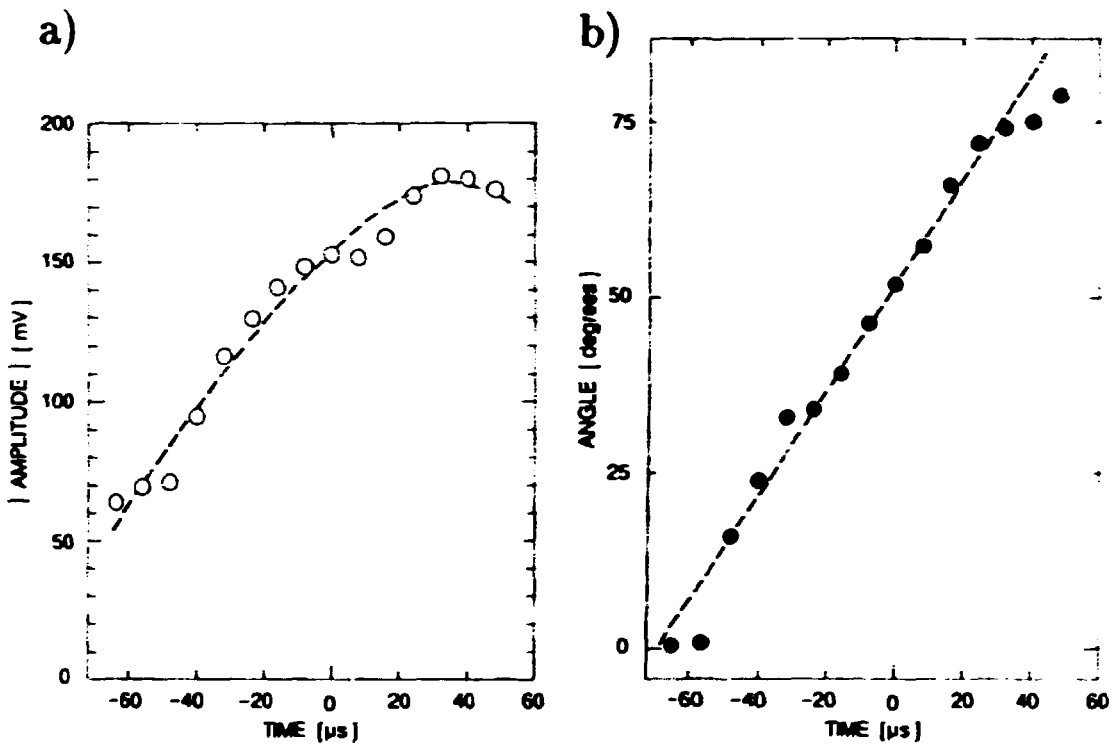

Figure 10. The numerical value of the peak amplitude in (a) and angular position in the azimuthal direction in (b) of the monopole structure in Fig. 9.

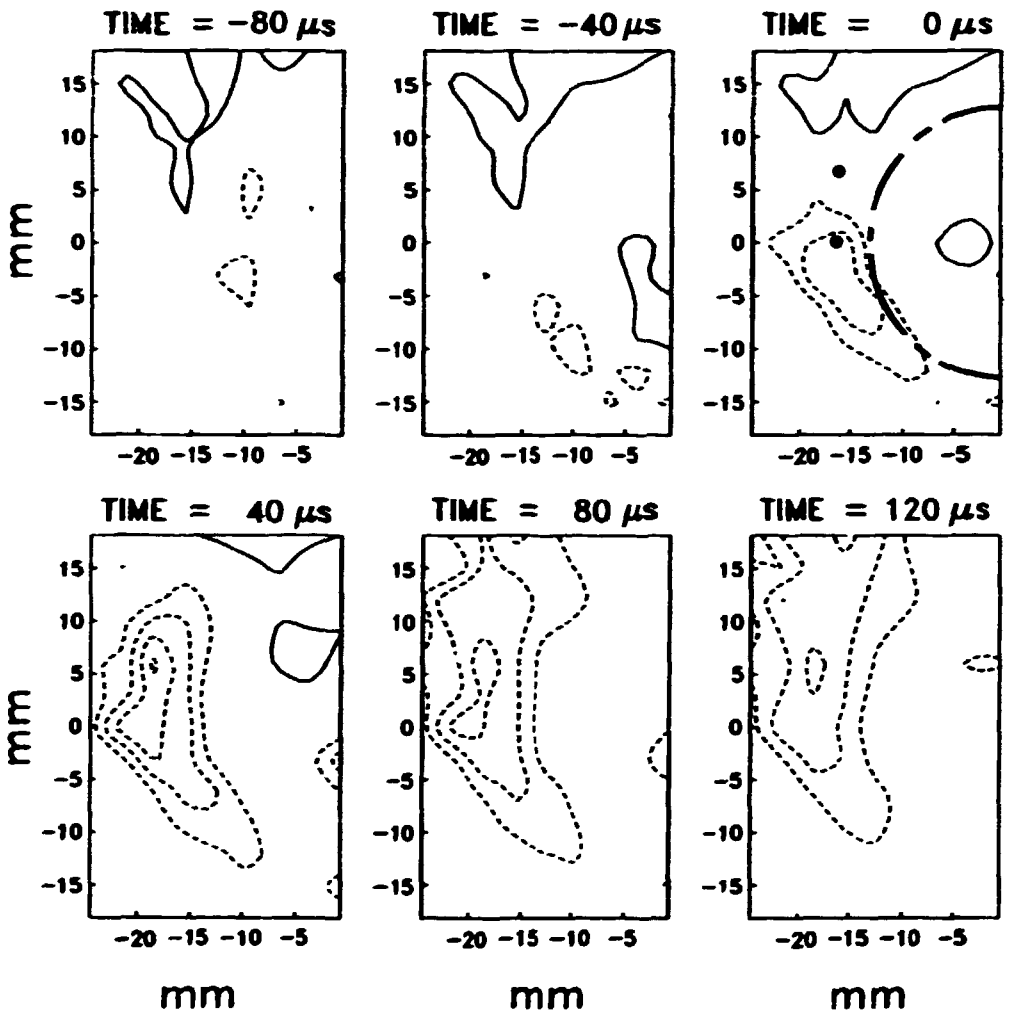

Figure 11. Results corresponding to Fig. 9 with $E_o = -1.5\,\sigma$ with $\partial_t \tilde{E} > 0$. The contour interval is $\Delta\tilde{\phi} = 0.025$ V.

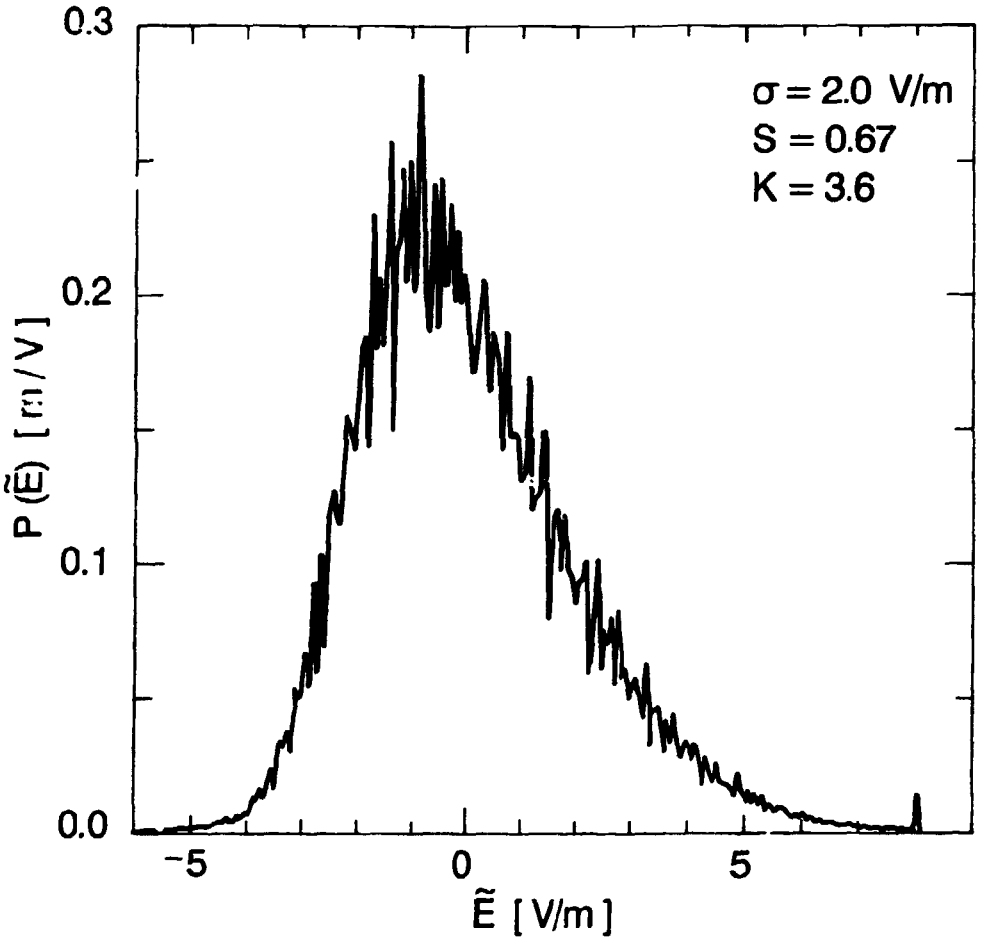

Figure 12. Amplitude probability density obtained for the azimuthal electric field component. The rms value of the fluctuations is $\sigma = 2.0$ V/m, skewness, $S = 0.67$, and the kurtosis, $K = 3.6$. The plasma parameters are as in Fig. 9.

ters, with the DC-potential profile as the most important parameter. This parameter determines the size and strength of the shear flow. Also the density and the strength of the magnetic field are important. In Fig. 13 the time evolution of the flow is shown using an aperture bias of -3.3V, a plasma density of $n_o(r = 0) = 6 \times 10^{14}\mathrm{m}^{-3}$, and a magnetic field at $B_o = 0.275$T. For this low-aperture bias close to the plasma floating potential we obtain large average structures in the form of long-lived double vortices. These structures are almost stationary which is in agreement with the small $\mathbf{E}_o(r)$ values obtained for the present values of V_A, see Fig. 3(c). The eigenvelocity of the double vortex is estimated to be around 20 m/s. In the 200 μsec time interval shown in Fig. 13 the displacement is around $2-4$ mm in the counterclockwise direction. That it rotates the "wrong" way around the plasma column may apparently seem strange, but when examining Fig. 3(c) more closely it is noticed that in the outer region of the residual plasma the radial electric field actually points outwards and will thus result in a (small) counterclockwise bulk plasma $\mathbf{E}_o(r) \times \mathbf{B}_o/B_o^2$ propagation.

The long lifetime of double vortices in Fig. 13, as compared with monopoles in Figs. 9 and 11, does not justify the interpretation of double structures as being particularly robust. The bulk plasma flow is strongly sheared in Figs. 9 and 11, while the vortices in Fig. 13 propagate in an almost shear-free region, see Fig. 3(c). The source region of the instability is localized to the fringe in the potential, separating the central and residual parts of the plasma column. The large amplitude electrostatic fluctuations generated by the instability are spread over a larger region, as seen in numerical studies of related instability (see, e.g., Horton *et al.* (1987)). In the central part of the plasma column the fluctuations are heavily damped by the short-circuiting effect of the hot plate and large structures are consequently observed only in the residual plasma. Strictly speaking, an observation of two vortices next to each other in a conditionally averaged potential cannot guarantee that they are simultaneously present in each realization. With these kinds of measurements, where we only have access to the electrical field from the fixed probes, it is not possible to prove that they are a result of the same realization.

Using the ion saturation current so that the movable probe could detect fluctuations in plasma density, one can obtain the conditionally averaged density variations corresponding to the potential variations shown already. The results obtained for the same condition as Fig. 13 are shown in Fig. 14; the results were obtained shortly after each other so the plasma condition did not change. The fluctuations in density were normalized in each spatial grid position by the DC density like the one shown in Fig. 4. Here we find a much more complicated time evolution than the corresponding potential. The fluctuations in density are small, about 10 % compared with the DC density, but the potential structures are clearly associated with variations in density. The first noticeable difference is that there are more density structures with shorter lifetime than potential structures. Furthermore, they do not only propagate around the plasma column, but also have a radial propagation. These features, together with the fact that the density structures seem to occur between the two potential structures, indicate that the potential dipole causes plasma to be transported out of the plasma column in a burst-like manner. In order to examine the importance of the transport due to coherent structures one has to calculate the plasma flux more precisely. This will be done in the next section.

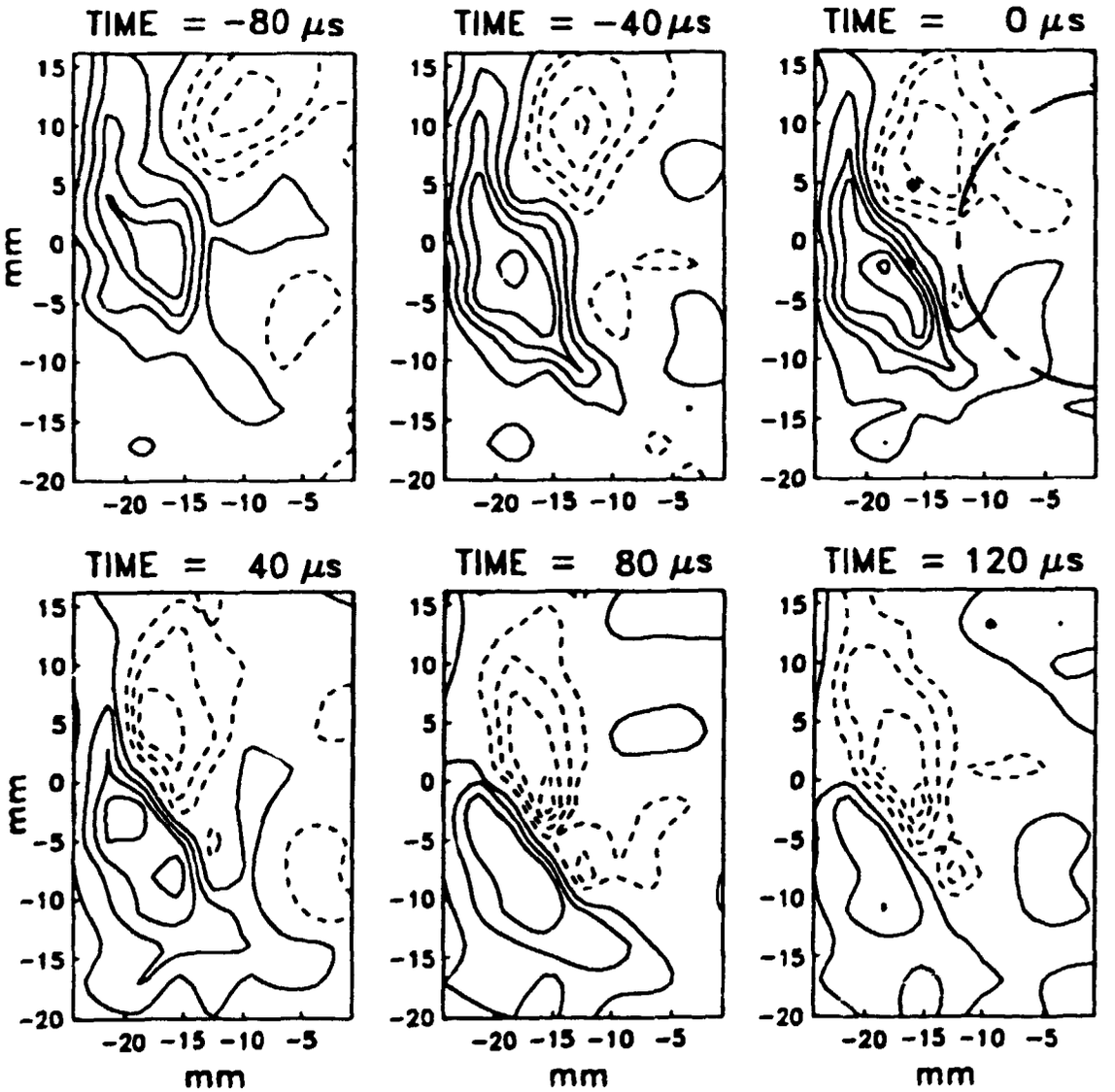

Figure 13. Space-time variation of the conditionally averaged potential obtained for $E_* = 1.5\sigma$ with $\partial_t \tilde{E} > 0$. The aperture bias was $V_A = -3.3$ V. The contour interval is $\Delta\tilde{\phi} = 0.0007$ V. Here $n_o(r = 0) = 6 \times 10^{14}$ m^{-3} and $B_o = 0.275$ T.

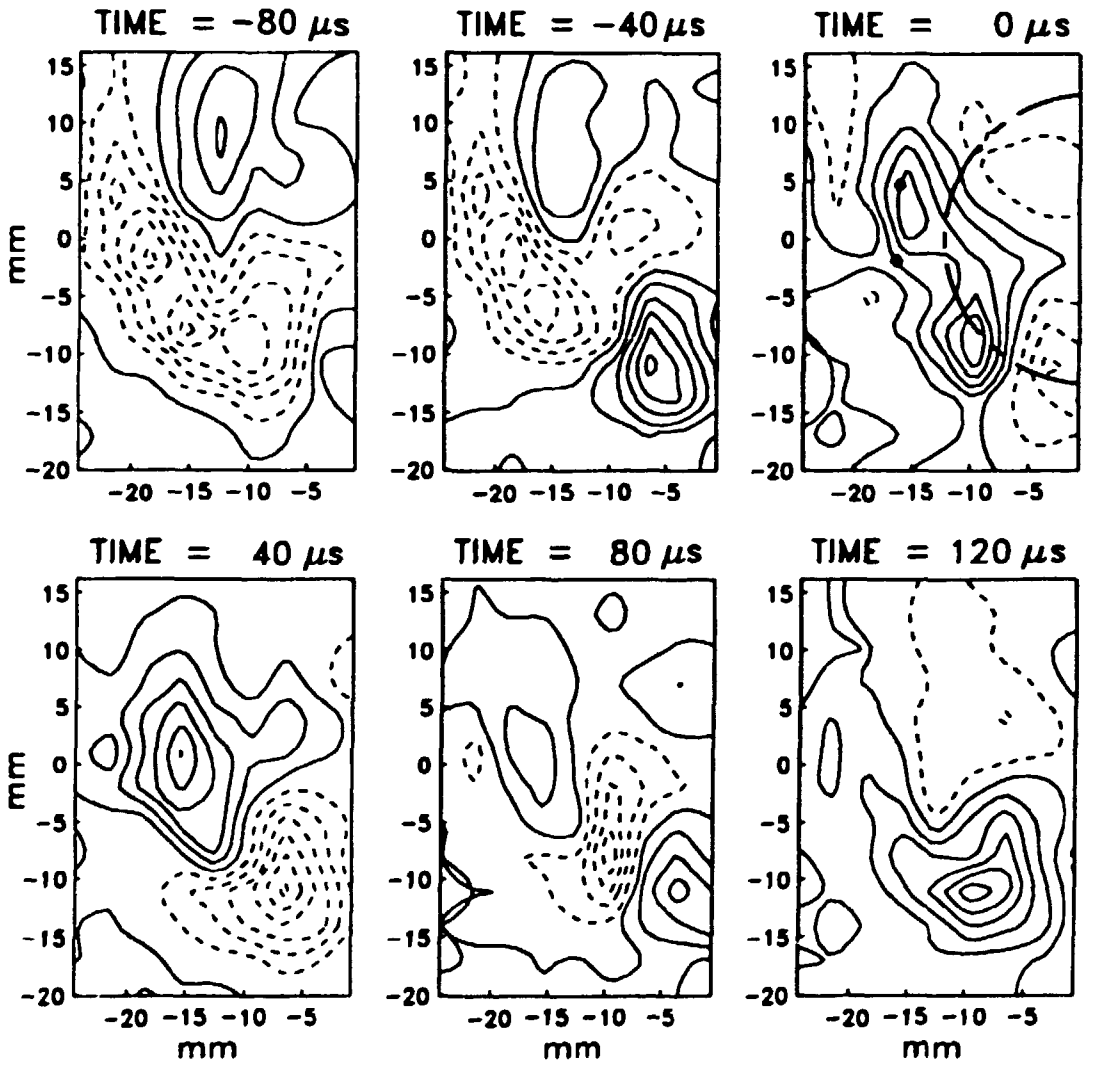

Figure 14. Space-time variation of the conditionally averaged relative plasma density fluctuations $\tilde{n}/n_o(r)$, obtained for the same conditions as in Fig. 13. The contour interval is $\Delta\tilde{n}/n_o(r) = 0.03$.

2.6 Flux Measurement

When investigating the flux of plasma diffusing from the plasma column, one could use the results from the potential and the density fluctuations, for example the ones shown in Figs. 13 and 14, to calculate such a flux. That would mean that we have to derive the azimuthal electric field from the spatial potential variations, and since these quantities were obtained with 3 mm spatial resolution, the uncertainty of the result would be too considerable. Instead, we will restrict this analysis to the plasma flux at the reference position using the signal from the three fixed probes. Due to the approximate cylindrical symmetry of the problem, all azimuthal positions are essentially statistically equivalent for a given radial position. The radial flux is defined as: $\Gamma \equiv v_r n$. Splitting the two terms from this equation into a DC and a fluctuating value and using the E_θ/B_o for the radial velocity, a general form for the radial flux is obtained:

$$\begin{aligned} \Gamma &= \frac{1}{B_o}(E_{o\theta} + \tilde{E})(n_o + \tilde{n}) \\ &= \frac{1}{B_o}(\tilde{E}n_o + \tilde{E}\tilde{n}) \,, \end{aligned} \tag{10}$$

where $E_{o\theta} \equiv 0$ because of rotational symmetry. The first term on the right hand-side of eq. (10) is of no interest in this context since $< \tilde{E} > n_o = 0$. This term will not contribute to any average transport of plasma as it will only cause an oscillation in the radial direction. It is thus appropriate to evaluate only the last term from eq. (10):

$$\tilde{\Gamma} \equiv \frac{\tilde{E}\tilde{n}}{B_o} \,, \tag{11}$$

and its time average:

$$\Gamma_o \equiv < \tilde{\Gamma} > \,. \tag{12}$$

The average value is the net plasma transport out of the plasma column which is due to the low-frequency electrostatic *flute*-type fluctuations. It depends on the plasma conditions, the DC-potential profile being the most important condition. This profile can be controlled through the aperture bias, and Γ_o as a function of the bias is shown in Fig. 15. The plasma conditions were here the same as in Fig. 13. For V_A around ground potential the net flux is very small, which is consistent with previous results, see Huld *et al.* (1988). The spectrum is dominated by narrow frequency peaks, but because $\tilde{\phi}$ and $\tilde{n}$ are virtually in counterphase, there is no significant plasma transport. As the aperture bias decreases from $V_A \sim -1.5$V towards the plasma potential, Γ_o changes rapidly, having a maximum at about -2.7V and finally reaches a kind of plateau when V_A is around the plasma potential. The increase in the net plasma flux can be explained when examining Fig. 3. When decreasing the aperture bias, the electrical field also decreases and the fluctuations can occupy a larger part of the residual plasma measured in the radial direction. The time evolution of the coherent structures would therefore be slower, in Fig. 13 it is seen that they are nearly stationary, and they would have a longer lifetime. From Fig. 13 it can be seen that the potential structures are dipoles and 90° out of phase with the density fluctuations (see Fig. 14). This will result in a burst-like transport, where the dipole bursts a large portion of plasma out of the column.

A diffusion coefficient can, at least formally, be defined by: $D \equiv \Gamma_o / \mid dn_o/dr \mid$. We find a typical value of $D \sim 10^{-3} m^2 \mathrm{sec}^{-1}$ for $V_A < -1$ V, which is somewhat

less than the Bohm value obtained for the present plasma conditions, but significantly larger than the diffusion coefficient due to collisional transport. The latter contribution is not incorporated in these measurements as we have no access to single particle movements. It is thus appropriate to consider these results as evidence for turbulent transport.

The nature of the turbulent transport cannot be understood only by simple measurement of Γ_o. The turbulent transport can be caused by small random displacements, corresponding to a diffusion-like process, or it can be due to large sporadic bursts caused by large coherent structures as the ones shown in the previous section. In order to examine the turbulent transport we have applied the conditional average method to the fluctuating flux, i.e. calculated $< \tilde{\Gamma}(t) \mid \tilde{E} \geq \xi\sigma >$. Similar to the potential and density variations, one can examine the flux when the azimuthal electric field is large, i.e. when coherent structures may be present in the flow. Fig. 16 shows examples of this for $\xi = 0.5$, 1.0 and 1.5 with the same plasma parameters as in Fig. 13. An oscillatory variation of the conditional flux is observed due to the propagation of the double vortex. The forms of the curves are nearly identical, although there is a noticeable phase shift for the minima of the curves. For the maximum value and for the two local maxima we see that they increase for increasing ξ. Larger structures will result in a larger net plasma flux; recall that the curves are averaged so there is no information of how many times the condition has been satisfied. For average times larger than the correlation time, τ, the signal will be uncorrelated with the signal at the reference time $t = t_*$, and we therefore measure the DC value of the flux Γ_o. Integrating the curve for different values of the imposed condition within the correlation time will give us information about the importance of the averaged structures. To evaluate how much the coherent structures dominate the net plasma flux, it is necessary to incorporate the number of times the condition has been satisfied. One way of evaluating this problem is by defining a quantity $\Lambda(\xi)$ (Huld *et al.* (1991, 1990)):

$$\Lambda(\xi) = \frac{N(\xi)}{T} \int_{-\tau}^{\tau} < \tilde{\Gamma}(R,t,\eta_o) \mid \tilde{E} \geq \xi\sigma > dt \,. \tag{13}$$

$N(\xi)$ is the number of realizations containing occurrences of the condition in the records for $\tilde{\Gamma}$. $N(\xi)$ is of course proportional to the total length of the record T.

Performing the integration in eq. (13) for various values of ξ, we obtain the result shown in Fig. 17. For large negative values of ξ the imposed condition is always satisfied and we thus calculate the flux from the total record, i.e. $\Lambda\,(\xi \rightarrow -\infty) = \Gamma_o$. For positive values of $\xi \geq 1$ we only get contributions from the coherent structures[4]. If the flux is only related to these coherent structures, we will expect to find a step-like curve, where the step occurs for a certain (large) value of ξ, the value correspondens to the electric field of the structures. If it is only related to small-scale fluctuations it will slowly tend to zero for some small (positive) value of ξ. From the curve it is seen that we have a situation somewhere between these two realizations with a moderate slope of the curve. Choosing a value of ξ at 1.5, which is a reasonable value to distinguish between small-scale fluctuations and coherent structures, we see that small-scale fluctuations account for approximately 50% of the total turbulent flux, while the remaining 50% are caused by structures for which $\tilde{E}$ exceeds 1.5. Two different kinds of explanation of this feature can be given. It is either due to the fact that coherent structures are not so effective in

[4] The random noise will be averaged out.

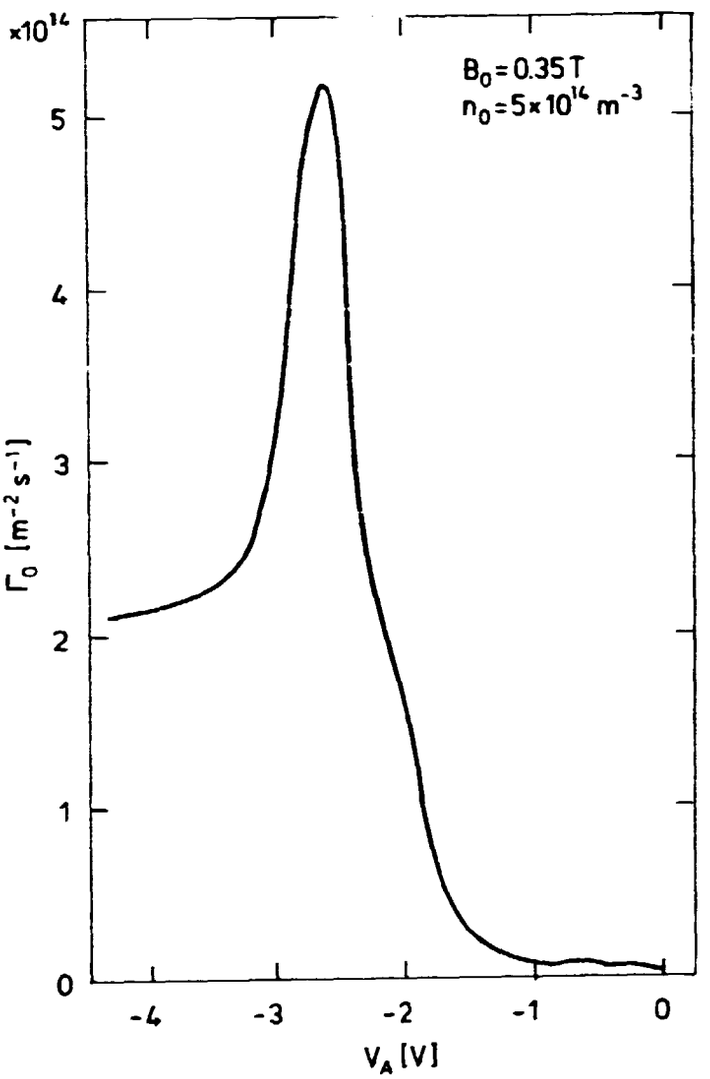

Figure 15. Variation of the averaged plasma flux Γ_o out of the plasma column as a function of the aperture bias V_A. Plasma conditions are as in Fig. 13.

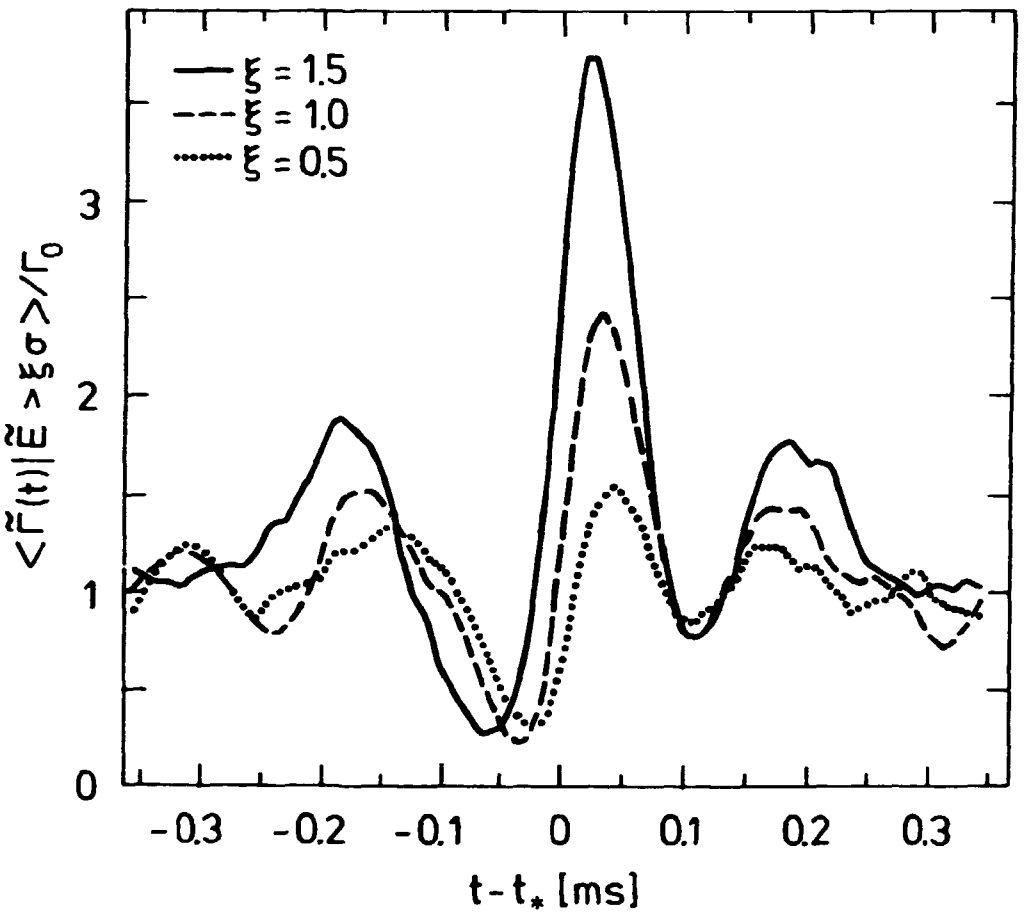

Figure 16. Conditionally averaged flux $< \tilde{\Gamma}(t) \mid \tilde{E} \geq \xi\sigma >$ at a reference position at $R = 16$ mm for three different values of ξ. The plasma parameters are as in Fig. 13

the transport of plasma - when this is compared with the result from Fig. 15 this should actually not be the case - or due to the fact that the number of realizations of these structures is small compared with the length of the record T. To clarify this Figs. 18(a) and (b) show the number of realizations the imposed condition $\tilde{E} > \xi\sigma$ has been satisfied (this curve can be viewed as a density of occurrence) and the flux associated with one realization of a certain amplitude of the structures, respectively. For large negative values of ξ we inevitably obtain the value $N(\xi \ll 0) \simeq 2T/(2\tau)$ and the flux of one realization is $2\tau\Gamma_o/T$, quite an understandable result as the imposed condition, $\xi \ll 0$, is always satisfied throughout the record. When ξ exceeds zero, $N(\xi)$ decreases rapidly and for $\xi \geq 4$ it is almost zero; there are no structures with an electric field larger than 4σ. The associated flux increases in the same interval nearly four times with a nearly exponential form. This demonstrates that individual structures are actually quite efficient in the transport of plasma, but since the relative number of these structures is small they cannot dominate the entire flux.

For an aperture potential near the plasma potential the turbulent transport can be considered as being composed of two nearly equal contributions. One part comes from the small-scale fluctuations which cover a large radial distance. This process will be a diffusion-like process, where the "random" variation of the az-

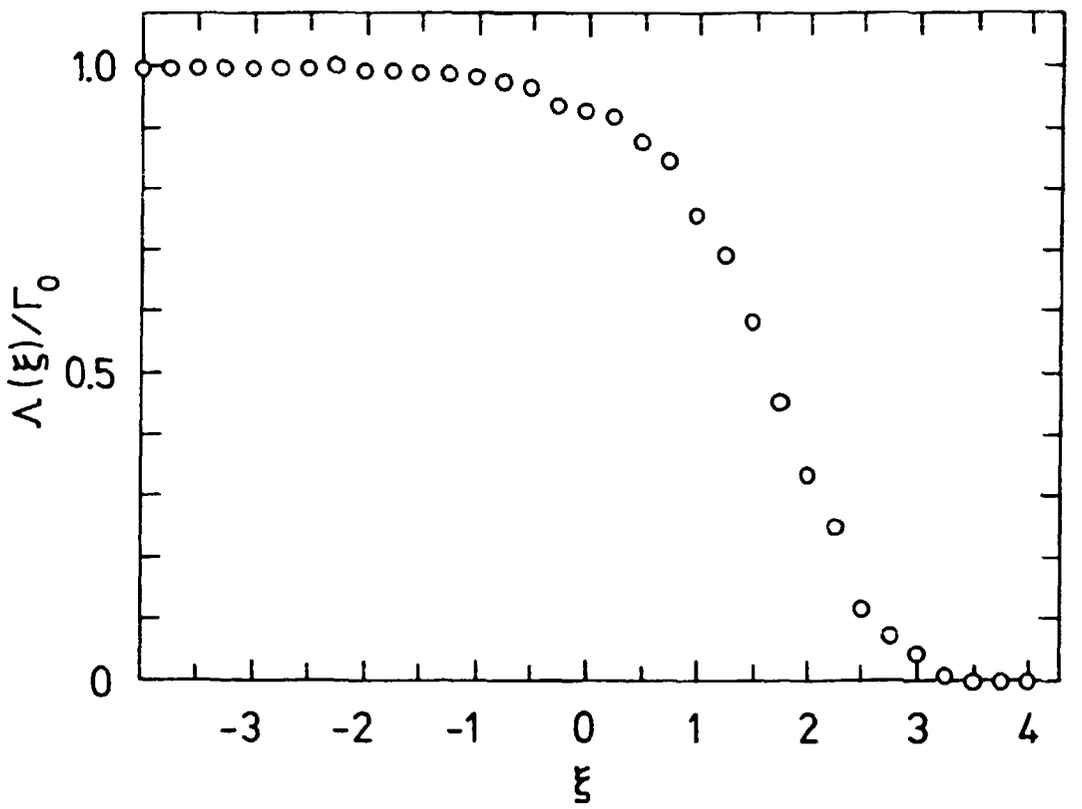

Figure 17. Normalized variation with ξ of the time-integrated conditionally averaged flux $\Lambda(\xi)$. The normalized quantity is $\Gamma_o \approx 5 \times 10^{13}\ m^{-2}sec^{-1}$. The plasma parameters are the same as in Fig. 13.

imuthal electric field will transport plasma due to the gradient of the density in the residual plasma region. The second contribution originates from large coherent structures in this case dipoles which, when they appear, dominate the flow and cause large bursts of plasma going out of the plasma column. When we perform the same analysis for an aperture potential around the ground potential, we find no noticeable net plasma flux. That is due to the fact that the residual plasma region is in this case smaller and that the structures present in the region are monopoles. In this case it has been found that, even though monopoles appear nearly as often as dipoles, they will not cause any noticeable plasma flux.

2.7 Conclusions and Discussions

The purpose of the study described in this chapter was twofold. First, the detection of large coherent structures in the turbulence generated by the Kelvin-Helmholtz instability using a statistical method. The analysis was then extended for analyzing the importance of the observed structures for the radial plasma flux across magnetic field lines.

Using a conditional analysis a full space-time evolution of averaged potential and density variations could be obtained since the fluctuations were time-stationary in a statistical sense. We had to apply a statistical method since instantaneous measurements of the full spatial variations of density and potential would require probes in each of the 9 x 13 grid points used for our analysis.

The formation and propagation of large vortex-like structures were observed

in the residual plasma region. Depending on plasma parameters these vortices could appear as monopoles, see Fig. 9, or as dipoles, see Fig. 13, although for certain cases rather irregular structures could appear. Our results are thus not supporting any preference for dipole-like vortices. It is interesting that analytically it is possible to find steady-state solutions to dynamic equations for certain two-dimensional flows (Horihata *et al.* (1990)) even when a velocity shear is present. In particular, monopole as well as dipole solutions can be obtained. Evidently, it is of interest to interpret our results in terms of such steady-state solutions that have been properly generalized to our conditions. The formation of vortices is, however, the central problem which still has not been fully resolved. The driving mechanism for the turbulent fluctuations is identified as the velocity shear, i.e. the Kelvin-Helmholtz instability. It is found, however, that all scales are unstable down to those comparable with the ion Larmor radius, where they are damped by ion viscosity. The formation of predominantly large scales is accomplished by an inverse spectral cascade, which is characteristic of two-dimensional turbulence. In chapter 3 this inverse cascade, i.e. generation of large-scale structures from smaller ones, is simulated in an annulus geometry using the Navier-Stokes equation. Once formed, the large vortices could in principle approach one of the steady-state solutions. It is more likely that the vortices damp out because of the influence of the small-scale fluctuations which are present in the spectrum at a level which is continuously maintained by the Kelvin-Helmholtz instability. Also the friction between the structures and the end plate acts as an energy drain on the coherent structures.

In the second part of our study we estimated the importance of large structures on the anomalous transport of plasma across the magnetic field lines. We feel able to argue that although a significant part of this transport can be attributed to large amplitude coherent structures, it is not solely caused by them. A nontrivial part of the anomalous transport, or turbulent diffusion, takes place in time intervals where no large structures are present. This interpretation is consistent with previous studies of turbulent diffusion, see Huld *et al.* (1988).

Although our results are carried out in a specific device, it should be noted that the basic characteristics of the turbulence discussed in this chapter are similar to results from the ISX-B tokamak, see Hallock *et al.* (1987), and to similar experiments, see Wootton *et al.* (1989), which indicates that we are dealing with universal phenomena. It is thus reasonable to expect that the basic properties of the vortex-like structures generated by the Kelvin-Helmholtz instability will be characteristic of other plasma conditions as well. Turbulent plasma transport is recognized as being important to, for instance, tokamak devices. Our results may be applicable to such experiments in the part of the plasma which is terminated by limiters (the scrape-off layer), but some of our conclusions may, obviously, have to be reinterpreted. While large structures did not have a dominant importance in our experiment, they may have serious consequences in a tokamak. A burst of hot plasma hitting the wall of the confining vessel can have a lasting influence because of, e.g., the resulting sputtered material, even if such bursts rarely occur.

Our results contain an interesting similarity to the transition between L and H modes as observed in tokamaks, see ASDEX Team (1989). Numerous investigations have indicated that the gradient in the radial electric field of a tokamak plasma is a key parameter in controlling a transition between regions characterized by a low radial plasma transport with corresponding steep density profiles

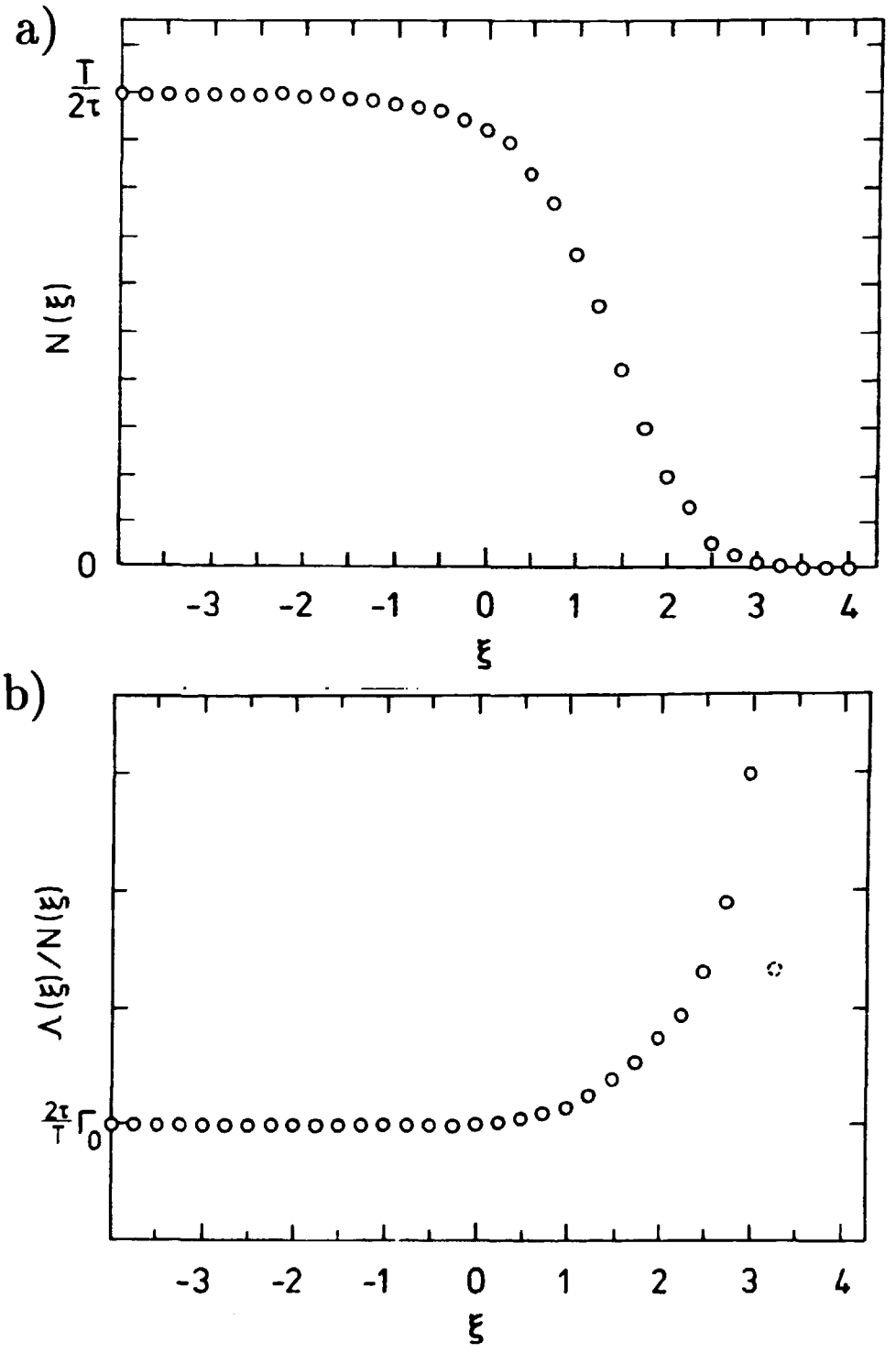

Figure 18. (a) Variation of the number of realizations $N(\xi)$ that contain occurrences of the imposed condition $\dot{E} > \xi\sigma$. (b) Variation of the integrated flux contribution $\Lambda(\xi)/N(\xi)$. The plasma parameters are the same as in Fig. 13.

(H mode) and another region where the density gradients are flattened by an enhanced transport which is apparently due to anomalous diffusion caused by turbulent fluctuations (L mode). Our experiments demonstrate that, although azimuthally propagating, electrostatic waves in the edge plasma in our Q-machine are unstable with respect to the Kelvin-Helmholtz instability and two basically different modes of operation can be obtained through varying the aperture bias. In one mode of operation which is characterized by steep radial potential variation localized to a narrow channel surrounding the plasma column we observed coherent structures, where the phase between density and electric field variations was locked to a value close to $\pi/2$, i.e. density and potential are essentially in counterphase. In this case it was demonstrated that the net plasma flux caused by the fluctuations was very small. In the other extreme case, for relatively gentle radial potential variations, fluctuations characterized by a broadband spectrum were obtained. In this case the fluctuations caused a significant net radial plasma transport out of the plasma column, as monitored by the averaged $\tilde{n}\tilde{\mathbf{E}} \times \mathbf{B}/B_\phi^2$ flux. It seems as if all the individual frequency components constituting the spectrum are incapable of maintaining, simultaneously, the phase between density and potential at the value that minimized the plasma flux.

3 Navier-Stokes Equations

3.1 Introduction

In the Q-machine experiments the plasma was confined by a strong uniform magnetic field, $\mathbf{B}_o = B_o \mathbf{e}_z$, and the fluctuations in the electric field occur perpendicular to this field. In Chapter 2 a two-dimensional approach for this problem was shown to be valid when frequencies below the ion cyclotron frequency were considered. To simulate the dynamics from these experiments the two-dimensional Navier-Stokes equations will be used, which are well known equations from neutral fluid dynamics. The equations are based on the conservation of momentum, where Newton's second law of motion is applied to an element of the fluid and have, in the incompressible case $\nabla \cdot \mathbf{v} = 0$, the form (see, e.g., Batchelor (1967) or Currie (1974)):

$$\frac{\partial \mathbf{v}}{\partial t} + (\mathbf{v} \cdot \nabla)\mathbf{v} = -\frac{1}{\varrho}\nabla p + \mathbf{f} + \nu \nabla^2 \mathbf{v}, \tag{14}$$

where ϱ is the density, ∇p the pressure gradient, $\mathbf{f}$ a body force, and ν the kinematic viscosity of the fluid. Taking the curl of eq. (14) on the assumption that the density is constant throughout the flow and introducing the vorticity $\underline{\omega} \equiv \nabla \times \mathbf{v}$ yield:

$$\frac{\partial \omega}{\partial t} + \mathbf{v} \cdot \nabla \omega = \nu \nabla^2 \omega + \nabla \times \mathbf{f}, \tag{15}$$

where $\underline{\omega} = \omega(x, y)\mathbf{e}_z$ can be treated as a pseudoscalar as it always points in the $\mathbf{e}_z$-direction for a two-dimensional flow. We are now solving the equations using the vorticity as a variable and can use the definition of the vorticity to determine the fluid velocity. Another way is by introducing the stream function ψ:

$$\mathbf{v}(x, y) \equiv \nabla \psi(x, y) \times \mathbf{e}_z \tag{16}$$

and relate ψ to the vorticity through the Poisson equation:

$$\nabla^2 \psi = -\omega\,, \tag{17}$$

which is sometimes easier to handle.

Using the plasma approach instead of the neutral fluid introduces some minor differences which I would like to emphasize here. Equation (14) can be obtained in two general ways, either through kinetic theory by taking the second moment of the Boltzmann equation or through MHD theory, see e.g. Chen (1974). The pressure term here includes both the particle pressure and the magnetic pressure. Please note that in the Q-machine experiments the magnetic pressure is much larger than the particle pressure as the density in the experiments was very low, so $\nabla p \simeq 0$. A viscosity term can be used in our case even though viscosity is normally associated with collisions. In the Q-machine experiments the mean free path of the particles was several times the length of the plasma column and collisions could therefore be ignored. There is another effect which justifies the use of a viscosity term in the plasma picture. The Larmor gyration of ions brings them into different parts of the plasma and will tend to equalize the fluid velocity, i.e. the finite Larmor radii for the ions introduce a lower length scale in the system. Fluctuations smaller than

this characteristic length will be damped out, which is exactly what a viscosity term is supposed to do.

Taking again the curl of equation (14), using the zero Larmor radii approximation to determine the plasma velocities will transform the problem into following the time evolution of the charge density ρ:

$$\frac{\partial \rho}{\partial t} + \mathbf{v} \cdot \nabla \rho = \nu \nabla^2 \rho \,, \tag{18}$$

$$\mathbf{v} = \frac{\mathbf{E} \times \mathbf{B}_o}{B^2} = -\frac{\nabla \phi \times \mathbf{B}_o}{B_o^2} \,; \tag{19}$$

$$\nabla^2 \phi = -\frac{\rho}{\epsilon_o} \,, \tag{20}$$

with ϕ being the electrostatic potential and ϵ the electric permittivity. The body force $\mathbf{f}$ has not been incorporated into the plasma picture. Normally this force will include the electromagnetic forces working on the plasma, but in the Q-machine experiments these forces are not present. The Lorentz force is zero for this setup as the velocity is given by the $\mathbf{E} \times \mathbf{B}$ drift velocity:

$$\begin{aligned} \mathbf{f}_L &= q(\mathbf{E} + \mathbf{v} \times \mathbf{B}_o) \\ &= q\left[\mathbf{E} + \frac{\mathbf{E} \times \mathbf{B}_o}{B_o^2} \times \mathbf{B}_o\right] = 0 \,. \end{aligned}$$

We are pumping energy into the flow, maintaining a constant shear around the plasma column due to a potential drop at the edge of the plasma column. The source of this energy is the hot plate which causes the potential drop. The hot plate is not a part of the flow and this feature therefore cannot be considered as a force in the usual sense.

The equations for neutral fluid and for the plasma fluid are actually identical. The electrostatic potential here takes the role of the stream function and the charge distribution that of the vorticity. The two constants, the magnetic field B_o and the electric permittivity ϵ_o in eqs. (19) and (20), can easily be transformed out of the system. In the rest of this chapter they will be set to be equal to 1. The sign difference in the definition of the velocity can be handled by letting the magnetic field point in the $-\mathbf{e}_z$ direction. This will transform eqs. (18) - (20) into the Navier-Stokes equation for neutral fluids given by eqs. (15) - (17).

In the next sections the different algorithms needed to solve the Navier-Stokes equations in an annulus geometry will be presented. It is here done by a spectral method where the solution is expanded into orthonormal basis functions. We will not present any feature about actually solving these algorithms computationally, i.e. we have assumed that the reader has basic knowledge about spectral methods (see, e.g., Gottlieb (1977) or Fox (1973)).

3.2 Numerical Scheme

Equations (18) - (20) are to be solved in a region which is similar to the setup of the Q-machine experiments. For this purpose a computer code has been developed at Risø which solves the problem in an annulus geometry, see Fig. 19. Here the inner radius denotes the plasma column and the outer radius denotes the confining steel vessel. In the first development of the code the viscosity term was not included (Huld (1990b), Coutsias *et al.* (1989)), and the code became unstable due to high frequency fluctuations at the boundaries. Several attempts to remove these

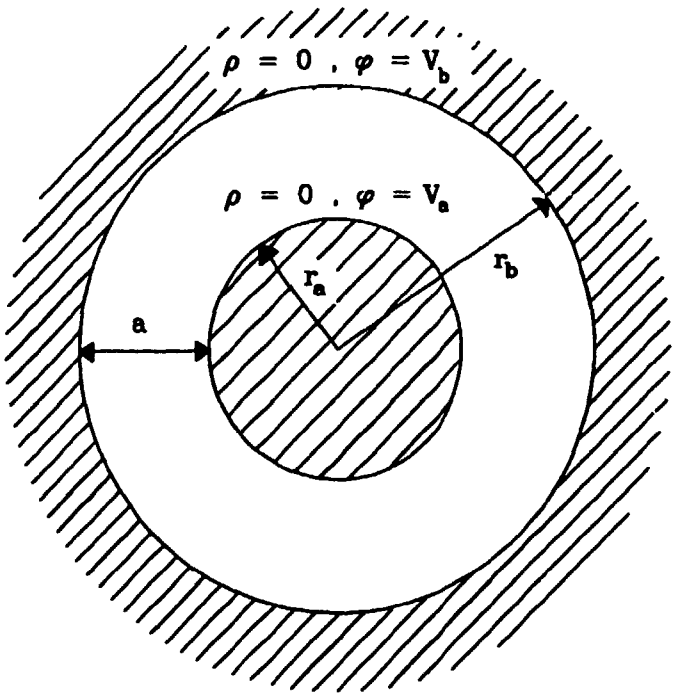

Figure 19. Geometry of the system.

fluctuations have been performed, e.g. "conditional smoothing in the configuration space" (Coutsias *et al.* (1989)), but have not been successful.

In the geometry of Fig. 19 a cylindrical coordinate system is an obvious choice. Using this coordinate system and substituting eq. (19) into eq. (18) yield:

$$r^2\frac{\partial\rho}{\partial t} - r(\frac{\partial\phi}{\partial\theta}\frac{\partial\rho}{\partial r} - \frac{\partial\phi}{\partial r}\frac{\partial\rho}{\partial\theta}) = \nu(r^2\frac{\partial^2\rho}{\partial r^2} + r\frac{\partial\rho}{\partial r} + \frac{\partial^2\rho}{\partial\theta^2}), \tag{21}$$

$$r^2\frac{\partial^2\phi}{\partial r^2} + r\frac{\partial\phi}{\partial r} + \frac{\partial^2\phi}{\partial\theta^2} = -r^2\rho, \tag{22}$$

where $r \in [r_a, r_b]$ is the radial and $\theta \in [-\pi, \pi[$ the azimuthal coordinates, and the two equations have here been multiplied by r^2. On the two boundaries the potential is defined to be constant in time around the annulus though not necessarily equal. This will result in a kind of free-slip boundary conditions, $\mathbf{v}(r = r_a, \theta)\cdot\mathbf{n} = \mathbf{v}(r = r_b, \theta)\cdot\mathbf{n} = 0$, where $\mathbf{n}$ is an outgoing normal to the boundary. There will be no transport of charge across the boundaries but we permit a plasma current on the wall in the azimuthal direction. As the system of equations, when expressed by the electrostatic potential ϕ, is a fourth-order differential equation, we need two more boundary conditions. They are obtained by requiring that the charge on the two boundaries is zero at all times. Comparing these boundary conditions with the physics of the Q-machine experiments, we see that we approximate the plasma column with a (free-slip) wall. This is actually not the case in the experiments. There is of course an effect from the plasma column, but it is not a solid wall. One can observe fluctuations inside the plasma column, even though they are small, and plasma is transported out of the plasma column due to these fluctuations. But in these simulations we are interested in seeing the formation of coherent structures evolving from small-scale fluctuations in an annulus geometry, and not

in an exact simulation of the experiment.

To follow the time evolution of ρ one can, for example, use a finite different or finite element method, but for a turbulent flow these schemes are found to be too inaccurate, see Coutsias *et al.* (1989). The second term on the left hand-side of eq. (21) is a highly nonlinear term which, in most cases, makes the solution turbulent in time. Instead the solution ρ and ϕ will be expanded into a finite number of orthonormal basis functions for each of the two coordinates r and θ:

$$\rho(r,\theta) = \sum_n \sum_m \rho_{mn} F_n(r) G_m(\theta). \tag{23}$$

$$\phi(r,\theta) = \sum_n \sum_m \phi_{mn} F_n(r) G_m(\theta). \tag{24}$$

For the azimuthal direction the expansion should of course be cyclical, and a simple orthonormal basis function with this property is the Fourier expansion:

$$F(\theta) = \sum_{n=-\infty}^{\infty} a_n \exp(in\theta) \ , \ \theta \in [-\pi, \pi[\, , \tag{25}$$

where

$$a_n = \frac{1}{2\pi} \int_{-\pi}^{\pi} F(\theta) \exp(-in\theta) d\theta. \tag{26}$$

This expansion involves infinitely many (complex) coefficients of a_n, which makes it impossible to use in numerical investigations as computers can only handle finite numbers. A truncation of the total number of modes is therefore necessary. Using the spectral method (collocation method, see Gottlieb (1977)) where we only use N terms in the expansion we get an approximation of the form:

$$F(\theta) \cong F_N(\theta) = \sum_{n=-N/2}^{N/2-1} \hat{a}_n \exp(in\theta) \, . \tag{27}$$

The values of $\hat{a}_n$ can then be determined by solving N linear equations

$$F_N(\theta_i) = F(\theta_i) \tag{28}$$

$$\theta_i = \frac{2\pi i}{N} \ , \ i \in (-N/2, \cdots, -1, 0, 1, \cdots, N/2-1) \, .$$

As the points, θ_i, are given in equividistant points, a Fast Fourier Transformation (FFT) can therefore with success be employed in the scheme, see Press *et al.* (1986). Due to aliasing errors when performing the FFT some of the highest modes must be dropped, for the present algoritm only 2/3 of the modes in each direction have been used, see Fox *et al* (1973). The Fourier functions are "simple" functions when differentiating a mode n with respect to variable θ; the result will be the same mode multiplied by a constant. Performing the θ-derivative in eqs. (18) - (20) introduces no major problem. Since both $\rho(r,\theta)$ and $\phi(r,\theta)$ are real functions, a real FFT is employed in the numerical code. This expansion explicitly uses cosine and sine modes and requires only N real coefficients to be stored as opposed to the N complex, or $2N$ real, coefficients implied by eq. (27). However, in order to keep the discussion simple, the exponential Fourier notation is used.

For the radial direction the solution is expanded in Chebyshev polynomials of the first kind; in the following they will simply be called Chebyshev polynomials. Making again the restriction of only taking a finite number of modes, the radial

expansion will take the form:

$$G(x) = \sum_{m=0}^{M} b_m T_m(x) \tag{29}$$

$$= \sum_{m=0}^{M} b_m \cos(m \arccos x) \ , \ x \in [-1,1] \ . \tag{30}$$

The first four Chebyshev polynomials can alternatively be written as

$$T_0(x) = 1 \quad , \quad T_1(x) = x$$

$$T_2(x) = 2x^2 - 1 \quad , \quad T_3(x) = 4x^3 - 3x \ ,$$

and the higher order polynomials are easily determined from the recursion formula

$$T_{m+1}(x) = 2xT_m(x) - T_{m-1}(x) \ . \tag{31}$$

The Chebyshev polynomials are only defined in the closed interval $[-1,1]$ and, therefore, the variable r has to been transformed. One way of making such a transformation is by defining a new variable: $x = r - a$, with $a = (r_b + r_a)/2$ being the aspect radius, see Fig. 19, and by letting the radius of the annulus be $r_b - r_a = 2$.

As the Fourier expansion was given in equividistant points, an FFT could be used to find the expansion, but there is no method which will directly expand a function given at discrete points in Chebyshev polynomials. However, when choosing to evaluate the solution in the radial grid points:

$$x_i = \cos(\frac{\pi i}{M}) \ , \ i \in [0, M] \ , \tag{32}$$

the m'th Chebyshev polynomial will take the form

$$T_m(x_i) = \cos(\frac{m\pi i}{M}). \tag{33}$$

The Chebyshev polynomials are now expressed by a cosine function and so the Chebyshev expansion can be performed by a cosine transformation which is closely related to an FFT (see Press *et al.* (1986)).

Unlike the Fourier expansion the Chebyshev polynomials are not "simple" functions. A differentiation of a Chebyshev polynomial m will result in contributions from many other Chebyshev polynomials. The problems in the next sections will require the knowledge of these two basic recursion formulas for the Chebyshev polynomials:

$$xT_m(x) = \begin{cases} T_1(x) & \text{for } m = 0 \\ \frac{1}{2}T_{m-1}(x) + \frac{1}{2}T_{m+1}(x) & \text{for } m \neq 0 \end{cases} \tag{34}$$

$$\frac{dT_m(x)}{dx} = \begin{cases} 0 & \text{for } m = 0 \\ T_0(x) & \text{for } m = 1 \\ 4T_1(x) & \text{for } m = 2 \\ 2m\sum_{k=1}^{m/2-1} T_{2k}(x) & \text{for } m \text{ even} \\ 2m\sum_{k=1}^{(m-1)/2} T_{2k+1}(x) + mT_0(x) & \text{for } m \text{ odd} \end{cases} \tag{35}$$

The procedure is always the same when applyin these recursion formulas to a given problem, viz. one has to rearrange the different terms into the same Chebyshev polynomials, $T_m(x)$. Mostly this is quite a puzzle, but it involves no expensive algebra. A more detailed list of formulas relating Chebyshev expansions to various linear operators is given in the appendix of Gottlieb (1977).

The total expansion of the charge ρ and the potential ϕ will then have the form:

$$\rho(x,\theta) = \sum_{n=-N/2}^{N/2-1} \sum_{m=0}^{M} \rho_{mn} T_m(x) \exp(in\theta) , \tag{35}$$

$$\phi(x,\theta) = \sum_{n=-N/2}^{N/2-1} \sum_{m=0}^{M} \phi_{mn} T_m(x) \exp(in\theta) , \tag{37}$$

where $\rho_{mn} = b_m \hat{a}_n$. As mentioned above, both the charge and the potential are to be constant on the boundaries for all values of θ. This will put a constraint on both functions. For the Chebyshev polynomials at the edge of the interval we have: $T_m(\pm 1) = (\pm 1)^m$, and applying this result to eqs. (36) and (37) the boundary conditions will take the form:

$$\begin{aligned} \sum_{m=0}^{M} \rho_{nm} &= 0 \\ \sum_{m=0}^{M} (-1)^m \rho_{nm} &= 0 , \end{aligned} \tag{38}$$

$$\begin{aligned} \sum_{m=0}^{M} \phi_{nm} &= \begin{cases} V_b & n = 0 \\ 0 & n \neq 0 \end{cases} \\ \sum_{m=0}^{M} (-1)^m \phi_{nm} &= \begin{cases} V_a & n = 0 \\ 0 & n \neq 0 \end{cases} . \end{aligned} \tag{39}$$

These boundary conditions will be employed when the Poisson equation is to be solved, see the next section, and for the Helmholtz equation when performing the time stepping.

3.3 The Poisson Solver

In solving the Navier-Stokes equations, one needs to calculate the potential at each time step in order to find the velocity given by eq. (19). For a given charge distribution we then have to solve the Poisson equation. As we use Chebyshev polynomials in the radial direction this problem is not at all straightforward. Substituting the expansion given in eq. (36) into eq. (22), using the new variable x, the Poisson equation takes this complicated form:

$$\begin{aligned} \sum_{n=-N/2}^{N/2-1} \Bigg[(x+a)^2 \frac{d^2}{dx^2} \sum_{m=0}^{M} \phi_{mn} T_m(x) &+ (x+a) \frac{d}{dx} \sum_{m=0}^{M} \phi_{mn} T_m(x) \\ &- n^2 \sum_{m=0}^{M} \phi_{mn} T_m(x) \Bigg] \exp(in\theta) \\ = - \sum_{n=-N/2}^{N/2-1} &\Big[(x+a)^2 \sum_{m=0}^{M} \rho_{mn} T_m(x) \Big] \exp(in\theta) \\ = \sum_{n=-N/2}^{N/2-1} &\Big[\sum_{m=0}^{M} \rho^*_{mn} T_m(x) \Big] \exp(in\theta) , \end{aligned} \tag{40}$$

where $\rho^*_{mn} = -(x+a)^2 \rho_{mn}$ has been introduced to simplify the problem. This function can readily be found using the recursion formula given in eq. (34) twice:

$$
\begin{aligned}
r^2\rho &= (x+a)^2 \sum_{n=-N/2}^{N/2-1} \sum_{m=0}^{M} \rho_{mn} T_m(x) \exp(in\theta) \\
&= \sum_{n=-N/2}^{N/2-1} \Big[(\frac{1}{2} + a^2)\rho_{0n} + a\rho_{1n} + \frac{1}{4}\rho_{2n} \\
&\quad + \big(2a\rho_{0n} + (\frac{3}{4} + a^2)\rho_{1n} + a\rho_{2n} + \frac{1}{4}\rho_{3n}\big) T_1(x) \\
&\quad + \big(\frac{1}{2}\rho_{0n} + a\rho_{1n} + (\frac{1}{2} + a^2)\rho_{2n} + a\rho_{3n} + \frac{1}{4}\rho_{4n}\big) T_2(x) \\
&\quad + \sum_{m=3}^{M-2} \big(\frac{1}{4}\rho_{m-2,n} + a\rho_{m-1,n} + (\frac{1}{2} + a^2)\rho_{mn} \\
&\quad + a\rho_{m+1,n} + \frac{1}{4}\rho_{m+2,n}\big) T_m(x) \Big] \exp(in\theta) \qquad (41)
\end{aligned}
$$

Using the recursion formulas given be eqs. (34) and (35) extensively, we can simplify eq. (40); the procedure is algebraically very simple, but it is very time consuming. For each Fourier mode, n, we have to solve the following equation:

$$
\sum_{m=0}^{M} \rho^*_{mn} = \sum_{m=0}^{M} \Big[(m^2 - n^2)\phi_{mn} + B_m \sum_{p=m}^{M} C_p\, p(p^2 - m^2)\phi_{pn} \Big] , \qquad (42)
$$

where

$$
B_m = \begin{cases} \frac{1}{2} & \text{for } m = 0 \\ 1 & \text{for } m \neq 0 \end{cases} , \quad C_p = \begin{cases} a^2 + 1 & \text{for } p \text{ even} \\ 2a & \text{for } p \text{ odd} \end{cases} . \qquad (43)
$$

Equation (42) denote a matrix problem of the form: $\underline{\rho}^*_n = \underline{\underline{A}}_n \cdot \underline{\phi}_n$, where $\underline{\underline{A}}_n$ is a triangular matrix as the m'th row of the matrix only has nonzero elements for the variables: $\phi_m \cdots \phi_M$. We can of course solve this matrix problem directly using, e.g., a backsubstitution method, but the number of operations necessary is in the order of M^2. This is unacceptable as we want to solve the Poisson equation for each Fourier mode n several times. Fortunately, we can simplify the matrix analytically. Denoting the m'th row of $\underline{\underline{A}}_n$ as $E_n(m)$ we make the following row multiplications:

$$
E^*_n(m) = \gamma(m)E_n(m) + \alpha(m)E_n(m+2) + \beta(m)E_n(m+4) , \qquad (44)
$$

where α, β and γ are functions depending only on the row number m. Having substituted this transformation into eq. (42) the m'th row will then have the form:

$$\begin{aligned}
\gamma(m^2-n^2)\phi_{mn} &+ 2\alpha B_m\gamma(m+1)(2m+1)\phi_{m+1,n} + \\
\left[\gamma B_m(\alpha^2+1)(m+2)(4m+4)\right. &+ \left.\alpha((m+2)^2-n^2)\right]\phi_{m+2,n} + \\
\left[2\alpha\gamma B_m(m+3)(6m+9)\right. &+ \left.2a\alpha(m+3)(2m+5)^2\right]\phi_{m+3,n} + \\
\left[\gamma B_m(\alpha^2+1)(m+4)(8m+16)\right. &+ \alpha(\alpha^2+1)(m+4)(4m+12) \\
&+ \left.\beta((m+4)^2-n^2)\right]\phi_{m+4,n} + \\
\sum_{p=m+5}^{M} C_p\Big[\gamma B_m\, p(p^2-m^2) &+ \alpha p(p^2-(m+2)^2)+\beta p(p^2-(m+4)^2)\Big]\phi_{pn} \\
&= \gamma\rho^*_{mn} + \alpha\rho^*_{m+2,n} + \beta\rho^*_{m+4,n}\,. \qquad (45)
\end{aligned}$$

The scoop is now to choose $\gamma(m)$, $\alpha(m)$ and $\beta(m)$ in such a way that the summation in eq. (45) vanishes. Please note that we have to treat the last five rows separately as we are working in a truncated system. By letting:

$$\alpha(m) = \begin{cases} -\frac{B_m 2(m+2)\gamma(m)}{m+3} & \text{for } m \in [0; M-5] \\ -\frac{(10M-25)\gamma(M-4)}{6M-9} & \text{for } m = M-4 \\ 0 & \text{for } m \in [M-3, M] \end{cases} \qquad (46)$$

and

$$\beta(m) = \begin{cases} \frac{B_m(m+1)\gamma(m)}{m+3} & \text{for } m \in [0; M-5] \\ 0 & \text{for } m \in [M-4; M] \end{cases} \qquad (47)$$

we are left with only nonzero elements at the positions $m, \cdots, m+4$ of the m'th row in matrix $\underline{\underline{A}}$. This has transformed the triangle matrix into a triangularised, pentadiagonal matrix which is much faster to calculate than the original matrix problem. The function $\gamma(m)$ can be chosen freely in eq. (45). It is introduced for stability reasons so that each element of $\underline{\underline{A}}$ is numerically of the same order. As the elements in eq. (45) scale as m^2, we have chosen $\gamma(m) = 1/m^2$.

We must evidently solve the Poisson equation using the boundary conditions for ϕ, i.e. using eq. (39), which introduces two new equations in the system. This leaves us with $M+3$ equations with only $M+1$ unknown variables. The problem is hereby overdetermined. We therefore remove the last two rows of the matrix. This will of course change the value of the two variables, ϕ_{M-1} and ϕ_M but since they contain information about the truncation, the error we make is not grave. Anyway, the energy of those modes is very small and they will not have any (serious) influence on the time evolution of the flow.

3.4 The Convolution Sum

The electrostatic potential is found by solving the Poisson equation and the nonlinear term from eq. (21) can then be calculated, i.e.

$$-\left(\frac{\partial\phi}{\partial\theta}r\frac{\partial\rho}{\partial r} - r\frac{\partial\phi}{\partial r}\frac{\partial r}{\partial\theta}\right)\,.$$

We are here faced with a problem as we have to calculate the two derivatives $\partial/\partial\theta$ and $r\partial/\partial r$ for both ρ and ϕ. Since both functions are expanded into the

same basis functions, their derivatives will have the same form. Therefore only the derivatives of ρ will be presented.

For the θ-derivative life is very simple; one can directly perform the azimuthal derivative of the expansion given in eq. (37) :

$$\begin{aligned}\frac{\partial \rho}{\partial \theta} &= \frac{\partial}{\partial \theta}\Big[\sum_{m=0}^{M}\sum_{n=-N/2}^{N/2-1}\rho_{mn}T_m(x)\exp(in\theta)\Big] \\ &= \sum_{m=0}^{M}\sum_{n=-N/2}^{N/2-1} in\rho_{mn}T_m(x)\exp(in\theta) \ . \end{aligned} \tag{48}$$

It is just a constant multiplied by the same Fourier mode and no rearranging of the terms is therefore needed.

For the r-derivative things are more complicated. Extensive use of the recursion formulas given in eqs. (34) and (35) is needed to get:

$$\begin{aligned} r\frac{\partial \rho}{\partial r} &= \sum_{n=-N/2}^{N/2-1}\sum_{m=0}^{M} d_{mn}T_m(x)\exp(in\theta) \\ &= \sum_{n=-N/2}^{N/2-1}\Big[(x+a)\sum_{m=0}^{M}\rho_{mn}\frac{dT_m(x)}{dx}\Big]\exp(in\theta) \\ &= \sum_{n=-N/2}^{N/2-1}\Big[\sum_{p=0}^{M} pD_p\rho_{pn} + \sum_{m=1}^{M}\Big[m\rho_m + 2\sum_{p=m+1}^{M} D_p p\rho_p\Big]T_m(x)\Big]\exp(in\theta) \ , \end{aligned} \tag{49}$$

where

$$D_p = \begin{cases} 1 & \text{for } p+m \text{ even} \\ a & \text{for } p+m \text{ odd} \end{cases} \ , \tag{50}$$

and d_{mn} denotes the coefficients of the resulting expansion of the r-derivative. To solve this equation we need to make in the order of $M^2 \cdot N$ operations, which is too time consuming. Fortunately, there is a way around this. First we calculate $d_{M,n}$ and $d_{M-1,n}$ for each Fourier mode n, then we determine the rest of the coefficients by rewriting eq. (50) into a recursion formula:

$$\begin{aligned} d_{mn} &= d_{m+2,n} + m\rho_{mn} + 2a(m+1)\rho_{m+1,n} + (m+2)\rho_{m+2,n} \\ d_{0n} &= \frac{1}{2}d_{2,n} + a\rho_{1,n} + \rho_{2,n} \ . \end{aligned} \tag{51}$$

Note that the zero Chebyshev polynomial has to be treated differently and that we get the same recursion formula for m even as for m odd. We can now calculate the r-derivative using only in the order of $M \cdot N$ operations.

We have transformed the four derivatives in the nonlinear term into four expansions and they have to be multiplied. We can perform this in the transformed space but, unfortunately, products in real space become convolution integrals in the transformed space, which is too time consuming to perform. Instead, the four terms are transformed into real space using the FFT routine. Here the products are made using the values in the grid points and the results are then transformed back into the transformed space. The FFT routine uses in the order of $MN(\log_2 M)(\log_2 N)$ operations and the calculations are (and should be) the most time consuming in the computer program. After calculating these products, we have the nonlinear term given by a new expansion:

$$G(\rho,\theta,t) = -(\frac{\partial\phi}{\partial\theta}r\frac{\partial\rho}{\partial r} - r\frac{\partial\phi}{\partial r}\frac{\partial r}{\partial\theta}) = \sum_{n=-N/2}^{N/2-1}\sum_{m=0}^{M} g_m T_m(x)\exp(in\theta) \ , \quad (52)$$

which shall be used when performing the time stepping in the next section.

3.5 The Time Evolution

With the results obtained in the previous sections, we are now ready to solve the Navier-Stokes equations completely. Introducing the convolution sum, denoted by the function $G(\rho,\phi,t)$, our equation has the form:

$$r^2\frac{\partial\rho}{\partial t} = G(\rho,\phi,t) + \nu r^2\nabla^2\rho \ , \quad (53)$$

which is to be discretized in time. This is done by finding the solution ρ at the discrete time points: $t_o, t_1 \cdots, t_i, t_{i+1} \cdots$, i.e. when we are given the solution ρ^i at the time t_i, use eq. (53) to generate the solution ρ^{i+1} at the time t_{i+1}. Actually, only single step algorithms use the solution at time t_i, while multi-step algorithms also use information about the solution at previous times, i.e. for $t_{i-1}\cdots$. For simplicity the procedure will be described using the simplest time discretization scheme, the Euler method, before proceeding to the more advanced ones. Applying the Euler method to eq. (53) yields:

$$r^2\frac{\rho^{i+1}-\rho^i}{\Delta t} = G(\rho^i,\phi^i,t_i) + \nu r^2\nabla^2\rho^{i+1} \ , \quad (54)$$

where Δt is a constant time spacing between the calculated solutions. The viscosity term is here evaluated at time t_{i+1} for stability reasons; if it is evaluated at t_i, it has been found that the scheme will quickly become unstable. Rearranging the terms in eq. (54) yields:

$$(r^2 - \nu\Delta t r^2\nabla^2)\rho^{i+1} = r^2\rho^i + \Delta t G(\rho,\phi,t_i) \ . \quad (55)$$

This equation is known as the Helmholtz equation. The right-hand side of the equation can be expressed in Fourier functions and Chebyshev polynomials using eqs. (41) and (52) and will be denoted $\underline{F}^i$ in the rest of the section. The operator on the left-hand side does process some problems but, fortunately, we have already developed the tools to handle them. The first term, $r^2\rho$, can be found from eq. (41) which, for a specific Fourier mode n, is a $(M+1)\times(M+1)$ matrix. The second term $r^2\nabla^2\rho$ is "just" our matrix from the Poisson solver, which has been derived in eq. (45). This matrix, one for each Fourier function n, has been transformed from a triangular matrix to a triangularised, pentadiagonal matrix by performing the row multiplications given in eq. (44). When combining the two matrixes one also has to perform the row multiplications on the $r^2\rho$ matrix. The Helmholtz equation has then been reduced to solve n matrix problems: $\underline{\underline{B}}_n\underline{\rho}_n^{i+1} = \underline{F}_n^{i+1}$, where the m'th row of the matrix, $\underline{\underline{B}}_n$, has the form:

$$\frac{\gamma}{4}\rho^{i+1}_{m-2,n} + a\gamma\rho^{i+1}_{m-1,n} + \Big[(\frac{1}{2}+a^2)\gamma + (m^2-n^2)\gamma\Big]\rho^{i+1}_{m,n} +$$
$$\Big[a\gamma + 2a(m+1)(2m+1)\gamma + a\alpha\Big]\rho^{i+1}_{m+1,n} +$$
$$\Big[a\gamma + a\alpha + (a^2+1)(m+2)(4m+4)\gamma + ((m+2)^2-n^2)\alpha\Big]\rho^{i+1}_{m+2,n} +$$
$$\Big[a\alpha + a\beta + 2a(m+3)(6m+9)\gamma + 2a(m+2)(2m+5)^2\alpha\Big]\rho^{i+1}_{m+3,n} +$$
$$\Big[\frac{\alpha}{4} + (\frac{1}{2}+a^2)\beta + (a^2+1)(m+4)(8m+16)\gamma +$$
$$(a^2+1)(m+4)(4m+12)\alpha + ((m+4)^2-n^2)\beta\Big]\rho^{i+1}_{m+4,n} +$$
$$a\beta\rho^{i+1}_{m+5,n} + \frac{\beta}{4}\rho^{i+1}_{m+6,n} = \gamma F^{i+1}_{m,n} + \alpha F^{i+1}_{m+2,n} + \gamma F^{i+1}_{m+4,n} \quad , \tag{56}$$

a complicated expression but easy to calculate on computers as the matrix $\underline{\underline{B}}_n$ is a triangularised, ninth-diagonal matrix. The functions, γ, α and β are only functions of the row number m. Note that the first three rows of $\underline{\underline{B}}_n$ look different due to the $r^2\rho$ term, see eq. (41). As was the case with the Poisson equation, also the Helmholtz equation is to be solved using the boundary conditions found in eq. (38); again we drop the last two rows of $\underline{\underline{B}}_n$ as they involve the variables $\rho_{M-1,n}$ and $\rho_{M,n}$ containing information about the truncation.

As already mentioned we are not using a single step Euler method for the time stepping. Such a scheme is too unstable to use in the time evolution of a turbulent flow. Instead, we have implemented a fully corrected third-order Adams-Bashford algorithm, see Gazdag (1976). This algorithm consists of a predictor step:

$$(r^2 - \nu\Delta t r^2\nabla^2)\tilde{\rho}^{i+1} = r^2\rho^i + \frac{\Delta t}{12}(23G^i - 16G^{i-1} + 5G^{i-2}) \quad , \tag{57}$$

where $\tilde{\rho}^{i+1}$ denotes the predicted charge distribution at t_{i+1} and G^i, G^{i-1} and G^{i-2} denotes the convolution sum for the time t_i, t_{i-1} and t_{i-2} respectively. $\tilde{\rho}^{i+1}$ is then used to find a predicted convolution sum $\tilde{G}^{i+1}$. Finally, we obtain the corrected charge distribution ρ^{i+1} through the formula:

$$(r^2 - \nu\Delta t r^2\nabla^2)\rho^{i+1} = r^2\rho^i + \frac{\Delta t}{12}(5\tilde{G}^{i+1} + 8G^i - G^{i-1}) \quad . \tag{58}$$

As the scheme is fully corrected, the convolution sum has to be calculated for the corrected charge distribution, i.e. G^{i+1}. When solving the Helmholtz equation (see eq. (55)), the method is the same; only the right-hand side of eq. (55) has been replaced with information about the solution at the previous time step.

When given an initial charge distribution ρ^o one needs to calculate the first two time steps using other methods than the method described above. The first time step is calculated by using a leapfrog scheme and the second by a fully corrected Adam-Bashford algorithm, see Gazdag (1976).

To summarize what has been presented up to now, let me give a short description of the scheme.

(I) When given a charge distribution ρ^i expressed in Fourier mode and Chebyshev polynomials, solve the Poisson equation to find the corresponding expansion of the potential, using the boundary conditions $\phi(r = r_a, \theta) = V_a$ and $\phi(r = r_b, \theta) = V_b$.

(II) Find the azimuthal and radial derivatives for these two expansions.

(III) Find the convolution sum by transforming the derivatives into configuration space, perform the multiplications there using the values in the grid points, and

transform the result back into the transformed space.
(IV) Perform the time stepping to obtain ρ^{i+1} and hereby solve the Helmholtz equation as the viscosity term is given implicitly and use the boundary condition for the charge distribution: $\rho(r = r_a, \theta) = 0$ and $\rho(r = r_b, \theta) = 0$.
(V) Go to (I).

3.6 Energy and Enstrophy Evolution

As we are working with a finite number of modes, we want to have some diagnostics on how well the simulation of Navier-Stokes equations behaves compared with the real solution. In the inviscid and force-free case the Navier-Stokes equations, given by either eq. (14) or eq. (18), guarantee that there exists an infinite family of conserved integrals. Here we will concentrate on the following two:
The total kinetic energy:

$$E = \frac{1}{2}\int_D \mathbf{u}\cdot\mathbf{u}\,ds = \frac{1}{2}\int_D u_r^2 + u_\theta^2\,ds\,, \tag{59}$$

and the total enstrophy:

$$\Omega = \int_D \rho^2\,ds\,. \tag{60}$$

By inserting the time derivatives of E and Ω into eqs. (14) and (18), respectively, one can easily demonstrate that these integrals are time constants. The effect of the boundaries in our geometry does not change either of the integrals as we are working with free-slip boundaries. If we had implemented no-slip boundary condition there could be an enstrophy input to the system, see Coutsias and Lynov (1991), but we want to use boundary conditions which will result in minimum disturbance of the flow. The effect of the viscosity term will take energy and enstrophy out of the flow, and we will thus expect these two "invariants" to decrease during the time evolution.

To calculate the integrals we note that all three of them have the same form. When given a variable y ($y = u_r, u_\theta$ or ρ) by the coefficients to the Chebyshev and Fourier expansions we want to calculate the integral: $\int_D y^2 ds$. To find the expansion of y^2 we transform the variable y into the configuration space where we calculate y^2 using the values given in the grid points. The results are then transformed back into the transformed space and we thus have y^2 given by the coefficients to the Chebyshev and the Fourier expansion; they will be denoted y^*. The integral is then reduced to:

$$\int_D y^2 ds = \int_{-1}^{1}\int_0^{2\pi} y^*_{mn} T_m(x)\exp(in\theta)\,(x+a)\,dx\,d\theta\,. \tag{61}$$

Only for $n = 0$ will the integral in eq. (61) result in nonzero contributions and with some help from eq. (34) we find:

$$\int_D y^2 ds = 4\pi a y^*_{00} - \sum_{k=1}^{M/2}\frac{4\pi a}{4k^2-1}y^*_{2k,0} + \sum_{k=1}^{M/2}\frac{4\pi}{4k^2-4k-3}y^*_{2k-1,0}\,. \tag{62}$$

As the calculation of the total energy and enstrophy requires the use of the FFT subroutine (six times), we are not interested in calculating these quantities for every time step. Anyway, they will not change much between each time step and they are consequently only evaluated when needed. The evolution of these quantities will thus offer information about the behavior of the code, but to find exactly

how much the simulated solution has diverged from the exact one, we need to relate them to theoretical expressions. We can find an analytical relation between the decay rate of the energy and the enstrophy. The temporal evolution of the total energy is described by (see Coutsias and Lynov (1991)):

$$\frac{dE}{dt} = \int_D \mathbf{u} \cdot \frac{\partial \mathbf{u}}{\partial t}\, ds \ . \tag{63}$$

Using the vector relation:

$$\begin{aligned} \nabla \times (\nabla \times \mathbf{u}) &\equiv \nabla(\nabla \cdot \mathbf{u}) - \nabla^2 \mathbf{u} \\ &= -\nabla^2 \mathbf{u} \\ &= \nabla \rho \mathbf{e}_z \end{aligned}$$

in eq. (14), and inserting this in eq. (63) yields:

$$\frac{dE}{dt} = \int_D \mathbf{u} \cdot [\mathbf{u} \times \rho \mathbf{e}_z - \nabla(p + \frac{1}{2}\mathbf{u}^2) - \nu \nabla \rho \mathbf{e}_z] ds \ . \tag{64}$$

Each of the three terms on the right-hand side of eq. (64) will be evaluated separately.

The first term

$$\int_D \mathbf{u} \cdot [\mathbf{u} \times \rho \mathbf{e}_z]\, ds \equiv 0$$

since $\mathbf{u} \times \mathbf{e}_z \perp \mathbf{u}$.

Introducing $\Phi \equiv p + \frac{1}{2}\mathbf{u}^2$ the second term yields:

$$\begin{aligned} \int_D \mathbf{u} \cdot \nabla \Phi \, ds &= \int_D (\nabla \cdot (\mathbf{u}\Phi) - \Phi \nabla \cdot \mathbf{u})\, ds \\ &= \int_{\partial D} \mathbf{u}\Phi \cdot \mathbf{n}\, dl = 0 \, , \end{aligned}$$

where we have used Stokes theorem, the flow is incompressible, and $\mathbf{u}$ is perpendicular to the outgoing normal $\mathbf{n}$ on ∂D as we have employed free-slip boundary conditions.

Again using Stokes theorem the last term on the right-hand side of eq. (64) can be written as:

$$\begin{aligned} -\nu \int_D \mathbf{u} \cdot (\nabla \times \rho \mathbf{e}_z) ds &= \nu \int_D [\nabla \cdot (\mathbf{u} \times \rho \mathbf{e}_z) - \rho \mathbf{e}_z \cdot (\nabla \times \mathbf{u})]\, ds \\ &= \nu \int_{\partial D} (\mathbf{u} \times \rho \mathbf{e}_z) \cdot \mathbf{n}\, ds - \nu \Omega \\ &= -\nu \Omega \, , \end{aligned} \tag{65}$$

as $\rho = 0$ on the boundaries. We have thus gained a simple relation between the two quantities:

$$\frac{dE}{dt} = -\nu \Omega(t) \, . \tag{66}$$

As the enstrophy, Ω, is always a positive quantity, the total energy E must decay monotonously. By comparing the calculated time evolution of the energy with the predicted energy decay obtained by a simple Euler integration of eq. (66), we thus have a measure of the accuracy of the simulation. It is also possible to obtain an expression for the decay of the enstrophy,

$$\frac{d\Omega}{dt} = 2\nu \int_D \omega(t) \nabla^2 \omega \, ds \, , \tag{67}$$

but at present it has not been incorporated into the computer code.

3.7 Numerical Results

The algorithms for simulating the Navier-Stokes equations have been transformed into a FORTRAN computer code and implemented on Risø's Apollo DN10000 "minisupercomputer". For testing of the computer program this computer is sufficient, but it is necessary to use a real supercomputer to get the spatial resolution sufficiently high. One should note that the code has only recently been completed and several tests must be performed. The decay rate of the enstrophy (see eq. (67)), will be implemented in the near future. Also the accuracy of the code must be improved. In this section two different kinds of simulations will be presented. First a potential profile similar to the profile found in the Q-machine is initialized. This profile is known to be unstable, see Chapter 2. In the second simulation a high azimuthal mode is initialized in order to examine the inverse cascade, where energy is transported from small wavelength to large wavelength.

Due to the viscosity term the system will tend towards a stable situation where there is no charge present in the annulus. In this case there will be some energy in the system as we have forced a potential difference between the two boundaries. To find this DC-potential profile we note that there cannot be any azimuthal dependence, and the profile can be found by solving the Poisson equation for $\rho = 0$:

$$\begin{aligned} \nabla^2 \phi_{dc} &= 0 \Rightarrow \\ \phi_{dc}(r) &= C_1 \ln r + C_2 , \end{aligned} \tag{68}$$

where the two integration constants can be found using the two boundary conditions, ϕ_a and ϕ_b, see Fig. 19. As we are free to choose the zero level of the potential, we can without any problems simplify the equations by letting $\phi_a \equiv 0$.

$$C_1 = \frac{\phi_b}{\ln r_b/r_a} , \; C_2 = -\frac{\phi_b \ln r_a}{\ln r_b/r_a} .$$

The DC potential profile will create an azimuthal velocity:

$$u_{\theta,dc} = \frac{C_1}{r} . \tag{69}$$

This velocity profile is stable in the sense that all initial conditions will tend towards it due to the viscosity. The energy associated with this profile is given by:

$$\begin{aligned} E_{dc} &= \int_{r_a}^{r_b} \int_0^{2\pi} u_{\theta,dc}^2 r dr d\theta \\ &= \frac{2\pi\phi_b^2}{\ln r_b/r_a} . \end{aligned}$$

The DC-potential profile is not the potential profile we find from the Q-machine experiments, otherwise this report would not have been written. The profile is actually far from being logarithmic as the potential drop occurs over a small spatial distance compared with the dimensions involved. To set up a situation which simulates such a potential profile, we have chosen:

$$\phi(r, \theta, t = 0) = -\frac{\phi_b}{2} \tanh(\frac{r - r_d}{\Delta}) - \frac{\phi_b}{2} , \tag{70}$$

where the parameter r_d makes it possible to choose the location of the potential drop, and Δ is the size of it. Note that there is no azimuthal dependence on the potential profile which is in agreement with the experiments where the profile is,

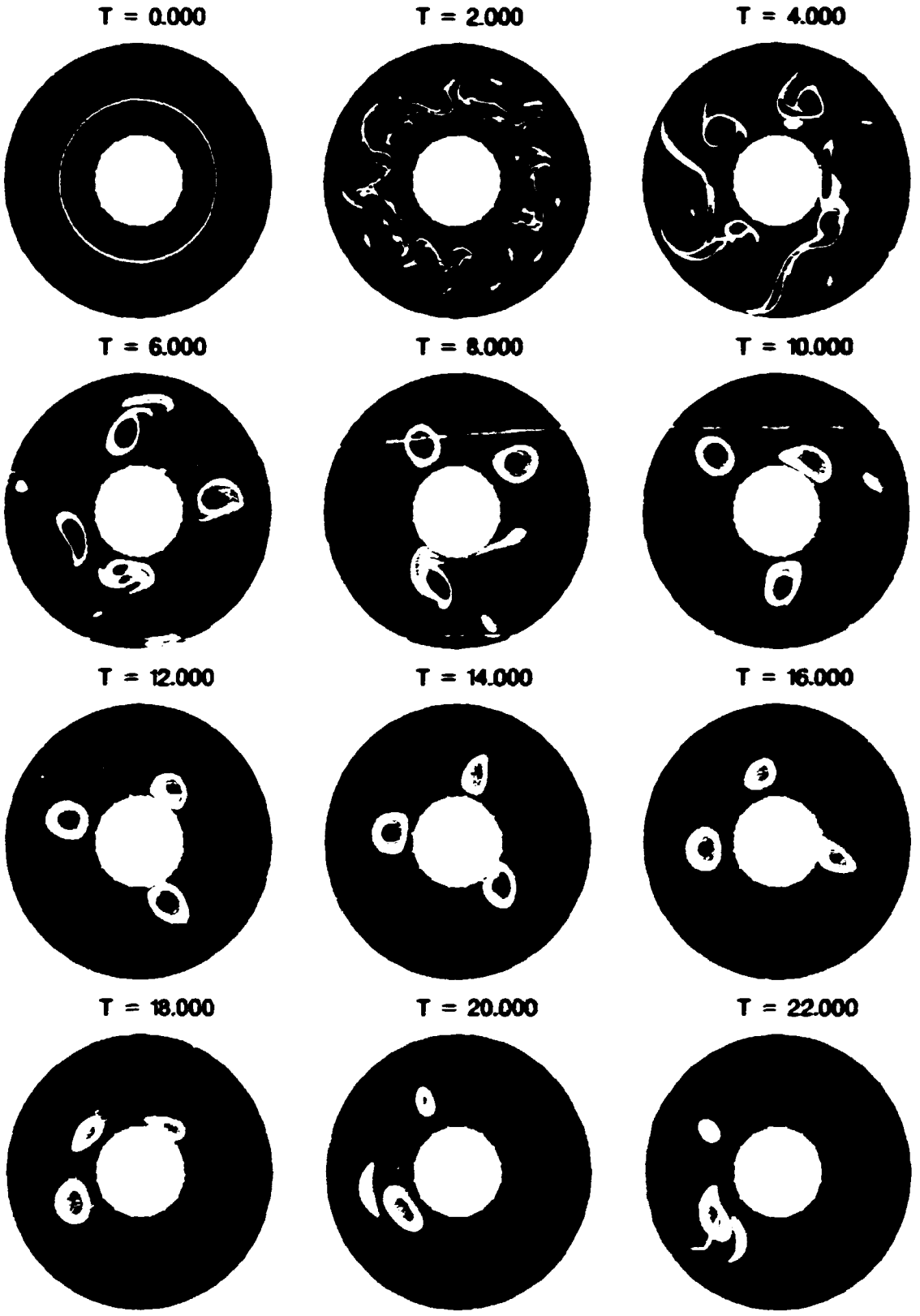

Figure 20. $\omega(r,\vartheta,t)$ for twelve different times using eq. (71) as initial condition. Here $N = 256$, $M = 64$, $\alpha = 2.0$, $\Delta t = 5 \cdot 10^{-3}$, $\omega_0 = 1$, $\Delta = 12$ and $\nu = 10^{-3}$. High values are red whereas low are values blue in the plot.

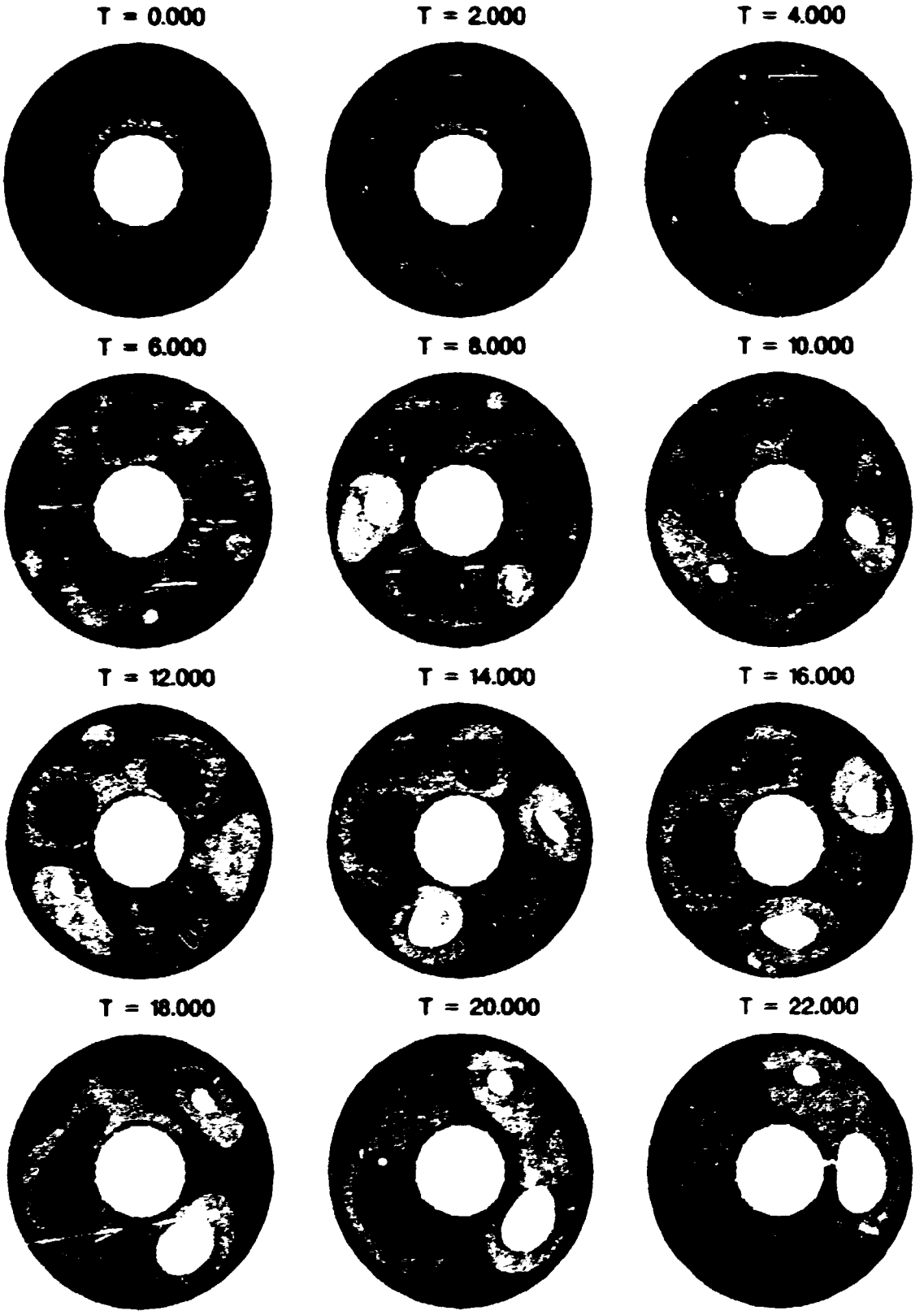

Figure 21 [illegible] for the same twelve times as in Fig.20. The DC potential variation has been removed from the solution.

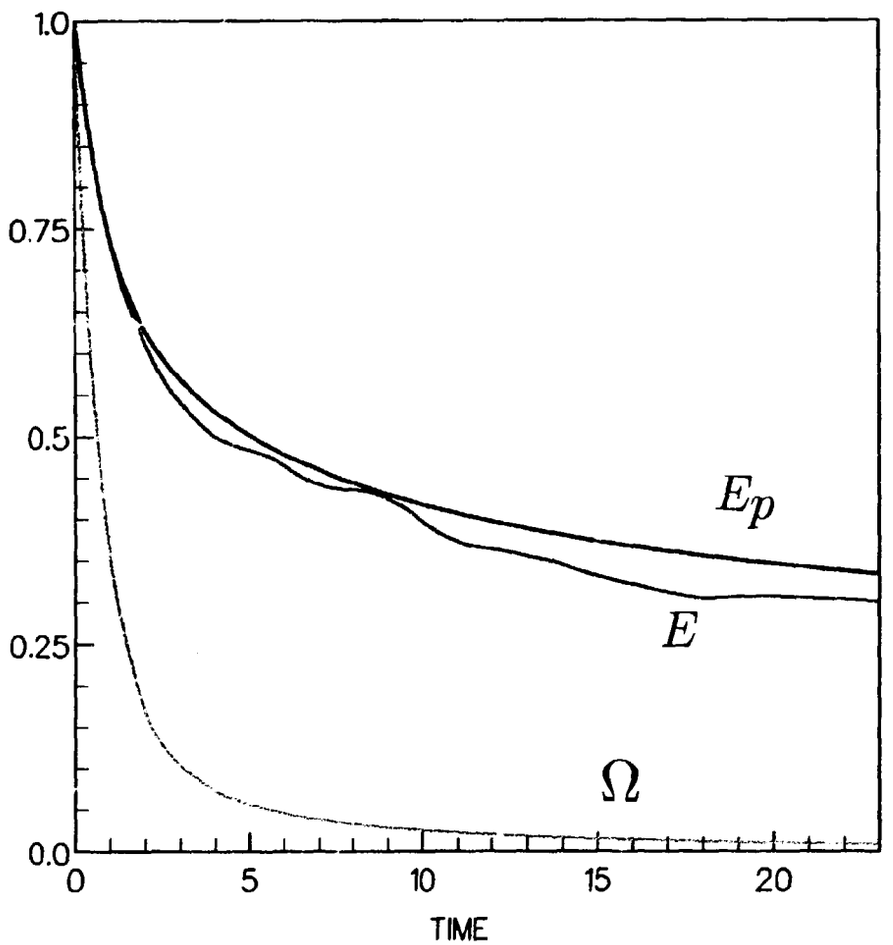

Figure 22. Energy, predicted energy and enstrophy evolution for the simulation shown in Figs.20 and 21. The curves have been normalized with their initial values.

to a good approximation, rotationally symmetric. As we are solving the Navier-Stokes equations using the charge as variable, we have to use Poisson's equation to calculate such a charge distribution:

$$\rho(r,\theta,t=0) = \frac{\rho_b}{2}\mathrm{sech}^2\left[\frac{r-r_d}{\Delta}\right]\left(\frac{1}{\Delta r}-\frac{2}{\Delta^2}\tanh[\frac{r-r_d}{\Delta}]\right) * (1+\mathrm{noise}), \quad (71)$$

where a small quantity of random noise ($\sim 2\%$) has been added to the initial condition, in order to initialize the instability. Δ must be chosen sufficiently small for the boundary conditions to be satisfied. We can accept a small (inevitable) divergence from the boundary conditions in the initial setup. When solving Poisson's equation and Helmholtz's equation the code will automatically adjust the solution to satisfy these conditions. Larger divergences will generate high frequency fluctuations and the code will thus become unstable.

A computer run using the initial conditions of eq. (71) is seen in Figs. 20, 21 and 22, where the spectral resolution is 64 Chebyshev modes and 256 Fourier modes. The evolution of ϕ' and ρ are shown as contour plots for twelve different times. Red/yellow colors correspond to positive values, blue to negative values. As the DC-potential profile found in eq. (68) is of no interest here, this contribution has been removed from the contour plots in Fig. 21, and we are thus only seeing the fluctuating part of the potential, i.e. $\phi' = \phi - \phi_{dc}$. Even though there is no azimuthal component in the initial condition, we note that the setup is very unstable and nearly immediately breaks up in many vortices. The vortices interact with each other and with the walls of the system and we see that there is a clear tendency of emergence of structures. At the end of this simulation we are left with only two potential vortices (a mode one) while we can identify five structures in the charge distribution. These structures will slowly rotate in the annulus due to the DC-velocity profile while their energy is damped out because of the viscosity term. The similarity to the experiment is clear the energy cascade from the high modes to the low modes of the system.

Figure 22 shows the evolution of the enstrophy, $\Omega(t)/\Omega(0)$, the energy, $E(t)/E(0)$, and the predicted energy, $E_p(t)/E_p(0)$, found according to eq. (66). All three curves have been normalized with their initial values. For the enstrophy we see that the setup is very unstable as the curve quickly (monotonously) decreases. For the energy we find a more moderate decay rate, a reasonable result as the enstrophy is the curl of the velocity and is therefore more effected by the introduced viscosity. For the relation between the simulated energy and the predicted energy evolution we see that there is a fair agreement, but oscillations occur in the simulated energy which is clearly not a feature of Navier-Stokes equations. At the start their decay rates are very similar (a difference of $10^{-4}\%$ has been found numerically), but at larger times a significant difference between the curves is noticeable. The simulation agrees fairly well with the Navier-Stokes equations, but for a spectral method we do expect more accurate behavior. The reason for this difference can either be that the number of modes in the system is too low or that the viscosity term must be evaluated for higher orders than the first order we have implied in the scheme.

To show another example of the inverse cascade of energy in this geometry an initial setup, corresponding to only one azimuthal mode exited and with a

exponential form in the radial direction will be shown. In the first simulation there were no azimuthal modes in the setup except for the random noise which has been added to the solution. Choosing a potential profile like:

$$\phi(r,\theta,t=0) = -\exp\left[-\frac{(r-r_d)^2}{\Delta}\right]\cos(k\theta) \tag{72}$$

will guarantee that all the energy is in the azimuthal mode k. Here r_d is again the position of the perturbation and Δ the size of it. The functional form of the charge distribution must again be found:

$$\begin{aligned}\rho(r,\theta,t=0) &= \left[\frac{4(r-r_d)^2}{\Delta^2} - \frac{4}{\Delta} + \frac{2r_d}{\Delta r} - k^2\right]\phi(r,\theta,t=0) \\ &\quad *(1+\text{noise})\,. \end{aligned} \tag{73}$$

These profiles satisfy the boundary conditions. Again some random noise has been added to the solution in order to initialize the instability and so that the solution does not become symmetric. A computer run with this initial condition is shown in Figs. 23, 24 and 25 using 64 Chebyshev modes, 256 Fourier modes and with $k = 15$ in eq. (73) Again the DC-potential profile has been removed from the contour plots in Fig. 24. For the charge distribution we see that the setup is very unstable and quickly breaks up in 15 dipoles and 15 smaller monopoles. Due to the noise we have added the evolution is not regular and soon loses its feature of the exited azimuthal mode number. The vortices start to interact and several vortex mergers can be seen, where a larger vortex rolls up a smaller vortex. At the end of the simulation we are left with only five structures which are so far apart from each other that they will be damped out of the system before any further interaction can take place. For the potential evolution we note that the evolution is more moderate than for the corresponding charge distribution Small-scale structures are not so dominant, but the emergence of vortices is noticeable and the flow is soon condensed to two positive and two negative structures (a mode two).

In Fig. 25 the energy, the predicted energy and the enstrophy evolution are shown. They have again been normalized with their initial values. The difference between the simulated energy and the predicted energy does have a similar behavior as before, but there is a significant difference at the start. Later their decay rates are very similar.

The inverse cascade is a well known phenomenon in two-dimensional flows. It was discovered by Fjørtoft already in 1953. Seyler *et al.* (1975) demonstrated that in an unbounded system, truncated at a maximum wave number and under certain initial conditions, the inverse cascade may result in a concentration of energy at the lowest possible wave number. This feature originates from the exact conservation of energy and enstrophy. Using a three-wave interaction theory (Knorr *et al.* (1990). Hasegawa (1985)) it can be shown that when enstrophy is transferred to small wavelengths energy will simultaneously be transferred to long wavelengths. However, Seyler *et al.* also showed that this will not always be the case but will depend on the initial conditions. An analogue to the three-wave interaction theory for a bounded flow is in general not directly obtainable. However, in simulations performed in similar geometries the inverse cascade is found play an important role in the dynamics of such flows (Marcus (1990), Ingersoll (1988)).

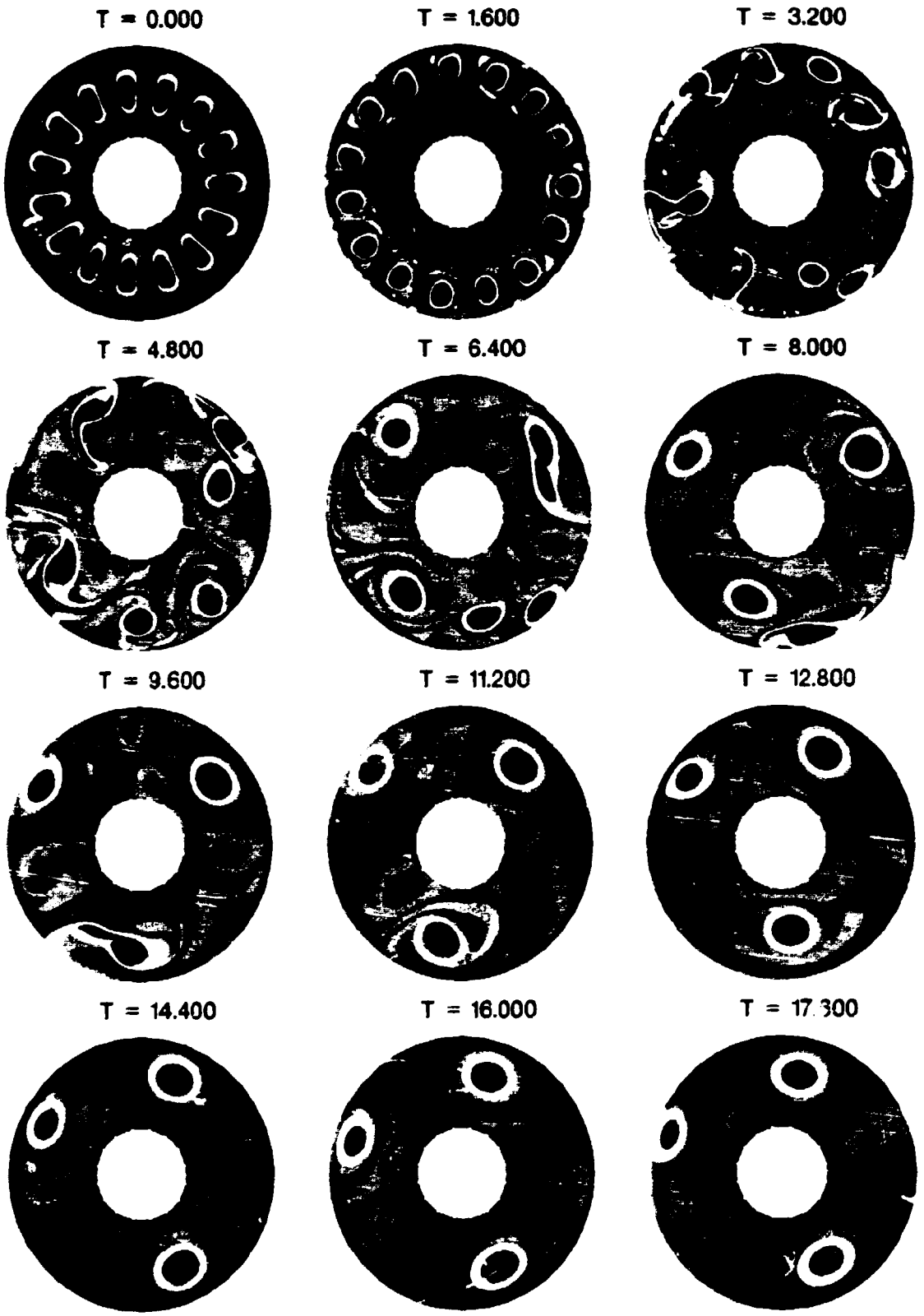
T = 0.000
T = 1.600
T = 3.200
T = 4.800
T = 6.400
T = 8.000
T = 9.600
T = 11.200
T = 12.800
T = 14.400
T = 16.000
T = 17.300

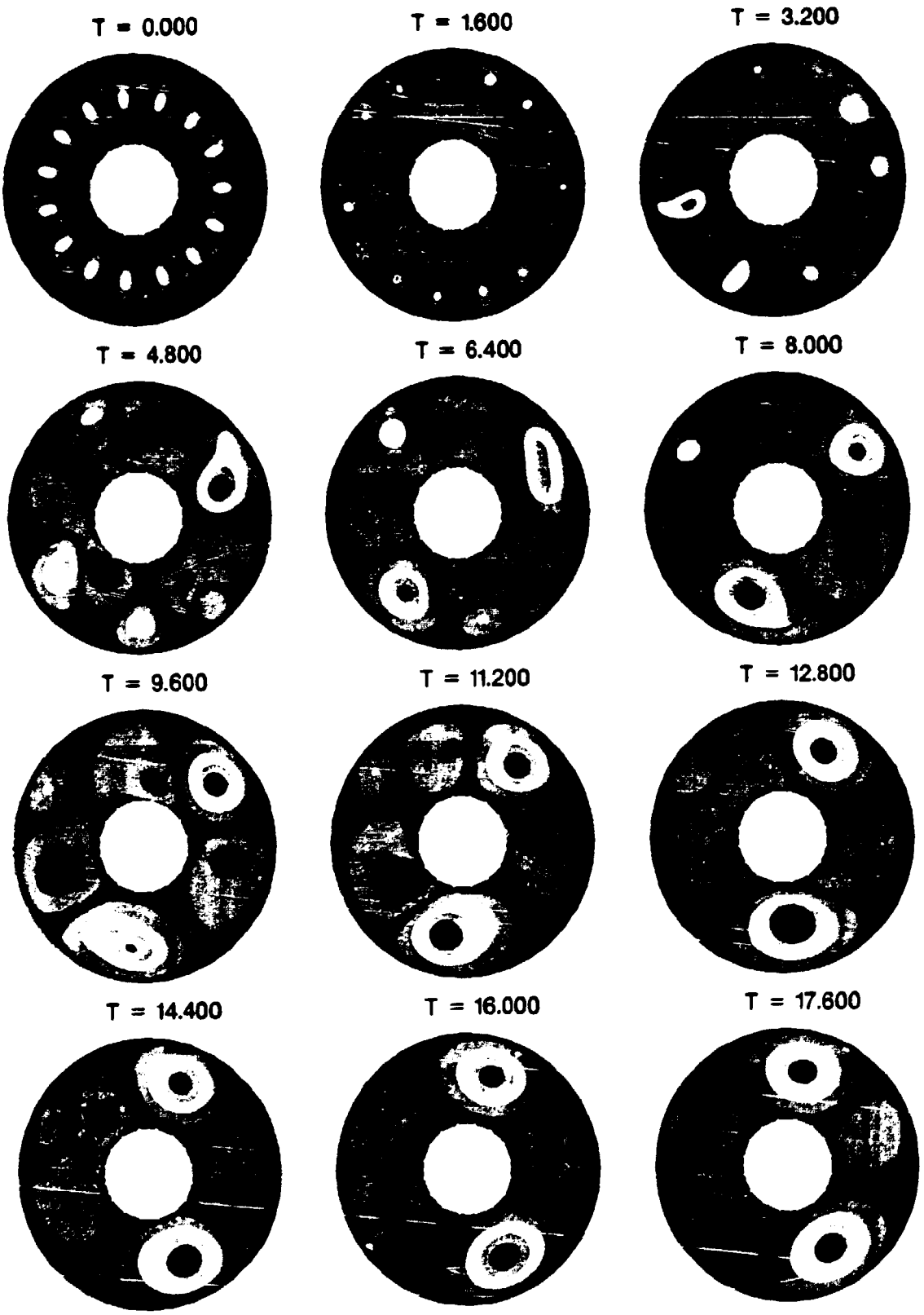

Figure 24 $\phi'(r,\theta,t)$ for the same twelve times as in Fig.22. The DC-potential variation has been removed from the solution.

3.8 Conclusions and Discussions

In this chapter an approximation method in terms of Chebyshev-Fourier expansion of the problem of free-slip boundary conditions for the Navier Stokes equations has been described. The method has been implemented on a computer and the numerical code has been used to simulate the dynamics of the experiments outlined in chapter 2. Two kinds of simulation have been presented.

In the first example a potential profile similar to the Q-machine experiments was initialized. Here a strongly sheared flow was confined to the central part of the annulus. The formation of a mode one in the potential profile was seen. A similar linear stability theory may easily be applied to the initial condition in the simulation, see section 2.3. The result is that all modes for $m \geq 2$ are unstable (in the dissipation free limit). It is particularly interesting to note that $m = 1$ is linearly stable. But this mode appears clearly in the saturated state of the turbulence, and it is exited by the nonlinear inverse cascade process. Thus, the saturated spectrum does not necessarily bear much information about the linear stability properties. The numerical results support the experimental results in the formation of large-scale structures. In the other example only a high azimuthal mode was initialized. Also this simulation reveals the same kind of self-organization, and one can therefore conclude that what we are seeing is a general physical behavior in such a geometry.

The developed code is thus a good tool to test the dynamics of the Q-machine experiments but it is not restricted to plasma physics only. As mentioned in the introduction, the Navier-Stokes equation is a general equation for the dynamics of fluids. In particular it may be used for simulation of the formation of vortices in a rotating fluid with shear. Such an experiment has recently been started in the Optics and Fluid Dynamics Dept.. Here the boundary conditions will be no-slip, which can readily be implemented, see Coutsias and Lynov (1991).

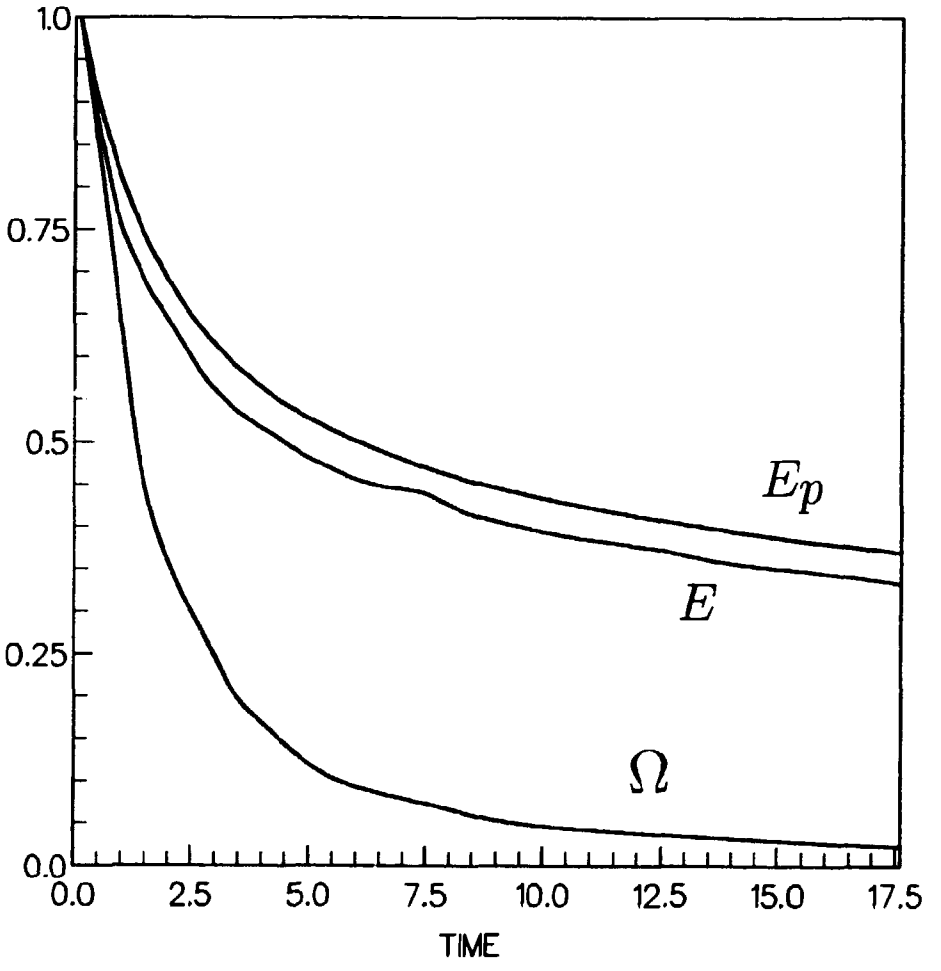

Figure 25. Energy, predicted energy and enstrophy evolution for the simulation shown in Figs. 22 and 23. The curves have been normalized with their initial values.

4 Studies of the Eulerian-Lagrangian Transformation in Two-Dimensional Flows

4.1 Introduction

In the present study we take advantage of the ease with which two-dimensional flows can be simulated numerically, using a generalized version of Onsager's interacting line vortex model (1949). In particular some specific theoretical results of Wandel and Kofoed-Hansen (1962) and Pécseli and Mikkelsen (1985) for the relations between Eulerian and Lagrangian averages can then be tested with good accuracy under well defined conditions in two dimensions, although the results in their most general form are applicable to fully three dimensional conditions as well.

Originally Wandel and Kofoed-Hansen (1962) set out to provide a theoretical basis for the hypothesis of Hay and Pasquill (1960) which gives a phenomenological relation between the power spectra $P_L(\omega)$ and $P_E(\omega)$ obtained by Lagrangian and Eulerian sampling, respectively, of the turbulent velocity fluctuations. They suggested a simple scaling as

$$P_L(\omega) \simeq \beta P_E(\beta\omega) \ , \tag{74}$$

where the constant β was determined empirically to be in the range of $2 < \beta < 4$. In terms of the correlation functions the relation (74) becomes

$$R_L(\beta\tau) \simeq R_E(\tau) \ . \tag{75}$$

Rather than approaching the problem by the Navier-Stokes equation Wandel and Kofoed-Hansen (1962) considered an autonomous system which for certain parameters has turbulence-like features. They thus assumed a flow field $\mathbf{v}(\mathbf{r},t)$ obtained by superposition of many structures, i.e.

$$\mathbf{v}(\mathbf{r},t) = \sum_{l}^{N} \mathbf{u}_l(\mathbf{r}-\mathbf{r}_l) \ . \tag{76}$$

An autonomous model is obtained by requiring that individual structures are convected by the flow generated by all the others, i.e.

$$\frac{d\mathbf{r}_l(t)}{dt} = \sum_{k\neq l}^{N} \mathbf{u}_k(\mathbf{r}_l-\mathbf{r}_k) \tag{77}$$

By studying systems described in eqs. (76) - (77) with some simplifying assumptions Wandel and Kofoed-Hansen (1962) suggested a value for β in eqs. (74) - (75) which depended explicitly on the r.m.s. value of the velocity fluctuations and the mean flow velocity, $\langle v\rangle$, as $\beta = (\sqrt{\pi}/4)\ (\langle v\rangle/u')$, where $u'^2 \equiv \frac{1}{3}\langle u^2\rangle$ in three dimensions in the limit where $\langle v\rangle \gg u'$. This result has been recognized in the literature, see e.g. Panofsky and Dutton (1984). The analysis is, however, much more general and contains a fundamental result in terms of explicit relations between Eulerian and Lagrangian velocity correlations. It is our aim to study and analyze these relations. For this purpose a numerical code has been developed in which a system containing a large number of structures and evolving in accordance with eqs. (76) - (77) is simulated. Although the formulation of these equations allows, in principle, a full three dimensional modelling, our calculations are, as mentioned, restricted to two dimensions. This analysisis is relevant also to other

physical systems, such as certain types of low-frequency plasma turbulence, which may be quite well described by the two-dimensional model outlined in Chapters 2 and 3 (see also Joyce and Montgomery (1973), Seyler *et al.* (1975), Huld *et al.* (1988), Knorr and Pécseli (1989)).

In two dimensions eqs. (76) and (77) are conveniently rewritten as

$$\mathbf{v}(\mathbf{r},t) \;=\; \nabla\Phi \times \hat{e} \;=\; \sum_{l}^{N} \nabla\phi_l(\mathbf{r}-\mathbf{r}_l(t)) \times \hat{e} \;, \tag{78}$$

and

$$\frac{d\mathbf{r}_l(t)}{dt} \;=\; \sum_{k\neq l}^{N} \nabla\phi_k(\mathbf{r}_l-\mathbf{r}_k) \times \hat{e} \;, \tag{79}$$

where the introduction of the stream function, Φ, ensures that the flow is incompressible, $\nabla\cdot\mathbf{v}(\mathbf{r},t)=0$. The unit vector, $\hat{e}$, is perpendicular to the plane confining the system. The vorticity associated with the flow is $\omega=\nabla^2\Phi=\sum_l^N \nabla^2\phi_l(\mathbf{r}-\mathbf{r}_l)$. The number of structures in the system, N, is varying randomly over the ensemble of realizations according to a Poisson distribution. Elements of this model can also be found in the paper by Chorin (1973). In particular, Onsager's line-vortex model (1949) is a special case of eqs. (78) - (79) with the choice $\phi_k(\mathbf{r}) = A_k \ln(|\,\mathbf{r}\,|)$. It is readily demonstrated that the dynamic system of structures described by eqs. (78) - (79) can be put in a Hamiltonian form for $\phi_k = A_k F(|\,\mathbf{r}\,|)$, where $F(r)$ is an arbitrary function and A_k is a constant. With

$$H \;=\; -\frac{1}{2\pi}\sum_{l>k} A_l A_k F(|\,\mathbf{r}_l-\mathbf{r}_k\,|) \;, \tag{80}$$

the generalized coordinates are related to the (x,y) coordinates in configuration space by

$$(q_l,p_l) \;=|A_l|\,(x_l, y_l\,\mathrm{sign}(A_l)) \;, \tag{81}$$

i.e. $dp_l/dt = -\partial H/\partial q_l$ and $dq_l/dt = \partial H/\partial p_l$. The notation $l>k$ in the summation in eq. (80) indicates that each pair of structures is counted only once. The Hamiltonian, eq. (80), accounts for an effective potential energy of the interacting structures, which is evident by considering the particular line vortex model. The system does not possess any kinetic energy in the usual sense. The Hamiltonian, eq. (80), applies in the absence of boundaries. The presence of periodic boundary conditions requires the introduction of a modified potential for F (Ewald, 1921).

From the construction it is clear that the individual structures, specified by ϕ_i in eqs. (78) and (79) or by F in eq. (80), are not distorted by the flow. The length scales of the structures are thus imposed *a priori* and will characterize the flow at all times. However, any macroscopic arrangement of many individual structures will be distorted and sheared by the flow. The velocity field, eq. (78), will therefore have properties in common with flows described by two-dimensional Euler equations although the two equations governing the time evolutions of the flows are different. Evidently any flow described by eq. (78) with smooth initial condition will remain smooth for any later time, i.e. no discontinuities will develop. Also these properties are consistent with those characterizing flows described by the Euler equation in two dimensions (Sulem and Sulem (1983), and Sulem *et al.* (1983)).

From eq. (81) it is readily concluded that phase space is finite for a confined system. Onsager (1949) pointed out that for such systems the temperature may

take on negative values. In such cases the system is expected to be characterized by an ordering of structures appearing as a clustering of structures having the same sign of the amplitude, A_k, as discussed also by Joyce and Montgomery (1973) and Montgomery and Joyce (1974). This clustering can be argued in a particularly simple way for the line vortex model: for a finite physical domain the only way to increase the energy content of the system indefinitely is to place like-signed line vortices close to each other, resulting in macroscopically organized structures. (Recall that $T = dQ/dS$, where T is the temperature, Q is the energy while the entropy S can be taken as a measure of the disorder of the system. The inverse temperature is a measure of the change of disorder of a system per unit change in energy. The actual value of the system energy where the temperature changes sign is subject to some controversy.) On the other hand, the positive temperature states, which will be studied in the present work, are expected to be characterized by complete randomness, i.e. a structure can at any time be found with equal probability in any area element of phase space, irrespective of the position of the other structures. Explicit use of this feature will be made in the subsequent analysis.

Our analysis was restricted to two spatial dimensions in order to reduce the demands for computer resources. Even this restricted study is, however, of physical relevance in connection with certain types of low frequency electrostatic turbulence in strongly magnetized plasmas (Huld *et al.* 1988). In these cases magnetic field lines can be considered equipotential, and a two-dimensional description (Joyce and Montgomery, 1973) in the plane perpendicular to the magnetic fields is appropriate. It is interesting to note that in this problem the electrostatic potential, which is a readily measurable quantity, takes the role of the stream function. Turbulent diffusion of charged particles across magnetic field lines is a particularly pertinent problem for present day fusion research.

4.2 Analytical Results

In the first part of this section we will summarize the main results obtained by Wandel and Kofoed-Hansen (1962), given in more detail by Kofoed-Hansen and Wandel (1967). Their study is concerned with model systems described by eqs. (76) - (77), which are analyzed in certain limits described by parameters characterizing the system. One of the parameters is the normalized density of structures, μ, while another one, ϵ, is a characteristic of the wavenumber spectrum of the turbulence, expressed in terms of wavenumbers raised to some power and averaged over the entire spectrum. The most important of these two parameters is μ which for a given area of the system is a measure of the average number of structures, i.e. the number of degrees of freedom in the system. In this sense μ can be interpreted as being proportional to an effective Reynolds number.

Summary of Basic Analytical Results

In the present work we study in particular the correlation functions of the velocity fluctuations. The velocity field is sampled either along a trajectory $\mathbf{r} = \mathbf{r}(t)$, where $\mathbf{r} = \mathbf{v}_0 t$ with $\mathbf{v}_0 = \text{constant}$, which corresponds to Eulerian sampling (in particular we may have $v_0 = 0$), or along $\mathbf{r}(t) = \int_0^t \mathbf{v}(\mathbf{r}(\tau), \tau)\, d\tau$ with $\mathbf{v}$ given by eq. (78), which corresponds to the Lagrangian sampling with velocity $\mathbf{u}(t) = \mathbf{v}(r(t), t)$. The

normalized Lagrangian correlation functions can be written as a series expansion (Hinze 1975)

$$R_L(\tau) \equiv \langle \mathbf{u}(t) \cdot \mathbf{u}(t+\tau) \rangle$$
$$= 1 + \sum_{n=1}^{\infty} \tau^{2n} \frac{(-1)^n}{(2n)!} \frac{\langle (d_t^n \mathbf{u})^2 \rangle}{\langle u^2 \rangle} , \tag{82}$$

where angular brackets denote ensemble averages. Time stationarity is assumed, i.e. R_L is a function of time separations only and does not explicitly depend on both t and τ. The symmetry property $R_L(\tau) = R_L(-\tau)$ was explicitly used. It is assumed that each of the terms in eq. (82) is finite and that $R_L(\tau \to \infty) \to 0$. Situations may formally exist where the series (eq. (82)) diverges or the series expansion is not feasible. These cases are not considered here. As the first step the eigenmotion of the structures is ignored, i.e. $\mathbf{r}_l$ = constant in eqs. (76) - (77). This limit corresponds to analyzing the transport properties of a frozen flow where the velocity varies with position but not with time. In the limit $\mu \to \infty$ and $\epsilon \to 0$ a basic result of Wandel and Kofoed-Hansen (1962) admits the approximation

$$\langle (d_t^n \mathbf{u})^2 \rangle = \langle [(\mathbf{u} \cdot \nabla)^n \mathbf{u}]^2 \rangle \approx \langle (|\mathbf{u}|^n (\hat{e} \cdot \nabla)^n \mathbf{u})^2 \rangle$$
$$\approx \langle u^{2n} \rangle \cdot \langle [(\hat{e} \cdot \nabla)^n \mathbf{u}]^2 \rangle , \tag{83}$$

for homogeneous, isotropic turbulence, where $\hat{e}$ is an arbitrary unit vector. Introducing the power spectrum $\mathcal{E}(k)$ for the velocity fluctuations we use the definition for $\langle k^{2n} \rangle = \int_0^\infty k^{2n} \mathcal{E}(k) dk$. Equation (83) can then be rewritten as

$$\frac{\langle (d_t^n \mathbf{u})^2 \rangle}{\langle u^2 \rangle} \approx \langle u^{2n} \rangle \langle k^{2n} \rangle . \tag{84}$$

In the limit of large μ and randomly distributed structures, the components of $\mathbf{u}$ are normally distributed by the central limit theorem, and $\langle u^{2n} \rangle$ is readily calculated for all n. In particular $\langle u^2 \rangle = \int_0^\infty \mathcal{E}(k) dk$. It was subsequently demonstrated that the random motion of the individual structures could be accounted for simply by replacing $\mathbf{u}$ in $\langle u^{2n} \rangle$ by the average velocity difference between individual structures and the test particle. Since structures are transported like particles according to eq. (79), their velocity distribution can be taken to be the same Gaussian as that of the test particle. Since many structures contribute to the local particle velocity, the respective velocity of an individual structure and a particle may be considered statistically independent to a good approximation. With these approximations applied to the two-dimensional geometry, Pécseli and Mikkelsen (1985) obtained

$$R_L(\tau) = \int_0^\infty \mathcal{E}(k) W(k\tau \langle u^2 \rangle^{\frac{1}{2}}) dk , \tag{85}$$

where

$$W(\zeta) = 1 - \zeta e^{-\frac{1}{2}\zeta^2} \int_0^\zeta e^{\frac{1}{2}\gamma^2} d\gamma . \tag{86}$$

The function $W(\zeta)$ is closely related to the Dawson integral. The differences in $R_L(\tau)$ for two and three dimensions originate in the calculations of $\langle u^{2n} \rangle$ in eq. (83) with a Gaussian distribution of the two, or three, velocity components.

The Eulerian velocity correlation function $R_E(\tau)$ can be calculated in a similar way. Considering first the frozen flow, the velocity field is sampled along a trajectory $\mathbf{r} = \mathbf{v}_0 t$ with constant probing velocity $\mathbf{v}_0$, i.e. $\mathbf{v}(t) = \mathbf{v}(r = \mathbf{v}_0 t)$ for this

case. An expression corresponding to eq. (82) is of course also valid for $R_E(\tau)$, but eq. (83) is now replaced by

$$\begin{aligned}\langle (d_t^n \mathbf{v})^2 \rangle &= \langle [(\mathbf{v_0} \cdot \nabla)^n \mathbf{v}]^2 \rangle = \langle (|\mathbf{v}_0|^n (\mathbf{e} \cdot \nabla)^n \mathbf{v})^2 \rangle \\ &= v_0^{2n} \langle [(\mathbf{e} \cdot \nabla)^n \mathbf{v}]^2 \rangle \end{aligned} \tag{87}$$

or

$$\frac{\langle (d_t^n \mathbf{v})^2 \rangle}{\langle v^2 \rangle} = v_0^{2n} \langle k^{2n} \rangle \ . \tag{88}$$

which is now an exact relation. The random motion of structures was accounted for by replacing v_0 in eq. (88) by the velocity difference between the probe and the local flow velocity, i.e. writing

$$\frac{\langle (d_t^n \mathbf{v})^2 \rangle}{\langle v^2 \rangle} \approx \langle |\mathbf{v}_0 - \mathbf{v}|^{2n} \rangle \langle k^{2n} \rangle \ , \tag{89}$$

where $\mathbf{v}$ on the right-hand side is assumed to have components with a Gaussian distribution, using the same arguments as before. The explicit result is given by Pécseli and Mikkelsen (1986) as

$$R_E(\tau) = \int_0^\infty \mathcal{E}(k) S(k\tau u', \frac{v_0}{u'}) \, dk \ , \tag{90}$$

where $u'^2 \equiv \frac{1}{2}\langle v^2 \rangle$ and

$$S(x,y) = e^{-\frac{1}{2}y^2} \int_0^\infty \cos(x\gamma) e^{-\frac{1}{2}\gamma^2} I_o(y\gamma) \, \gamma \, d\gamma \ , \tag{91}$$

where I_o is the modified Bessel function of the first kind of order zero. In particular, for homogeneous incompressible flows we have the mean square velocity fluctuations being independent of the actual sampling (Eulerian/Lagrangian), i.e. $\langle u^2 \rangle = \langle v^2 \rangle$. The expression for the two-time, two-point correlation function $R_E(\zeta, \tau) = \langle \mathbf{v}(\mathbf{r}, t) \cdot \mathbf{v}(\zeta + \mathbf{r}, t + \tau) \rangle$ can be obtained from eq. (90) by simply replacing v_0 by ζ/τ. It can be shown that $R_E(0, \tau)$ has a simple relation to $R_L(\tau)$ in eq. (85). In this limit the two functions become identical, apart from a factor $\sqrt{2}$ in the argument, see Wandel and Kofoed-Hansen (1962) or Pécseli and Mikkelsen (1986).

The normalized wavenumber spectrum $\mathcal{E}(k)$ entering eqs. (85) and (90) is given by the Fourier transform of the spatial correlation function $\langle \mathbf{v}(\mathbf{r}, t) \cdot \mathbf{v}(\mathbf{r} + \zeta, t) \rangle / \langle u^2 \rangle = R_{11}(\zeta) + R_{22}(\zeta)$, i.e. the sum of the longitudinal and lateral correlation functions. The spatial correlation tensor $\langle v_i(\mathbf{r}) v_j(\mathbf{r} + \zeta) \rangle$ has the general form

$$R_{ij}(\zeta) = g(\zeta)\delta_{ij} + [f(\zeta) - g(\zeta)] \frac{\zeta_i \zeta_j}{\zeta^2} \ . \tag{92}$$

With the stream function introduced before, these correlation functions can be given a simpler form with

$$f = -\frac{1}{\zeta} d_\zeta R_\Phi(\zeta)/R_\Phi'' \ \text{ and } \ g = -d_\zeta^2 R_\Phi(\zeta)/R_\Phi'' = d_\zeta(\zeta f) \ , \tag{93}$$

where $R_\Phi(\zeta)$ is the scalar spatial correlation function for the stream function, where $R_\Phi(\zeta \to \infty) \to 0$ by choice of reference level, and $R_\Phi'' \equiv -d_\zeta^2 R_\Phi(\zeta = 0)$. Note that homogeneous and isotropic two-dimensional turbulence does not possess any lateral integral scale, i.e. $L_g \equiv \int g(\zeta) \, d\zeta = 0$. The longitudinal length scale $L_f \equiv \int f(\zeta) \, d\zeta$ is nonvanishing. The properties of the correlation tensor (eq. (92)) and the spectral tensor for a two-dimensional system are discussed by for instance

Pécseli and Mikkelsen (1985). Fourier transformation of the correlation function gives $\mathcal{E}(k) = 2/\pi \int_0^\infty [f(\zeta)+g(\zeta)]\cos(k\zeta)\,d\zeta$, by use of eq. (92) (see also Batchelor (1953)).

The wavenumber spectrum can, however, be calculated from first principles when the form of the individual structures in eqs. (78) and (79) and their densities are known. It is most convenient to work with the stream function $\Phi = \sum_i \phi_i(\mathbf{r}-\mathbf{r}_i)$ according to eq. (78). The correlation function R_Φ is by standard methods (Rice, 1944) obtained as

$$\begin{aligned} R_\Phi(\zeta) &\equiv \langle \Phi(\mathbf{r})\Phi(\mathbf{r}+\zeta)\rangle \\ &= \sum_l \mu_l \int \phi_l(\mathbf{r})\phi_l(\mathbf{r}+\zeta)d\mathbf{r} \end{aligned} \tag{94}$$

where it is assumed that the structures are uniformly distributed in space with statistically independent positions. The summation in eq. (94) runs over all structure shapes with individual densities μ_l. A possible DC-contribution in eq. (94) is assumed to vanish by symmetry arguments, i.e. positive and negative amplitudes of a structure are assumed to be equally probable. Note that $R_\Phi(0) \neq 1$.

The present model allows the generation of a random flow which according to eq. (94) can reproduce an arbitrary, prescribed, spatial correlation function and therefore an arbitrary wavenumber spectrum. This is possible even with the use of only <u>one</u> type of randomly distributed structures. Given R_Φ in eq. (94) a spatial structure for ϕ_l can be prescribed in indefinitely many ways since the convolution implied in eq. (94) is insensitive to a phase factor. When only one type of structure is present (with both signs being equally probable), the problem is fully specified if both the correlation function and the triple correlation function are specified. In particular we have $\langle u^2\rangle \equiv 2u'^2 = 2R_\Phi''$ from eqs. (93) and (94).

Simplified Derivation

It is evident that the analysis summarized in the present section cannot accommodate <u>arbitrary</u> spatial variations for the structures defined by $\phi_l(\mathbf{r})$ in eq. (94). Although the line vortex model can be described by eqs. (78) and (79), the introduction of the corresponding logarithmic stream function in eq. (94) will give rise to a divergence of the integral. It is worth pointing out that the main results summarized in section 4.2 can be obtained by quite different arguments, which may by helpful in providing an insight into the physical implications of the approximations made by Wandel and Kofoed-Hansen (1962) in their analysis. For this purpose consider first a frozen flow, where the wavenumber spectrum is known by Fourier transform of eq. (94). Let this flow realization move with constant velocity u. A stationary observer will obtain a time varying signal with an Eulerian correlation function given by

$$R_E(\tau \mid u) = \int_0^\infty \mathcal{E}(k)\cos(ku\tau)dk \ . \tag{95}$$

Now let u be randomly varying over the realizations of the ensemble. Assuming a Gaussian distribution for the components of u we have the probability density $(u/u'^2)\exp(-\frac{1}{2}(u/u')^2)$ for its magnitude, giving

$$R_E(\tau) = \int_0^\infty \mathcal{E}(k)\int_0^\infty \gamma\cos(ku'\tau\gamma)\exp(-\frac{1}{2}\gamma^2)\,d\gamma\,dk\,, \tag{96}$$

reproduction, eq. (90) with $v_0 = 0$. Also the result for $v_0 \neq 0$ can be reproduced with a little more algebra, along the lines indicated here. It thus seems as if the essentials of the analysis resulting in eq. (90) amount to assuming that structures are swept rapidly past an observer in such a way that the flow velocity convecting individual structures in each realization can be considered constant in the time interval it takes a structure to propagate its own diameter. The Gaussian distribution for the velocity can be argued as already discussed.

Also the expression (85) for the Lagrangian correlation function can be argued in a similar way. Consider a test particle being transported by the flow with a velocity $\mathbf{v}$ which will be considered essentially constant in a finite time interval. The flow generating $\mathbf{v}$ at the particle position is composed of a large number of overlapping structures. Out of all these structures those having velocities in a narrow interval around $\mathbf{u}$ are selected. The number of overlapping structures is assumed to be so large that the selected group will have a contribution to the spectrum $\mathcal{E}(k)$ which is independent of $\mathbf{u}$. This requirement is trivially satisfied if all the structures are identical. Their contribution to the time-varying correlation function experienced by the test particle will of course depend on the selected velocity $\mathbf{u}$ as

$$R_L(\tau \mid \mathbf{v}, \mathbf{u}) = \int_0^\infty \mathcal{E}(k) \cos(k\tau \mid \mathbf{u} - \mathbf{v} \mid) \, dk \ . \tag{97}$$

Again $\mathbf{v}$ and $\mathbf{u}$ will be varying over all realizations having the same Gaussian probability density with standard deviation u'. (An interesting special case can be argued, where the probability densities of $\mathbf{v}$ and $\mathbf{u}$ are different. See Wandel and Kofoed-Hansen (1962).) However, the probability density for $|\mathbf{u} - \mathbf{v}|$ is then also a Gaussian with standard deviation $\sqrt{2}u'$. Salu and Montgomery (1977) use a somewhat similar argument in their discussion of Corrsin's hypothesis (Corrsin, 1960). As one consequence we find that R_L is trivially related to $R_E(0, \tau)$, see Lynov *et al.* (1990) Another confirmation of this result can be obtained by eq. (90) and noting that the foregoing arguments simply state that v_0 should be considered as a random variable with probability density $(v_0/u'^2)\exp(-\frac{1}{2}(v_0/u')^2)$. Carrying out the averaging over v_0 using $\int_0^\infty x \exp(-x^2) I_0(\beta x) dx = \frac{1}{2}\exp(\beta^2/4)$ the same result is obtained again. It is worth noting that the present summary reproduces the main results of Wandel and Kofoed-Hansen (1962) irrespective of the use of the series expansion implicit in eq. (82).

A particular consequence of the simple relation between $R_L(\tau)$ and $R_E(\tau)$ in the present analysis is the corresponding relation between Lagrangian and Eulerian integral time scale, i.e. $\tau_E = \tau_L\sqrt{2}$. The literature seems somewhat ambiguous concerning the relation between these two quantities. On one hand Lumley and Panofsky (1964) argued that $\tau_E < \tau_L$ since the Eulerian measurement correlates at every instant new fluid at the observation point, whereas the Lagrangian correlation deals always with the same fluid. Velocities are supposed to be more persistent along the path of a fluid particle than at a fixed observation point. Alternatively, Kraichnan (1964) argued that the frozen random flow presents a limiting case where, obviously, τ_E is infinite, while he expected τ_L to be finite. Also Leslie (1973) argued for $\tau_E > \tau_L$, by noting that measurements in a fixed position are sensitive to the long period (i.e. large-scale) disturbances. The Lagrangian correlation is swept around by these disturbances and should, therefore, be much less affected by them. It is interesting that the present model analysis supports the arguments for $\tau_E > \tau_L$. The ratio of Eulerian to Lagrangian micro

time scale is $\tau_{mE}/\tau_{mL} = \sqrt{2}$ in the present model, i.e. the same as the ratio of the integral time scale. Tennekes (1975) has argued for $\tau_{mE}/\tau_{mL} \sim 1/R_e^{1/4}$ in three-dimensional flows, where R_e is the Reynolds number, i.e. $\tau_{mE} \ll \tau_{mL}$. The applicability of these results for moderate or small R_e has been criticized, however, by Yeung and Pope (1989).

4.3 Numerical Results

A numerical code has been developed in order to simulate a system containing a large number of structures which evolve according to eqs. (76) - (77), written in normalized units. The code is in principle quite straightforward and need not be described in particular detail. The calculations are carried out in double precision and the displacement in the coordinates of the individual structures is followed. This is a rather time consuming procedure which, for computational reasons, restricts the number of structures to at most a few thousand. Typically, in the simulations described in the following sections we used 1800 interacting structures with imposed symmetry conditions to be described. A significant increase in the number of structures would require interpolation in a grid representation of the flow. The resulting numerical inaccuracy could give rise to a randomness in the structure trajectory which would be in disagreement with the one assumed in the model. Our calculations are carried out in a large square system with side length $3L$, with the requirement that the number of structures in each of the 9 cells with area L^2 is the same. A symmetry requirement is imposed by generating 8 positions from positions of structures in the central cell, i.e. a position (x_l, y_l) gives rise also to $(x_l \pm L, y_l)$, $(x_l, y_l \pm L)$ and $(x_l \pm L, y_l \pm L)$. This procedure ensures that the number of structures in each of the 9 cells is constant i.e. if a structure leaves a cell, another one enters simultaneously at the opposite position in the same cell. The procedure outlined here is effectively tantamount to impose periodic boundary conditions provided L is much larger than the spatial extent of any structure in the system. The time stepping is accomplished by a partially corrected Adams-Bashforth scheme of 3rd order, see Gazdag (1976), except for the first step which is a simple Euler step, and the second one which is a leap-frog step. For Hamiltonian systems the conservation of H in eq. (80) is used as a test for the accuracy of the code for a given time step. Simple cases with only two structures in the central cell are used for additional tests. Here the solution is known exactly. For the simulations discussed in the following the initial positions of the structures were generated by standard random number generators on the computer. Test runs (not discussed here) were carried out for other initializations.

Spatial correlations are obtained by recording time series for velocity components in selected points along the diagonal of a subcell with side length $L/2$. The correlation length of the fluctuating fields as obtained from eq. (90) is smaller than $L/2$ in all investigated cases. Likewise, the correlation time is smaller than the time it takes, on average, a vortex to traverse the distance $L/2$. The periodicity of our system can be ignored, and the subcell considered as representative for an element of an extended, homogeneous and isotropic flow. Lagrangian correlations are obtained both by following test particles in the flow and for self-consistently moving structures.

The analysis summarized in section 4.2 is in principle applicable for any shape of the structures (provided the integral exists) but the resulting expressions will

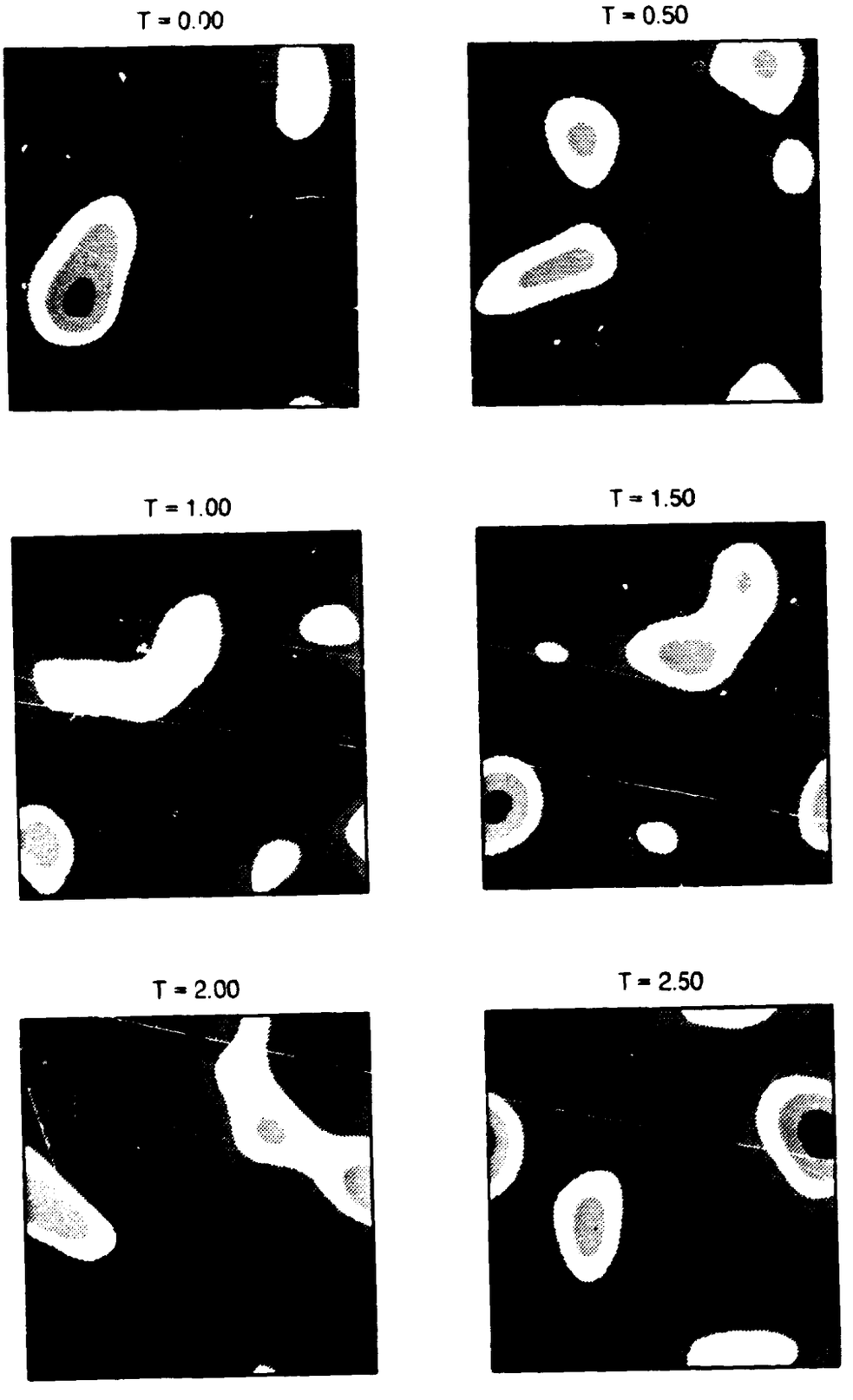

Figure 26. Time sequence showing the evolution of the stream function for 200 structures of each polarity with $|A_l| = 1$ and $\delta_l = \frac{1}{2}$. Note that individual structures cannot be discriminated by visual inspection. High values are red whereas low values are blue in the plot. The full system is periodic, as explained in the text

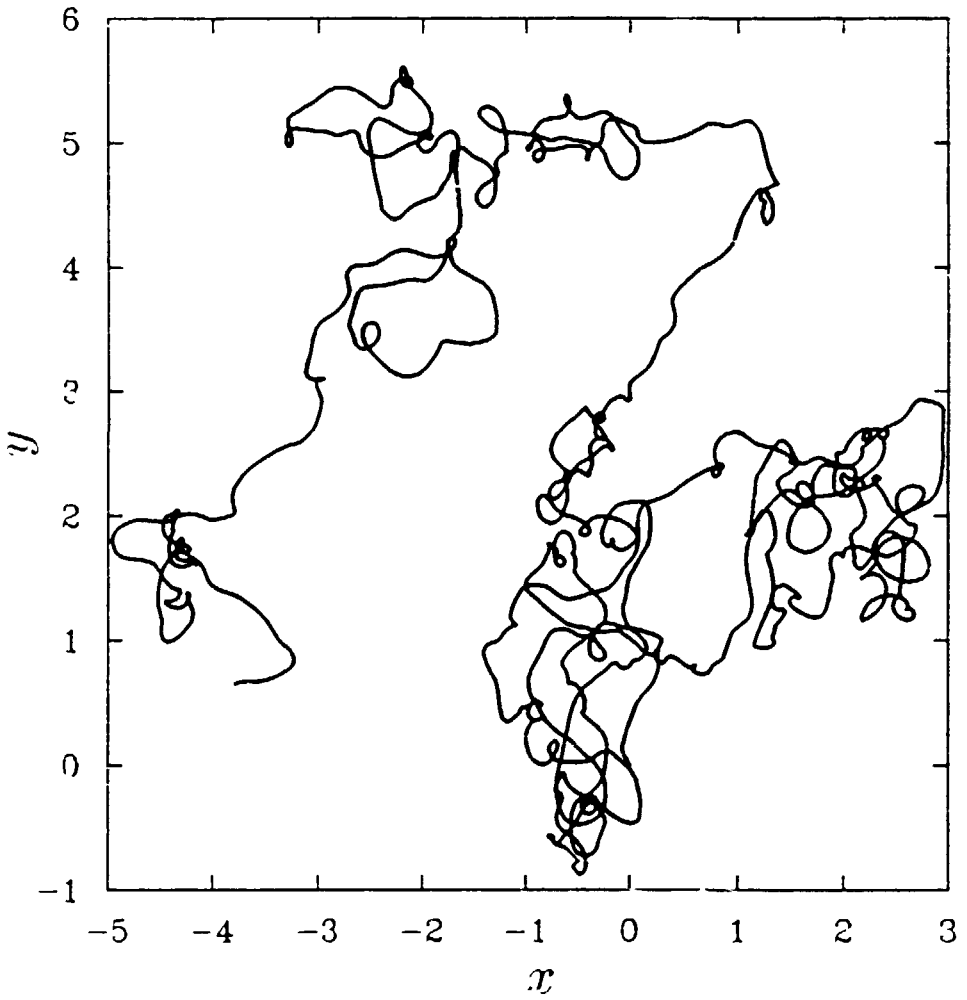

Figure 27. Trajectory of one typical vortex, initially at $(x, y) = (0,0)$. Parameters are as in Fig. 26.

in general have to be solved numerically. In the present study we consider only the case where the individual structures are described by

$$\phi_l = A_l \exp(-r^2/\delta_l) \quad , \tag{98}$$

characterized by only two parameters, A_l and δ_l. With this simple form all our expressions from section 4.2 can be solved analytically. Here we only consider the case where δ_l is the same for all structures and where only A_l is varying with l. This system was shown to be Hamiltonian in section 4.1. As an illustration we give a time sequence for the evolution of the stream function in fig.26 together with the trajectory of a typical vortex.

In all considered cases we had $\delta \ll L$. The periodicity imposed on the distribution of structures, which is a convenient computational simplification, is therefore immaterial for the interpretation of the numerical results. The computations were rather time consuming, and for practical reasons the density of structures could not be made arbitrarily large. Because the flows are composed of many overlapping structures these are not individually discernible in a realization as in fig.26. We note, however, that incidental groups or clusters of structures (see e.g. the white or black regions in fig.26) will be deformed and distorted by the flow, as discussed in the Introduction.

Structures with Same Widths and Amplitudes

First we consider the case where $\delta_l = \delta$ and $|A_l| = A$ for all l with an equal number of structures of the two polarities. The most important parameter for the problem is the density of structures $\mu = N/L^2$ where N is the number of structures in a cell. A central assumption in the analysis summarized in section 4.2 was that the velocity components have a Gaussian probability density, which follows from the assumption that many structures contribute to the velocity at a selected point. The number of overlapping structures is on average of the order $4\delta\mu$. It is well known, however, that this quantity need not be particularly large, i.e. a number larger than 4-5 will suffice for producing a probability density which is in practice indiscernible from a Gaussian. We characterize the probability density for the velocity components by its lowest order moments, i.e. standard deviation, skewness, and kurtosis. In fig.28 we show the variation of these three quantities for varying δ and two values of μ. The results are obtained as an average over an interval of 24 time units (i.e. 2400 time steps). For reference we give, by full lines, the variations according to our model.

The value for $\langle u^2 \rangle$ used in fig.28 was determined by first calculating the stream function correlation function obtained from eq. (94)

$$R_\Phi(\zeta) = \frac{\pi}{2} \frac{NA^2}{L^2} \delta \exp(-\zeta^2/(2\delta)) \, , \tag{99}$$

giving $R''_\Phi = (\pi/2)(NA^2/L^2)$, i.e. $\langle u^2 \rangle = \pi\mu A^2$, while $\langle \Phi^2 \rangle = \frac{\pi}{2}\mu A^2 \delta$.

Implicit in the derivation of Wandel and Kofoed-Hansen (1962) is the assumption that the distribution of structures (or, more correctly, structure centres) in a volume element follows a Poisson distribution, i.e. in the present case the number, k, of structure centres in an area element Δ is distributed according to $P(k) = (\Delta\mu)^k \exp(-\Delta\mu)/k!$. If two area elements are non-overlapping, then the two corresponding Poisson distributed random variables are independent. Since the equations of motion eqs. (76) - (77), certainly introduce a correlation between

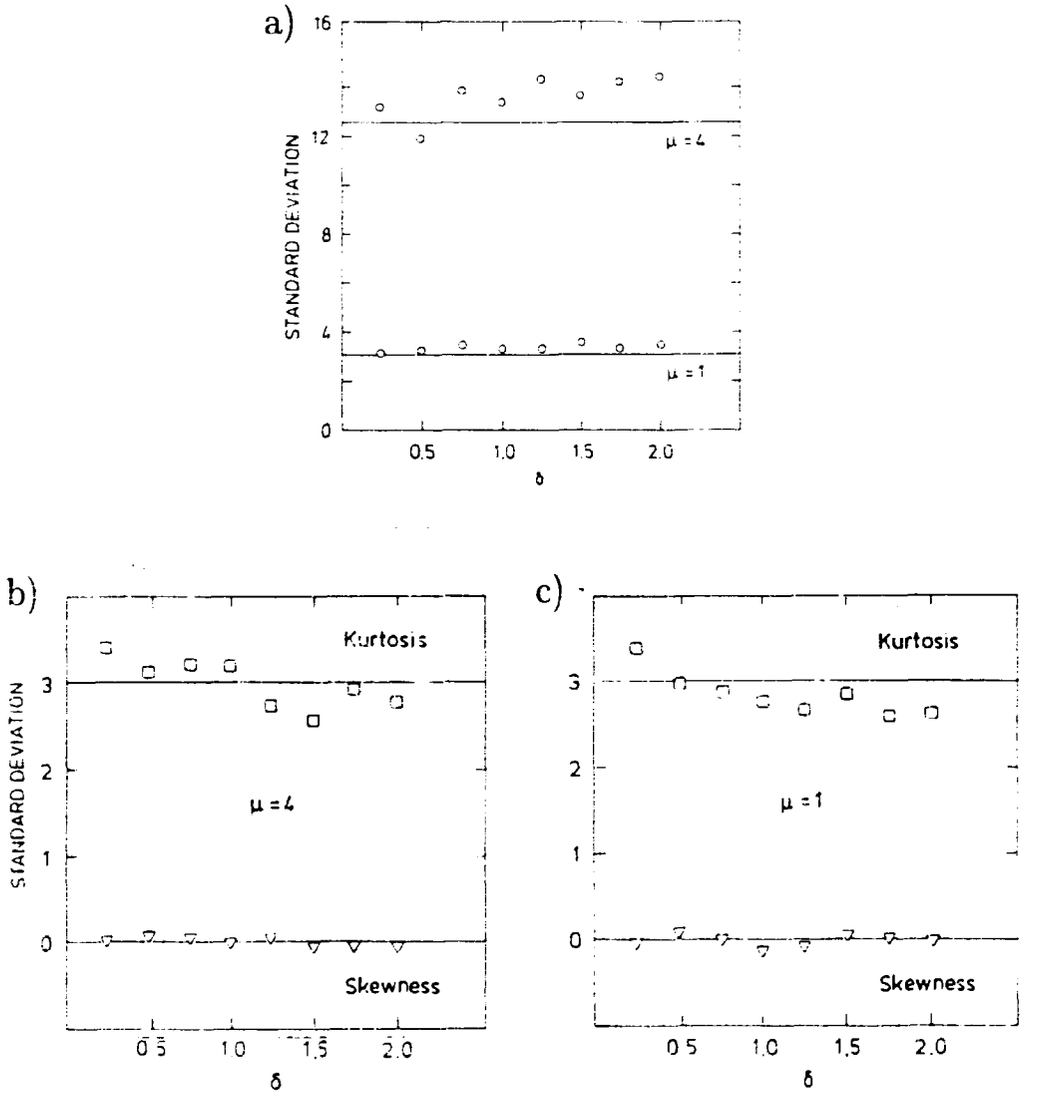

Figure 28. Variation of standard deviation, ○, skewness, Δ, and kurtosis, □ for varying width, δ, of the structures. Two different densities $\mu = 1$ and $\mu = 4$, were considered. Solid lines are the results expected for Maxwellian distributions.

all the structures, the assumption of a Poisson distribution cannot be exact. In the limit of small μ all structures are essentially isolated and they are consequently not convected at all. For low structure densities, convection will be induced primarily when two structures of opposite polarity happen to overlap, and they will propagate along an orbit characterized by their bulk properties. The orbit is a straight line if the structures are identical apart from a sign of amplitude. Two structures of same polarity will rotate around a suitably defined centre of mass. In either case structures will appear in pairs. However, again in the limit of large densities it might be expected that the correlation between individual structures is small. The assumption of a Poisson distribution mentioned before may then be appropriate. In fig.29 we show, with filled circles, the distribution of structure centres in a normalized area element 1 for $\mu = 4$. Open circles show the results for a Poisson distribution for the given parameters. We find the agreement quite acceptable.

Using eq. (93) with eq. (99) we readily obtain the expressions for the longitudinal and lateral correlation functions as

$$f(\zeta) = \exp(-\zeta^2/(2\delta)) \quad , \tag{100}$$

and

$$g(\zeta) = \frac{1}{\delta}(\delta - \zeta^2)\exp(-\zeta^2/(2\delta)) \quad . \tag{101}$$

The numerical results are shown in fig.30 with the analytical results from eqs. (100) and (101) given by a dotted line. The agreement seems fully satisfactory. In particular we confirmed that $R_{12}(\zeta) = 0$ within the statistical uncertainty, see eq. (92). In fig.30(c) the flatness factor is shown for both longitudinal and transverse velocity components. These results indicate that the joint probability density of the fluctuating velocity is close to a bivariate Gaussian, where the flatness factor is 3 for all separations. This result is expected for a random superposition of many structures (Rice, 1944). For the particularly simple model eq. (98), used here it is possible to solve eqs. (90) - (91) analytically with the result

$$R_E(\zeta,\tau) = \frac{1 + (\tau u')^2/\delta - \frac{1}{2}\zeta^2/\delta}{(1 + (\tau u')^2/\delta)^3}\exp(-\frac{1}{2}(\zeta^2/\delta)/(1 + (\tau u')^2/\delta)) \quad , \tag{102}$$

where we used $\mathcal{E}(k) = \sqrt{\delta/2\pi}\,(1 + k^2\delta)\exp(-\delta k^2/2)$ in eq. (90). In the limit $\zeta = 0$ the relation

$$R_E(0,\tau) = \frac{1}{(1 + (\tau u')^2/\delta)^2} \tag{103}$$

is obtained, while $\tau = 0$ gives $R_E(\zeta,0) = (1 - \frac{1}{2}\zeta^2/\delta)\exp(-\frac{1}{2}(\zeta^2/\delta))$ which reproduces $R_E(\zeta,0) = \frac{1}{2}[f(\zeta) + g(\zeta)]$ as it should. The limit $\tau \to 0$ is thus already analyzed by fig.30, where, as already mentioned, the expression (102) is in excellent agreement with our numerical results. For $\tau \neq 0$ we found that the largest disagreement is obtained for $R_E(0,\tau)$, i.e. the limit given by eq. (103). These results are shown in fig.31 with eq. (103) represented by a dotted curve. Close to the origin the agreement between the two curves is actually quite good, but the disagreement for large τ is obviously an indicator of a shortcoming in the model. An increase of ζ results in successively improving agreement between the numerical and analytical results. Finally, the Lagrangian correlation function is determined as

$$R_L(\tau) = \frac{1}{(1 + 2(\tau u')^2/\delta)^2} \tag{104}$$

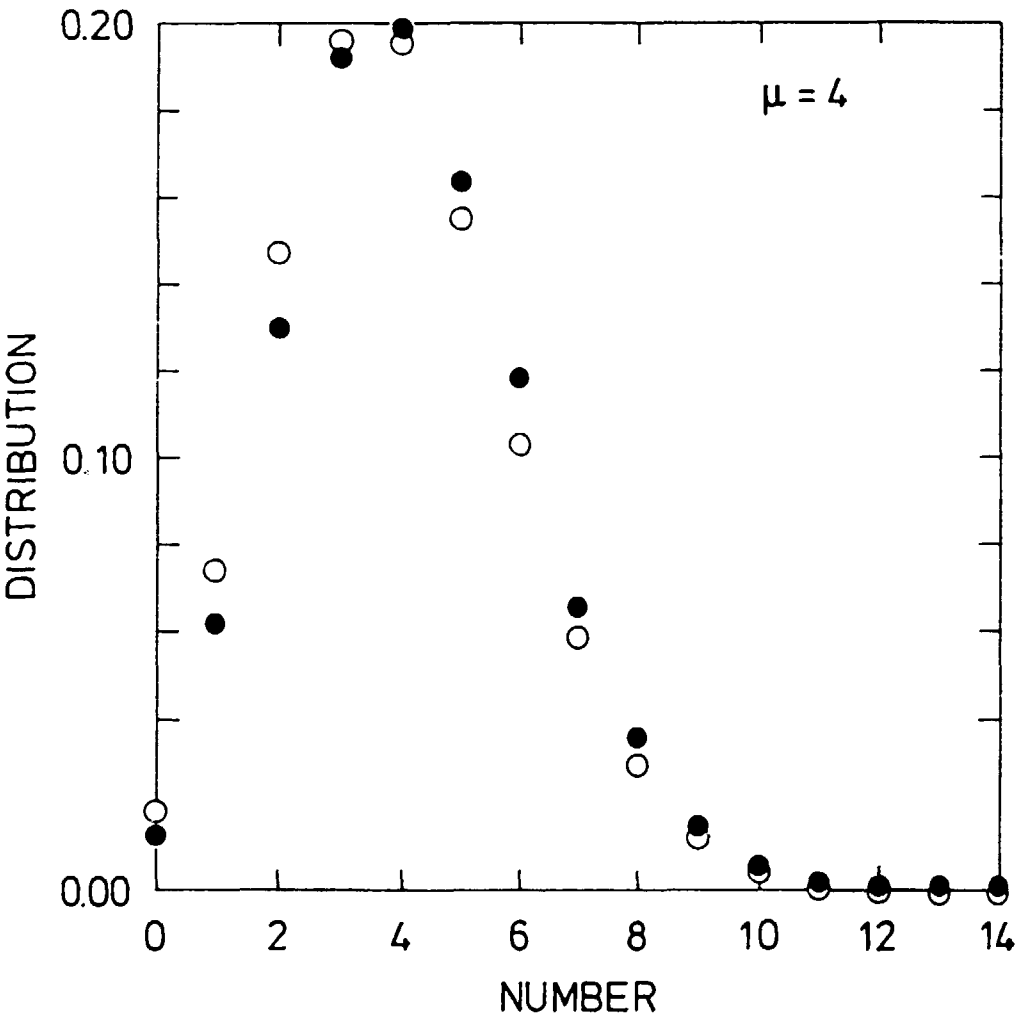

Figure 29. Distribution of the numbers of structure centres in a small area element $\Delta = 1$ for $\mu = 4$ obtained from the simulation with $\delta = \frac{1}{2}$ and $| A | = 1$. Open circles show the results from a Poisson distribution with the corresponding parameters.

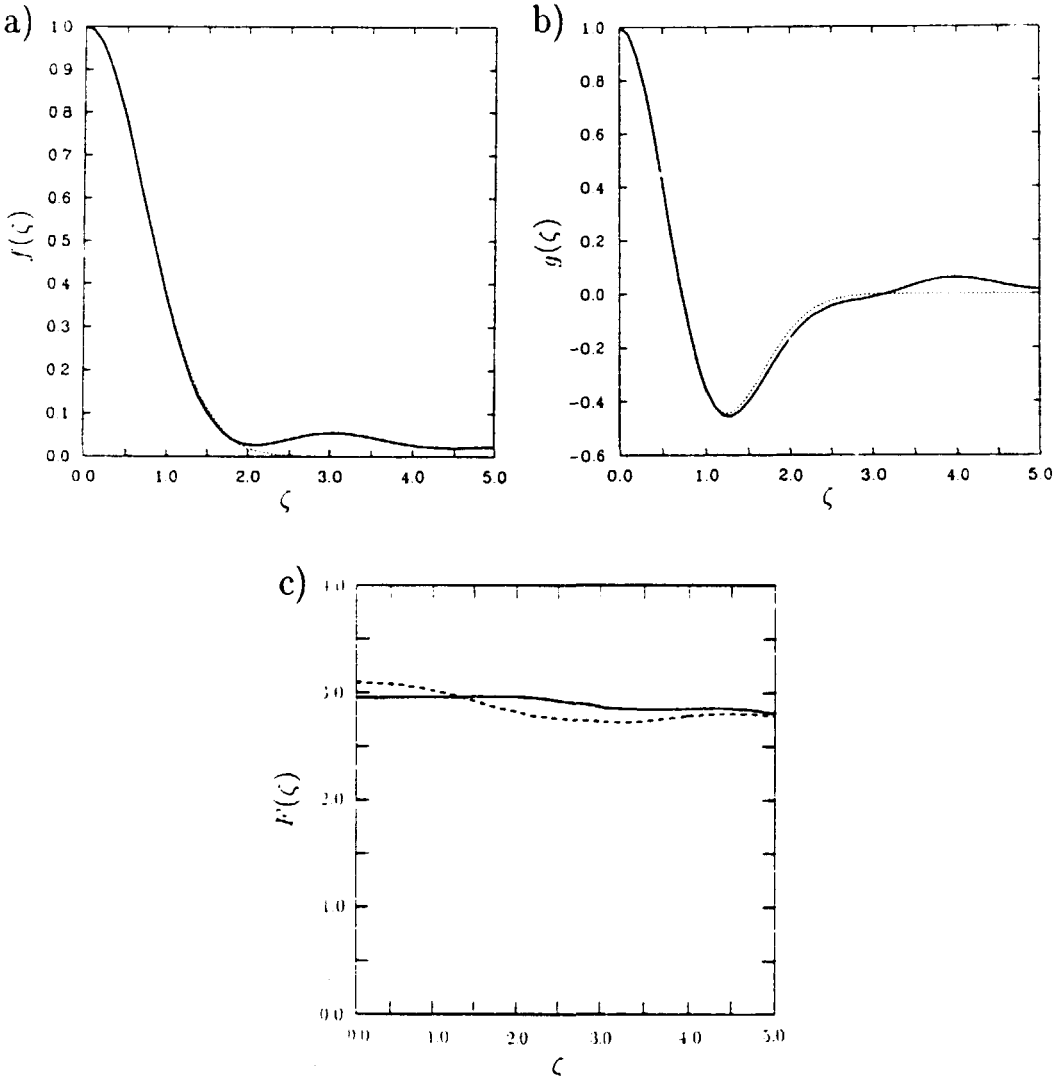

Figure 30. Results from the numerical simulation for (a) the longitudinal and (b) the lateral correlation functions, respectively. The dotted line gives the analytical results from eqs. (100) and (101). The averages are obtained from a simulation with a normalized time span of 120 with time step 10^{-2}. The parameters are $|\ A\ |= 1$, $\delta = 1/2$, and $\mu = 4$. c) Flatness factor $F(\zeta) = \langle[v_i(r_1+\zeta,r_2) - v_i(r_1,r_2)]^4\rangle / \langle[v_i(r_1+\zeta,r_2) - v_i(r_1,r_2)]^2\rangle^2$ for longitudinal (full line) and transverse (dashed line) velocity components.

Figure 32 shows numerical results where eq. (104) is included by a dotted curve for comparison. In this case the agreement is quite good. At first sight it seems paradoxical that eq. (104) gives such a good representation for the numerically simulated dynamics, while the seemingly similar expression, eq. (103), is giving only a modest approximation to the Eulerian correlations. It should, however, be noted, having in mind the simple physical discussion in section 4.2, that the analytical results implicitly assume that structures are swept rapidly past the observation point. This assumption is evidently best satisfied when the observation point is itself moving as, e.g., in Lagrangian sampling. With the substitution $r_0 = v_o t$ in eq. (102) corresponding to Eulerian sampling in a moving frame, as in eq. (90), we again obtained good agreement between numerical and analytical correlation functions, as already mentioned. Our numerical results for the Eulerian correlation function provide evidence in favor of Leslie's (1973) physical argument quoted previously, i.e. the Eulerian correlation function seems particularly sensitive to large-scale fluctuations.

Ignoring eq. (79) and prescribing straight line trajectories for the structures with a Gaussian distribution of velocities we obtain very good agreement with eq. (103). These results are shown by a dashed line in fig.31. The deviations from eq. (103) observed in fig.31 thus originate from time variations in the velocities during a structure transit time which will be particularly conspicuous for variations in slow structure velocities.

Calculations as those summarized in this section have been repeated with parameters $| A | = 1$, $\delta = 1/2$ and $\mu = 8$. The results agree with those from the simulations with $\mu = 4$, within the statistical uncertainty.

Intuitively it could be expected that an increase in $\langle u^2 \rangle$ would give rise to better agreement between numerical and analytical results for the Eulerian correlation functions. However, attempts to increase $\langle u^2 \rangle$ inevitably bring the system into the negative temperature regime characterized by a long-range ordering, and the basic assumptions in the analysis of section 4.2 are invalidated. In our simulations the transition becomes apparent by an increase in correlation lengths as compared with those obtained, e.g., from fig.30. The transition comes rather gradually and the value for the energy where the temperature changes sign is poorly defined by these numerical results.

Structures with Statistically Distributed Amplitudes

A simple generalization of the results of section 4.3 is obtained by retaining the form of eq. (98) with δ_l = constant, but letting A_l be a quantity which varies randomly with l. When all A_l have the same distribution, the results of section 4.3 are readily generalized by the extension of Campbell's theorem given by Rice (1944) and for instance eq. (99) is trivially generalized by use of eq. (94). The important point here is that the Hamiltonian eq. (80), applies for the present problem also. The numerical simulations were extended to cover also the case where A_l was varying. In order to ensure that $\int \phi d\mathbf{r} = 0$ we included structures pairwise with both polarities of A_l for varying l. We considered a case with equal number of amplitudes 1.2 and 0.8 and $\delta = 0.5$. Another simulation used a random number generator with amplitudes distributed in the range [0.8 ; 1.2] so that the average remained 1.0 also with $\delta = 0.5$. Finally, we considered the case with amplitudes A_i = 0.5, 1.0, 1.5 and 2.0 all with same density $\mu_i = 1$ while δ =

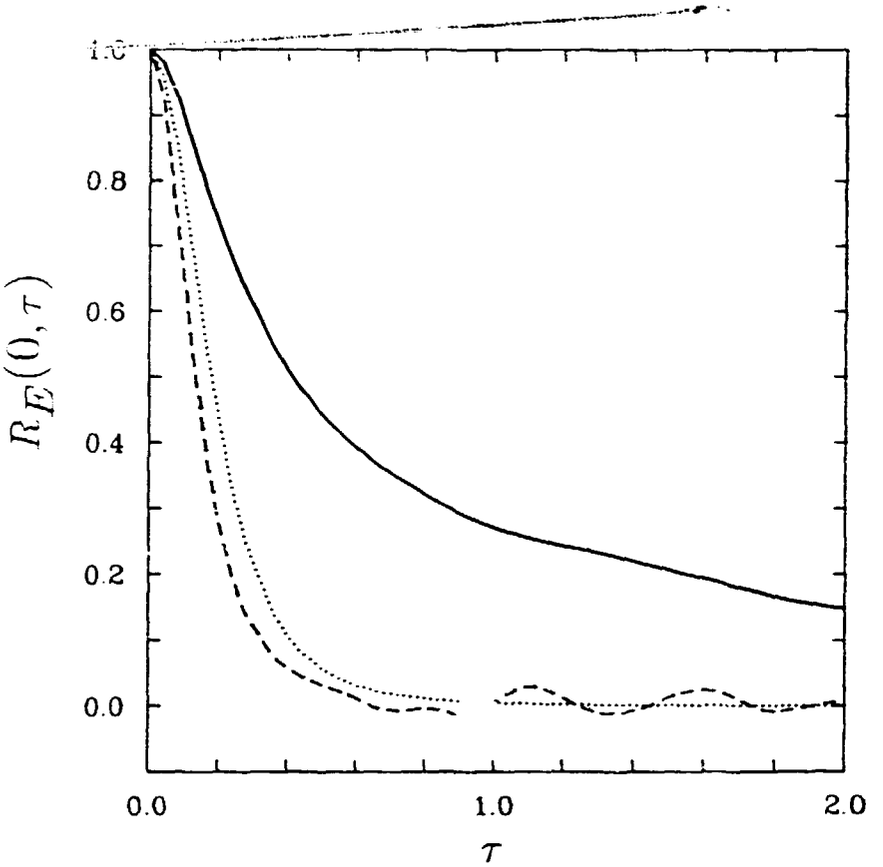

Figure 31. Numerical results for $R_E(0,\tau)$ with the analytical expression represented by a dotted line. The dashed line shows numerical results where the individual structures are moving along straight line orbits with constant velocities which have been chosen randomly from a Gaussian distribution. Parameters are as in Fig.30.

1. Comparing the numerically obtained correlation functions with the analytical results we found the same overall agreement as the one found in section 3.1, maybe with a slight improvement, which was, however, within the statistical uncertainty. In particular we did not find any noticeable improvement in the agreement with the analytical expression for the Eulerian correlation function.

4.4 Conclusions and Discussions

The relation between Eulerian and Lagrangian correlation functions has been studied in a two dimensional autonomous flow model, which can be considered as a generalization of Onsager's line vortex model. The results from a numerical simulation, where the properties of the model were implemented, were compared with analytical expressions for the correlation functions obtained by applying the ideas of Wandel and Kofoed-Hansen (1962) in a two-dimensional representation. In agreement with the simulation model this analysis assumes that a randomly varying flow is represented by a superposition of coherent structures in the form of vortices where each one propagates without change in shape along a trajectory which is determined by the combined convective effect of all other structures. In the present analysis we used a particularly simple shape for the individual structures eq. (98) characterized by only two parameters, i.e. an amplitude and a width. By use of this simple form all analytical results can be expressed in a closed form where the distribution of the parameters enters. The Eulerian correlation function

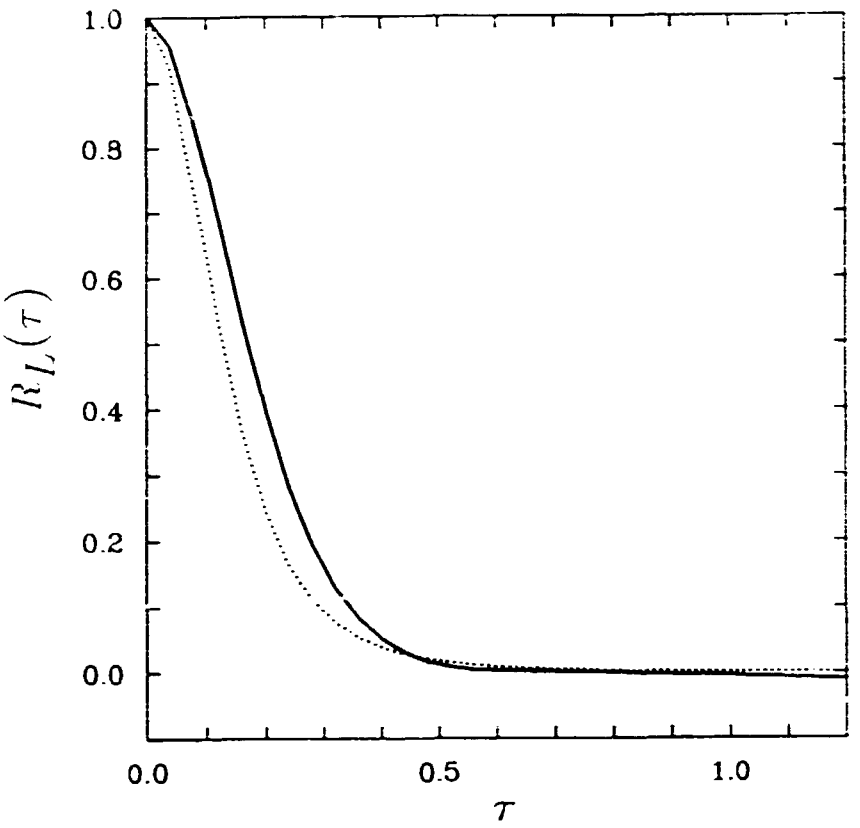

Figure 32. Numerical results for the Lagrangian velocity correlation function $R_L(\tau)$ with the analytical expression represented by a dotted line. Parameters are as in Fig. 30.

$R_E(\zeta, \tau)$ as well as its Lagrangian counterpart $R_L(\tau)$ are expressed in terms of the same wavenumber spectrum integrated together with weight functions containing the amplitudes, widths, and densities of the structures as parameters.

The conclusions from a comparison between the numerical and analytical results can be summarized as follows: for the limiting case $R_E(\zeta, \tau = 0)$ we found very good agreement in all investigated cases. As τ is increased, the agreement becomes progressively worse where the limit $R_E(\zeta = 0, \tau)$ gives the most pronounced disagreement between theory and simulations, where in particular the Eulerian correlation time from the simulations exceeded the theoretical value, see fig.31. We observed, however, that in the limit where the product $\delta\mu$ exceeded a value around 1 in the simulations, the micro-time scale defined by $[d_\tau^2 R_E(0,\tau)]_{\tau=0}^{-1/2}$ is in quite good agreement with its analytical expression. In the same limit good agreement was found for the Lagrangian correlation function $R_L(\tau)$ for all values of τ, see e.g. fig.32. The latter results were demonstrated as being independent of the conservation of the Hamiltonian, eq. (80), by the model (these results are not shown here). The limit $\delta\mu \geq 1$ implies that in any given point more than four structures contribute, on average, to the local bulk velocity obtained by the superposition, eqs. (76) or (78). For computational reasons we considered only cases where $\mu \leq 8$. For a typical value of $\delta = \frac{1}{2}$ we found, however, that $\mu > 2$ was sufficient to ensure that the probability densities of the velocity components were close to Gaussians.

The diffusion of passive particles can readily be investigated in the simulations of the model. The mean square displacement of a particle with respect to its origin

of release is given by, e.g., Lumley and Panofsky (1964) by expression (27). We have not carried out any particular study of the mean square displacement since the results can easily be derived from $R_L(\tau)$ which we have analyzed in detail.

The basic results of our study were a demonstration that within the present model the Lagrangian correlation function, to quite good approximation, could be obtained from expression (85) which involved as input parameters only the wavenumber powerspectrum $\mathcal{E}(k)$ and the mean-square fluctuation level $\langle u^2 \rangle$. The weight function $W(\zeta)$ in eq. (85) is an a priori given quantity. With both $\mathcal{E}(k)$ and $\langle u^2 \rangle$ being measurable quantities, the relation (85) and its three-dimensional analogue can be postulated as universal approximations valid irrespective of the model from which they were derived. Actually, Wandel and Kofoed-Hansen (1962) and Kofoed-Hansen and Wandel (1967) presented arguments for rather a general validity of the approximation and at least applied to the Hay-Pasquill (1960) hypothesis the results proved quite convincing.

Finally, we should like to point out that simulations like the ones used in the present work can be useful for testing methods for recovery of large coherent structures in turbulent flows (see e.g. Fazle Hussain, 1986). The flow in our simulation is composed entirely of coherent structures, and we find it worth noting that the lowest order approximation advocated by Adrian (1979) and Adrian and Moin (1988) will produce signatures for double-vortex structures. As pointed out by Pécseli and Mikkelsen (1986), this result could be fundamentally misleading since the flow is, by construction in our case, composed of monopole-type structures.

References

Adrian, R.J. 1979. Phys. Fluids **22**, 2065.

Adrian, R.J. and Moin, P. 1988. J. Fluid Mech. **190**, 531.

ASDEX Team 1989. Nucl. Fusion **29**, 1959.

Batchelor, G.K. 1953. *The Theory of Homogeneous Turbulence*, Cambridge University Press, Cambridge.

Blackwelder, R.F. and Kapland, R.E. 1976. J. Fluid Mech. **76**, 89.

Chandrasekhar S. 1961. *Hydrodynamic Hydromagnetic Stability*, Clarendon, Oxford.

Chen, F.F., Etievant, C. and Mosher, D. 1968. Phys. Fluid **11**, 811.

Chen, F.F. 1974. *Introduction to Plasma Physics*, Plenum Press.

Chorin, A.J. 1973. J.Fluid Mech. **57**, 785.

Corrsin, S. 1960 in: *Atmospheric Diffusion and Air Pollution*, ed. by Frenkiel, F.N. and Sheppard, P.A. [Advances in Geophysics, Vol 6 (Academic, New York)] p.162.

Coutsias, E.A. and Lynov, J.P 1991. Physica D **51**, 482.

Coutsias, E.A., Hansen, F.R., Huld, T., Knorr, G. and Lynov, J.P. 1989. Physica Scripta **40**, 270.

Currie, I.G. 1974. *Fundamental Mechanics of Fluids*, McGraw-Hill.

Ewald, P.P. 1921. Ann. Phys. (Leipzig) **64**, 253.

Fox, D.D. and Orzag, S.A. 1973. J. Comp. Phys., **11**, 612.

Fjørtoft, R. 1953. Tellus **5**, 225.

Gazdag, J. 1976. J. Comput. Phys. **20**, 196.

Gottlieb, D. and Orszag, S.A. 1977. *Numerical Analysis of Spectral Methods: Theory and Applications*, SIAM, CBMS-NSF Reg. Conf. Ser. in appl. Math. **26** 170.

Hallock, G.A., Wotton, A.J. and Hickok, R.L. 1987. Phys. Rev. Lett. **59**, 1301.

Hay, J.S. and Pasquill, F. 1960. Advances in Geophysics **6**, 345.

Hasegawa, A. 1985. *Self-Organization Processes in Continuous Media*, Adv. Phys. **34**. 1.

Hinze, J.O. 1975. *Turbulence*, McGraw Hill, New York, 2. ed..

Horton, W., Tajima, T. and Kamimura, T. 1987. Phys. Fluids **30**, 3485.

Horihata, S., Irie, H. and Sato, M. 1990. J. Phys. Soc. Jpn. **59**, 1242.

Huld, T., Iizuka, S., Pécseli, H.L., and Rasmussen, J.Juul 1988. Plasma Phys. Contr. Fusion **30**, 1297.

Huld, T. 1990. *Experimental and Numerical Investigations of Plasma Turbulence*, RisøR-2858.

Huld, T. 1990b. *User's Manual for the AIDA Data Acquisition and Display System*, RisøNational Laboratory. Internal Report.

Huld, T., Nielsen, A.H., Pécseli, H.L. and Rasmussen, J. Juul 1990. Phys. Rev Lett. **64**, 3023.

Huld, T., Nielsen, A.H., Pécseli, H.L. and Rasmussen, J.Juul 1991. Phys. Fluids B **3**, 1609.

Hussain, A.K.M.F. 1986. J. Fluid Mech. **173**, 303.

Ingensoll, A.P. 1988. Nature **331**, 654.

Jassby, D.L. 1972. Phys. Fluids **15**, 1590.

Johnsen, H., Pécseli, H.L. and Trulsen, J 1989. Phys. Scr. **40**, 280.

Joyce, G. and Montgomery, D. 1973. J.Plasma Phys **10**, 107.

Kent, G.I., Jen, N.C. and Chen, F.F. 1969. Phys. Fluids **12**, 2140.

Knorr, G., Lynov, J.P., Pécseli, H.L. 1990. Z.Naturforsch **45 a**, 1059.

Knorr, G., Hansen, F.R., Lynov, J.P., Pécseli, H.L. and Rasmussen, J. Juul 1988. Physica Scripta **38**, 829.

Knorr, G. and Pécseli, H.L. 1989. J. Plasma Phys. **41**, 157.

Kofoed-Hansen, O. and Wandel, C.F 1967. Risø Rep. No. 50.

Kraichnan, R.H. 1964. Phys. Fluids **7**, 142.

Lesieur M., 1987. *Turbulence in Fluids*, Martinues Nijhoff, Dordrecht.

Leslie, D.C 1973. *Developments in the Theory of Turbulence*, Clarendon Press, Oxford.

Lumley, J.L. and Panofsky, H.A 1964. *The Structure of Atmospheric Turbulence*, Interscience, New York.

Lynov, J.P., Nielsen, A.H., Pécseli H.L. and Rasmussen, J. Juul, J. Fluid Mech. 1991. **224**, 485.

Marcus, P.S. 1990. J. Fluid Mech. **215**, 393.

Montgomery, D. and Joyce, G. 1974. Phys. Fluids **17**, 1139.

Motley, R.W. 1975. *Q-machines*, Academic Press, New York.

Onsager, L. 1949. Nouvo Cimentc Suppl. **6**, 279.

Panofsky, H.A. and Dutton, J.A. 1984. *Atmospheric Turbulence*, John Wiley, New York.

Pécseli, H.L. and Mikkelsen, T. 1985. J. Plasma Phys. **34**, 77.

Pécseli, H.L. and Mikkelsen, T. 1986. Plasma Phys. Contr, Fusion **28**, 1025.

Pécseli, H.L. and Trulsen, J. 1989. Phys. Fluids B **1**, 1616.

Pécseli, H.L., Primdahl, F and Bahnsen, A. 1989. J. Geophys. Res. **94**, 5337.

Peskin, R.L. 1974. In: *Turbulent Diffusion in Enviromental pollution* ed. by Frenkiel, F.N. and Munn, R.E. [Advances in Geophysics, Vol **18A** (Academic, New York)] p.141.

Press, W.H., Flannery, B.P., Teukolsky, S.A., Vettering, W.T. 1986. *Numerical Recipes*, Cambridge University Press, Cambridge

Reeks, M.W. 1977. J.Fluid Mech. **83**, 529

Rice, S.O. 1944. Bell System Techn. Journal **23**, 282 and 1945, ibid. **24**, 46. Reprinted In: *Selected Papers on Noise and Stochastic Processes* (ed. N.Wax) 1954, Dover.

Rosenbluth, M.N. and Simon, A. 1965. Phys. Fluids **8**, 1300.

Salu, Y. and Montgomery, D. 1977. Phys. Fluids **20**, 1.

Seyler, C.E., Salu, Y., Montgomery, D., and Knorr, G. 1975. Phys. Fluids **18**, 803.

Sulem, C. and Sulem, P.L. 1983. J. Méchanique Theor. Appl. Numéro Special, 217.

Sulem, C., Sulem, P.L. and Frisch, H. 1983. J. Comp. Phys. **50**, 138.

Tennekes, H. 1975. J. Fluid Mech **67**, 561.

Wandel, C.F. and Kofoed-Hansen, O. 1962. J. Geophys. Res. **67**, 3089.

Weinstock, J. 1976. Phys. Fluids **19**, 1702.

Wootton, A.J., Austin, M.E., Bengtson, R.D., Boedo, J.A., Bravenec, R.V., Brower, D.L., Chen, J.Y., Cima, G., Diamond, P.H., Durst, R.D., Edmonds, P.H., Fan, S.P., Foster, M.S., Forster, J.C., Gandy, R., Gentle, K.W., Hickok, R.L., Hey, Y.X., Kim, S.K., Kim, Y.J., Lin, H., Luhmann, N.C., McCool, S.C., Miner, W.H., Ouroua, A., Patterson, D.M., Peebles, W.A., Philips, P.E., Richards, B., Ritz, Ch.P., Rhodes, T.L., Ross, D.W., Rowan, W.L., Schoch, P.M., Sing, D, Synalowski, E.J., Terry, P.W., Wenzel, K.W, Wiley, J.C., Yang, X.Z., Yu, X.Z., Zhang, Z., and Zheng, S.B. 1988. Plasma Phys. Controlles Fusion **30**, 1479.

Yeung, P.K. and Pope, S.B. 1989. J. Fluid Mech. **207**, 531.

Bibliographic Data Sheet **Risø-R-659(EN)**

Title and author(s)

Electrostatic Turbulence in Strongly Magnetized Plasmas

Anders H. Nielsen

ISBN	ISSN
87-550-1865-3	0106-2840

Dept. or group	Date
Department of Optics and Fluid Dynamics	January 1993

Groups own reg. number(s)	Project/contract No.

Pages	Tables	Illustrations	References
81		33	67

Abstract (Max. 2000 char.)

Turbulence in plasmas has been investigated experimentally and numerically.

- On the experimental side the turbulent nature of the Kelvin-Helmholtz instability has been studied in a single-ended Q-machine. The development of coherent structures in the background of the turbulent flow has been demonstrated and the capability of structures of transporting plasma across the magnetic field-lines is explained in detail.

The numerical investigations are divided into two parts:

- Numerical simulations of the dynamics from the Q-machine experiments using spectral methods to solve the two-dimensional Navier-Stokes equations in a cylindrical geometry.
- A numerical study of the Eulerian-Lagrangian transformation in a two-dimensional flow. Here the flow is made up by a large number of structures, where each individual structure is convected by the superposed flow field of all the others.

Descriptors INIS/EDB

COLLISIONLESS PLASMA; COMPUTERIZED SIMULATION; DIFFUSION; DYNAMICS; ELECTROSTATICS; FLOW MODELS; HELMHOLTZ INSTABILITY; NAVIER-STOKES EQUATIONS; PLASMA SIMULATION; TURBULENCE; VORTICES

Available on request from:
Risø Library, Risø National Laboratory (Risø Bibliotek, Forskningscenter Risø)
P.O. Box 49, DK-4000 Roskilde, Denmark
Phone (+45) 42 37 12 12, ext. 2268/2269 · Telex 43 116 · Telefax (+45) 46 75 56 27

Available on request from:
Risø Library
Risø National Laboratory,
P.O. Box 49, DK-4000 Roskilde, Denmark
Phone +45 42 37 12 12, ext. 2268/2269
Telex 43116, Telefax +45 46 75 56 27

ISBN 87-550-1865-3
ISSN 0106-2840